Modeling Flow-induced Collapse in Human Airways

Modeling flow-induced collapse in human airways
O. Massiot

Cover Image: O. Massiot

Thesis University of Twente, Enschede - With ref. - With summary in Dutch.
ISBN 90-365-2103-3

MODELING FLOW-INDUCED COLLAPSE IN HUMAN AIRWAYS

PROEFSCHRIFT

ter verkrijging van
de graad van doctor aan de Universiteit Twente,
op gezag van de rector magnificus,
prof.dr. F.A. van Vught,
volgens besluit van het College voor Promoties
in het openbaar te verdedigen
op vrijdag 17 december 2004 om 13.15

door

Olivier Massiot

geboren op 10 oktober 1975
te Rennes, Frankrijk

Dit proefschrift is goedgekeurd door de promotor:
prof.dr.ir. H.W.M. Hoeijmakers
en de assistant promotor:
dr.ir. F.H.C. de Jongh

TABLE OF CONTENTS

INTRODUCTION

1 CHAPTER

An introduction to the subject of airflow in a human lung is presented.
The lung-function test, a clinical test to determine the health state of the lung of a patient, is described in order to show the importance of the possible applications of the present research. Subsequently, the existing lung models that illustrate the complexity of the geometry of a lung are presented. Finally, the state-of-the-art of research on collapsible tubes, that mainly has been conducted for the last three decades, is reviewed.

1.1 Introduction

Lung diseases occur more and more frequently. They represent a major clinical, as well as economical issue at present and in the foreseeable future. Examples of major lung diseases are for instance COPD (Chronic Obstruction Pulmonary Disease) and asthma. Lung diseases may amongst others be caused by air pollution (lung alteration) and premature births (incomplete grown lungs). Chronic inflammation on a micro-scale may result in structural changes on macro-scale. This may lead to lung tubes with increased or decreased wall elasticity. During both inspiration and expiration, the tubes with decreased wall elasticity will collapse earlier.
A collapse appears when the transmural pressure defined as the pressure inside the tube minus the pressure outside the tube is negative. In other words, the internal pressure is lower than the external (pleural) pressure, resulting in compression of the tube. Tube collapse may also happen in healthy lungs during a forced expiration. Tube collapse results in a typical time history of the flow rate at the mouth. The shape of the resulting flow-volume curve, measured at the mouth, is used as clinical diagnostic tool for the health condition of the lungs.
More research is needed to correlate the characteristic shapes of the flow-volume curves to the distribution of the mechanical properties of the lung tube system. This can help to improve the treatment of patients. An example is the local administration of aerosols for targeting diseased lung areas.

1.2 The lung-function test

The world-wide standard used as a lung-function test is the so-called forced expiration. The patient is asked to inhale fully, then blow as fast and deep as possible, followed by a full

inhalation. The flow rate is measured at the mouth of the patient. The result is graphed in a flow-volume curve. An example for a healthy adult male (30 years, $1.83\ m$) is displayed in figure 1.1. In this curve, the expiratory flow rate is displayed on the positive vertical axis, the exhaled volume on the horizontal axis; the origin is at the beginning of the test (i.e. after the initial inhalation, i.e. at maximal lung-volume and no flow). The test proceeds clockwise

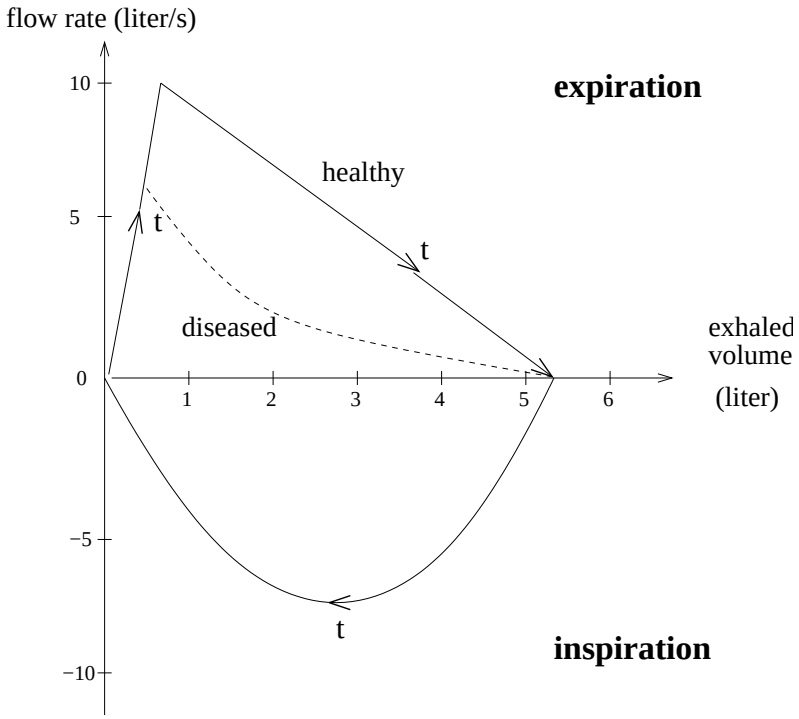

FIGURE 1.1: *Flow-volume curve: adult male (*30 *years,* $1.83\ m$*).*

along the curve. The part below the horizontal axis, the inhalation, corresponds to a more or less sinusoidal flow pattern. However, the expiratory part has a typical form, characterized by a fast rise to the expiratory peak flow rate followed by an almost linear flow-rate volume relation. This linear part is effort independent and the consequence of airway collapse. The location of the airway collapse in the lungs shifts during this forced expiration, from the larger airways (top part of the line) to the more peripheral airways (lower part of the line).
A lung disease might influence the elasticity of the lung tubes. For instance for patients with asthma the expiratory part of the curve will become more concave as indicated by the dashed line in figure 1.1. The inspiratory part remains unchanged.
The ultimate goal of the present research is to consider a model of the lung that can reproduce a flow-rate volume curve. Calculating the flow through a network of branching elastic tubes should give insight in how and at which location tube collapse occurs during a forced expiration. This analysis should account for the larger airways being at normal lung volume more rigid than the smaller airways. With an altered distribution of the elasticity of the lung tubes

it should be possible to reproduce the typical shape of the flow-rate volume curves observed in patients with diseases like asthma and chronic obstructive pulmonary disease (COPD). If known at which lung tube generation the changes of the elasticity of the lung tubes dominates the airway collapse, one could try to target that area with an aerosolized medication.

1.3 Lung model

1.3.1 Terminology

The terminology used to describe the basic components of a lung are presented in figure 1.2. A lung is considered as a tree, and all branches are called "tubes". The "tree" is built in a repetitive process, in which each tube splits into two tubes. Each level of this process is called a "generation". The n^{th} generation consists of 2^n tubes.
The air inspired from the mouth enters the lungs through the trachea. The trachea (generation 0) is the first generation of tubes consisting of a single, stiff tube. The air flows then through the bronchi, bronchioles and finally terminal bronchioles, from generation 1 to generation 16. This part of the lung is called the conductive zone, since no gas exchange occurs. The next part is referred as to the transitional and respiratory zone. At generation 16, small "spheres", called alveoli, start to appear on the lung tubes, in which gas exchange takes place. From generation 16 to the last one (23 to 27, depending on the specific model utilized), the number of alveoli increases strongly. The tubes of the last generation end with alveoli.

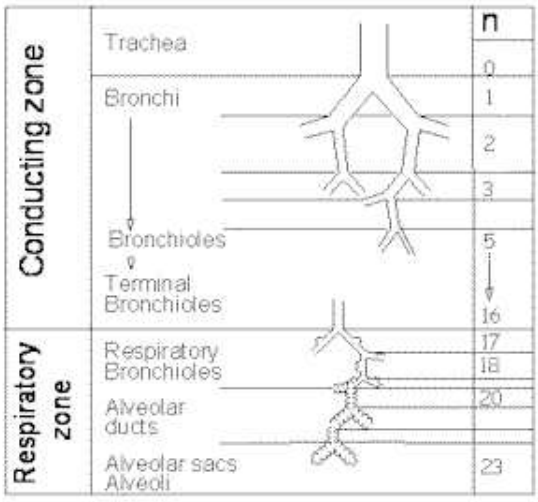

FIGURE 1.2: *Medical terminology used to describe the bronchial tree. The tubes are drawn in a plane for simplicity. n is the generation number. (from F.H.C. de Jongh (1995) after Weibel's lung model ([53]))*

1.3.2 Lung model of Weibel and Hansen-Ampaya

Historically the first model was introduced by Roher and Rauwerda (see [46] and [45]). They modelled the lung as a single cylinder with a cross-sectional area diverging linearly with the lung depth. However, in such a geometrical model, the exponential growth of the cross-sectional area of the higher generations is underestimated. Later, better models have been introduced with a more realistic relation between cross-sectional area and lung depth.
The Weibel lungmodel, today almost the *de-facto* standard lung model, was developed in 1963 (see [53]). It incorporates 24 generations of symmetrically dividing tubes. The tubes of each generation end in two tubes in the next generation. The first generation ($n = 0$) consists of a single tube (the trachea). The second generation ($n = 1$) consists of two tubes (left and right main branches) and so on. The length L in cm and diameter D in cm of the tubes are given by empirical relations. For a human adult:

$$\begin{array}{ll} 0 \leq n \leq 3 & : L = 12e^{-0.92n}, \quad A = 2.54e^{-0.083n} \\ 4 \leq n \leq 23 & : L = 2.5e^{-0.17n}, \quad A = 1.32e^{(0.107+0.0125n)n} \end{array} \tag{1.1}$$

with $A = \pi D^2/4$ the cross-sectional area in cm^2. Since the model is symmetrical, the cross-sectional area of all the tubes can be added to yield the total cross-sectional area. Figure 1.3 displays this cross-sectional area against the distance from the trachea. It shows the particular structure of the lung. The cross-sectional area is relatively small in the first 16 generations (26 cm from the beginning of trachea). The alveoli, in which gas exchange with the blood occurs, start to appear at generation 16. The tube cross-sectional area increases very rapidly, from 0.02 m^2 at generation 3 to 1.15 m^2 at the last generation. Furthermore, all alveoli (around 400*10^6) combined have a surface area of 70 - 140 m^2.

The characteristic distribution of the cross-sectional area as function of the lung depth has consequences for the flow through the tube system. The law of mass conservation (for a steady quasi-one dimensional flow $\rho UA =$ constant) with the density ρ assumed constant, implies that the cross-sectional averaged velocity U is inversely proportional to the cross-sectional area A. For normal respiration, assuming a normal tidal breath of 500 cm^3 in 5 seconds, (2.5 seconds inspiration and 2.5 seconds expiration), the average velocity in the trachea (with a diameter D of 1.8 cm) is 200 (cm^3/s) / 2.54 (cm^2) = 78.6 cm/s, corresponding to a Reynolds number ($Re_D = UD/\nu$) of 1.4*10^3. For a fully developed flow pipe flow turbulence does not appear below $Re_D = 2300$ ([13]). Apparently during normal respiration, and considering rigid tubes, the flow is laminar in the entire lung since the increasing cross-sectional area at the higher generations implies a still lower velocity and, combined with a smaller individual tube diameter, therewith an even smaller Reynolds number.
For forced expiration, however, the peak expiratory flow rate (measured at the mouth) is around 10 $liters/s = 10000$ cm^3/s. With the cross-sectional area of the trachea of 2.54 cm^2, the velocity in the trachea becomes 40 m/s, corresponding to a Reynolds number of about 5.4*10^4. This shows that the flow is definitely turbulent in the trachea in the case of forced expiration.

The "1963 lungmodel" from Weibel ([53]) has limitations. For instance, the dimensions of the tubes were measured in a lung at 75% of its maximum inflation, far from the conditions at rest which are achieved after a normal expiration. Another limitation is the symmetrical

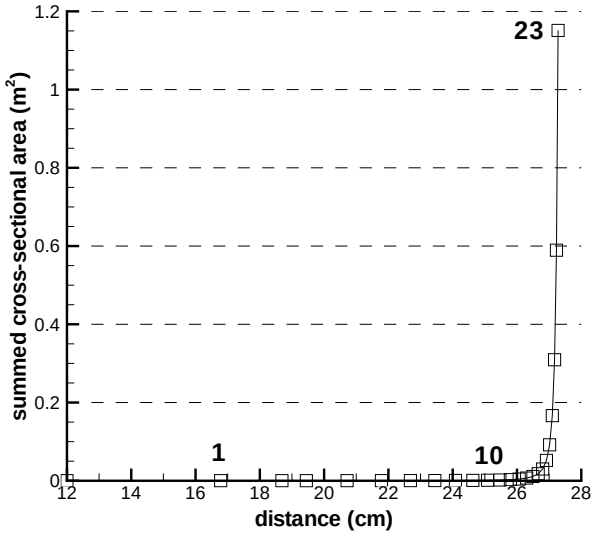

FIGURE 1.3: *Summed cross-sectional area of Weibel model for an adult lung versus distance starting from the end of the trachea. The generation is indicated by the squares.*

division of the tube system, while also a real lung does not end that abruptly at generation 23. Hansen and Ampaya ([16]) refined the last generations of the Weibel model. They concluded that a lung possesses 27 generations of tubes. The doubling of the number of tubes in each generation was replaced by a system in which the number of tubes increased up to generation 24 after which the number of tubes was decreased. Also, and after a detailed study of the alveoli, they stated that a human lung has more alveoli than assumed by Weibel ([53]).

1.3.3 Deformation of a collapsible tube

Experimental studies

The problem of the flow in collapsible tubes has been studied experimentally by many authors. The typical experimental set-up shown in figure 1.4, referred to as the "Starling Resistor", forms the basis for most analyses. The experiment exhibits many of the same characteristics as physiological collapsible tubes (lung airways, arteries or veins).
Inside a pressure chamber (pressure p_{ext}) a thin elastic tube (typically rubber) of length L, undeformed internal radius R and of wall thickness h is mounted between two rigid tubes. A viscous fluid (typically air or water) flows through the tube at a steady flow rate.
The flow can be controlled either by the flow rate Q or by the pressure drop $p_{entry} - p_{exit}$ applied between the two ends of the rigid tube. If p_{ext} exceeds the fluid pressure (inside the tube) sufficiently, the tube buckles non-axi-symmetrically, as sketched in figure 1.4. Flow-structure interaction then leads to a strongly non-linear relation between pressure-drop and flow-rate, depending on which pressure differences are held fixed as the flow increases (see [6]):

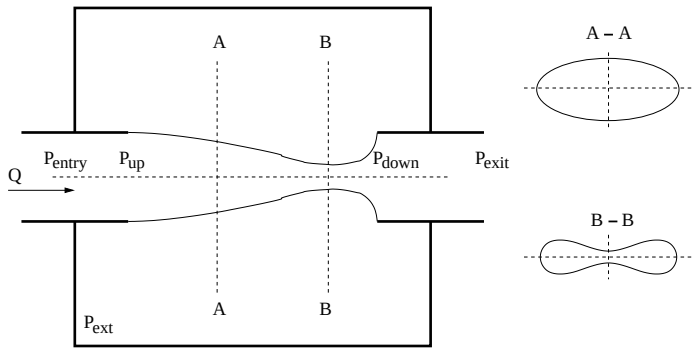

FIGURE 1.4: *Left: sketch of a typical experiment al apparatus, referred to as the "Starling Resistor". A thin elastic tube is mounted between two rigid tubes, and a fluid flows through the tube at a steady flow rate. Right: tube cross-sections at A-A and B-B.*

- flow limitation, i.e. increasing $p_{up} - p_{down}$, while keeping $p_{up} - p_{ext}$ fixed, which limits the maximum possible flow rate Q

- pressure-drop limitation, i.e. increasing Q with $p_{down} - p_{ext}$ fixed, which limits the maximum possible $p_{up} - p_{down}$.

At sufficiently large Reynolds numbers, the system also readily produces self-excited oscillations ([34], [3]).

Theoretical analysis: a general introduction

Already for three decades, a theoretical analysis that can explain the experimentally observed features is searched for. Yet, despite all the efforts, full details of the interaction of the flow and deformation of the tube are not completely understood.
Ideally one would like to find a solution of the unsteady, three-dimensional Navier-Stokes equations, coupled to the equations for the unsteady, three-dimensional, large deformation of the highly compliant tubes, this for different breathing patterns.

Lumped-parameter models
The first theoretical models of flow in collapsible tubes were lumped-parameter models ([6], [26]). In these models the system's behaviour is characterized by a small number of scalar variables, such as the cross-sectional area, the transmural pressure (local pressure – external pressure) and the fluid velocity at the narrowest point of the tube. These models do predict experimentally observed features, such as oscillatory behaviour. However, they fail to describe many aspects of the mechanical behaviour of the tube's deformation. Therefore a more sophisticated approach is needed.

One-dimensional models
In one-dimensional models the pressure and the axial velocity, both averaged across the tube cross-section, together with the cross-sectional area, are regarded as functions of the longitudinal coordinate x and the time t. The one-dimensional models give a good insight in the

basics of the flow and are easy to deal with numerically. Many different models have been developed so far, but they all have a number of disadvantages in common. Firstly, the solid mechanics of the tube is always a crude approximation of the solid mechanics of the real airway, which can be considered to be a non-axi-symmetric, cylindrical shell under prestretch. Secondly, the fluid mechanics involved in the model is crude, primarily because of the way the flow separation and the associated process of energy loss is modelled.

Two-dimensional models
Several two-dimensional models exist and produce satisfactory results in predicting the deformation of the wall, flow recirculation, flow limitation, etc ..., but they mainly have the same disadvantages as the one-dimensional models described above.
The problem solved with these $2D$ models is the flow in a straight channel, in which one part of the wall is replaced by an elastic membrane ([41], [32], [33], [44]).

Three-dimensional models
Nowadays the use of three-dimensional models is possible. These are investigated for instance by Heil ([18]). The large-displacement, geometrically non-linear Kirchhoff-Love shell theory, is fully coupled with either lubrication theory (assuming a small slope of the tube wall), Stokes flow (zero-Reynolds number flow) or the Navier-Stokes equations. The numerical results for the three-dimensional tube deformation closely resemble the experimental results. So far only steady flow calculations have been performed.

1.4 Flow in collapsible tube: review

In this section the different incompressible flow models as well as the different structural models utilized for studying the flow in collapsible tubes are described in some more detail.

1.4.1 Incompressible flow models (1D, 2D, 3D)

1D flow

Employing the Navier-Stokes equation (including body forces and a lumped representation of small viscous effects), the axial component of the momentum equation, for the case of a vertical tube with flow on downward direction, is given by:

$$\frac{\partial u}{\partial t} + u\frac{\partial u}{\partial x} = g - \frac{1}{\rho}\frac{\partial p}{\partial x} - Ru \tag{1.2}$$

where $u = u(x,t)$ is the cross-sectionally averaged axial velocity of the fluid, $p = p(x,t)$ is the fluid pressure, ρ the fluid density and $R > 0$ is a friction factor which value depends on the local cross-sectional area $A(x,t)$. g represents the gravitational acceleration.
The form of the continuity equation applied to a slab of the deforming tube between x and $x + \Delta x$ yields:

$$\frac{\partial A}{\partial t} + \frac{\partial (uA)}{\partial x} = 0 \tag{1.3}$$

Now, for given $A(x,t)$, we have two equations for $u(x,t)$ and $p(x,t)$ subject to boundary conditions at the entrance and/or exit of the tube and to initial conditions.

The solution for $u(x,t)$ and $p(x,t)$ can be expressed as:

$$\frac{u(x,t)}{u(0,t)} = \frac{A(0,t)}{A(x,t)} - \frac{1}{Q(t)}\frac{A(0,t)}{A(x,t)}\frac{\partial}{\partial t}\int_0^x A(\hat{x},t)d\hat{x} \quad \text{(1.4-a)}$$

$$\frac{p(x,t)-p(0,t)}{\frac{1}{2}\rho u^2(0,t)} = 1 - \frac{u^2(x,t)}{u^2(0,t)} - \frac{2}{u^2(0,t)}\left[\frac{\partial}{\partial t}\int_0^x u(\hat{x},t)d\hat{x} + \int_0^x Ru(\hat{x},t)d\hat{x}\right] \quad \text{(1.4-b)}$$

where $Q(t) = u(0,t)A(0,t)$ is the volume flow.
Once we have a relation between the transmural pressure $p(x,t) - p_{ext}$ and the cross-sectional area $A(x,t)$ the fluid-structure problem can be solved.

2D and 3D flow

Given the large resources required for the numerical solution of the $3D$ problem, much attention has focussed on the $2D$ deformable channel wall problem illustrated in figure 1.5.

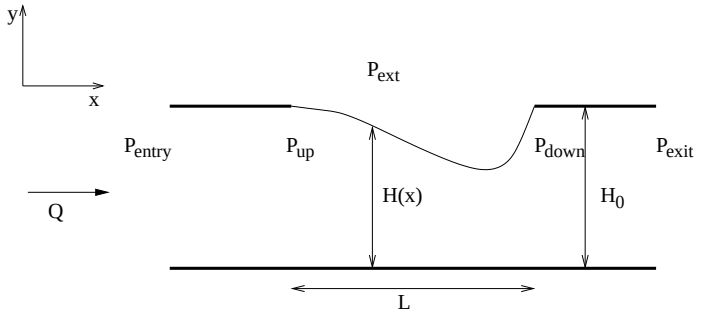

FIGURE 1.5: *Sketch of the $2D$ model problem: viscous flow through a channel in which part of one wall has been replaced by an elastic membrane under tension T_0.*

The flow is governed by the Navier-Stokes equations for $2D$ incompressible flow:

$$\frac{\partial u_i}{\partial x_i} = 0 \quad \text{(1.5-a)}$$

$$\rho\left(\frac{\partial u_i}{\partial t} + u_j\frac{\partial u_i}{\partial x_j}\right) = -\frac{\partial p}{\partial x_i} + \mu\frac{\partial^2 u_i}{\partial x_j \partial x_j} \quad \text{(1.5-b)}$$

where $i = 1,2$ and $j = 1,2$. In equation 1.5-b the index summation convention is used, while μ is the fluid dynamic viscosity, assumed constant. Furthermore:

$$\underline{u}(\underline{x},t) = (u_1(x_1,t), u_2(x_2,t))^T \quad \text{(1.6)}$$

is the $2D$ velocity field.
No-slip conditions are imposed at the walls. Usually, a constant or parabolic velocity profile

is prescribed at the inlet providing the volume flow Q.

An often used approximation to the Navier-Stokes equations is the Stokes equations, which are valid for sufficiently low Reynolds number ([32], [44] and [33]). The inertia effects are assumed negligible compared to the viscous effects, and the flow is considered steady. The Stokes equations are derived as:

$$\frac{\partial u_i}{\partial x_i} = 0 \tag{1.7-a}$$

$$\frac{\partial p}{\partial x_i} = \mu \frac{\partial^2 u_i}{\partial x_j \partial x_j} \tag{1.7-b}$$

where $i = 1, 2$ and $j = 1, 2$.

Assuming that the slope of the wall of the elastic part of the channel is small ($dH/dx \ll 1$), the flow is steady and the fluid inertia is negligible, the flow can be described with lubrication theory, in the limit of low Reynolds number ([41]). In the lubrication theory the pressure gradient is directly related to the volume flow rate through the tube, similar to Poiseuille's flow.

In $3D$ the flow is governed by the same Navier-Stokes equations (1.5-b), with $i = 1, 2, 3$ and $j = 1, 2, 3$. All approximations valid for the $2D$ situation can also be extended to $3D$.

1.4.2 Structural models (1D, 2D, 3D)

1D models

The golden standard of the solution of the $1D$-model of a collapsible tube is given by the tube law ([49]). The tube law considers a long elastic tube subject to a transmural pressure. The tube law describes the functional relationship between the dimensionless transmural pressure:

$$P(\alpha) = \frac{p - p_{ext}}{K_p} = \frac{p_{tm}}{K_p} \tag{1.8}$$

and the dimensionless area:

$$\alpha = \frac{A}{A_0} \tag{1.9}$$

with A_0 the cross-sectional area for $P = 0$.
The parameter K_p is defined as:

$$K_p = \frac{E^{'} I}{R^3} = \frac{E}{12(1-\nu^2)} \frac{h^3}{R^3} \tag{1.10}$$

where E is the Young modulus, ν is the Poisson ratio, R is the undeformed mean radius of the tube and $I = h^3/12$ is the bending moment of the tube wall per unit length in the axial direction, h is the thickness of the tube wall. $E^{'} I$ represents the flexural rigidity.

For $p_{tm} < 0$ the tube is compressed. Initially the tube remains circular in this regime. At a critical pressure the tube buckles and attains an elliptical cross-section. Buckling starts at

$P(\alpha) = -3$. The compression of the tube is counteracted by the bending stresses in the tube wall, specifically in the most highly curved parts of the tube wall. In this regime the tube is highly compliant and a small reduction in p leads to a large change in cross-sectional area. As the inside pressure p decreases further, the opposite walls of the tube come into contact, first at a single point at $\alpha = 0.27$, subsequently along a line at $\alpha = 0.21$ ([49]). Now the cross-sectional shape shows two lobes in which the bending stresses are high and a further reduction of the cross-sectional area is increasingly more difficult. In this regime Flaherty et al. ([12]) have shown that the tube law can be expressed as:

$$P(\alpha) = -\frac{1}{\alpha^{\frac{3}{2}}} \quad for\ \alpha \ll 1 \tag{1.11}$$

However, no reasonable simple analytic relationship $P(\alpha)$ can fit the experimental data over the entire range $\alpha \leq 1$. The modified tube law:

$$P(\alpha) = 1 - \frac{1}{\alpha^{\frac{3}{2}}} \quad for\ \alpha \leq 1 \tag{1.12}$$

can be used as an approximation which approaches equation 1.11 as $\alpha \to 0$ and which produces the correct value $\alpha = 1$ when $P(\alpha) = 0$.

For $P(\alpha) > 0$ the tube preserves its circular cross-section and the tube is very stiff, i.e. the cross-sectional area changes very slowly with increasing internal pressures. For this regime the deformation of the tube can be expressed as ([4]):

$$P(\alpha) = k(\alpha - 1) \quad for\ \alpha > 1 \tag{1.13}$$

where k is a constant.

For the case of steady flow through the (slender) tube without friction and without effects of gravity the fluid-structure interaction problem can be solved. For that case we have from equations 1.4-a and 1.4-b, with $u_0 = u(x = 0), p_0 = p(x = 0)$:

$$\frac{u(x)}{u(0)} = \frac{1}{\alpha} \tag{1.14-a}$$

$$\frac{p - p_0}{\frac{1}{2}\rho u_0^2} = 1 - \frac{1}{\alpha^2} = \frac{p_{ext} - p_0}{\frac{1}{2}\rho u_0^2} + \frac{K_p}{\frac{1}{2}\rho u_0^2}(1 - \frac{1}{\alpha^{\frac{3}{2}}}) \tag{1.14-b}$$

or:

$$C_{p,ext} = (1 - \frac{1}{\alpha^2}) - k_p(1 - \frac{1}{\alpha^{\frac{3}{2}}}) \tag{1.15}$$

where $C_{p,ext} = \frac{p_{ext} - p_0}{\frac{1}{2}\rho u_0^2}$ and $k_p = \frac{K_p}{\frac{1}{2}\rho u_0^2}$ are dimensionless quantities.
For given $C_{p,ext}$ and k_p the cross-sectional area α can be found.
The result for given k_p, i.e. wall stiffness, is presented in figure 1.7. It shows that k_p has to exceed the threshold value of $4/3$ in order to find a solution, i.e. to prevent collapse. For $k_p > 4/3$ two solutions for $\alpha = A/A_0$ are found: a realistic one at larger values of α, and another one at much smaller values of α. The value of $C_{p,ext}$ has to be below a limiting value, i.e.:

$$0 \leq C_{p,ext} \leq 1 - k_p + \frac{1}{3}\left(\frac{3}{4}k_p\right)^4 \tag{1.16}$$

Above the limiting value a solution is not found, indicating that total collapse will occur.

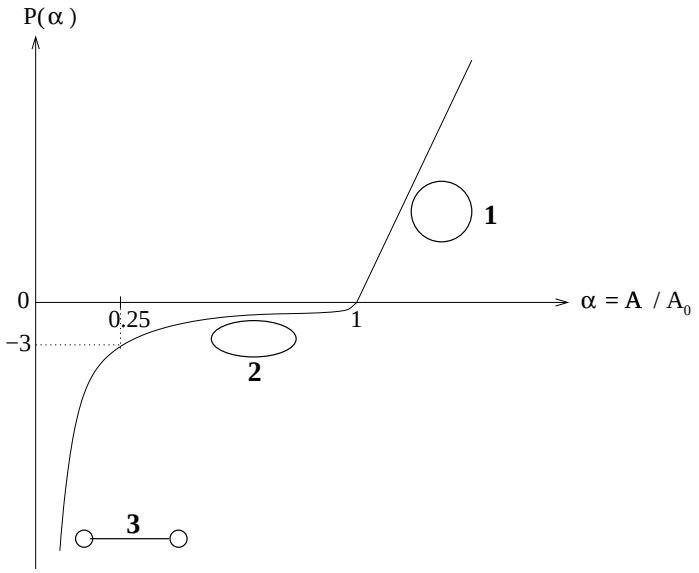

FIGURE 1.6: *Sketch of the tube law: the dimensionless transmural pressure (internal pressure minus the external pressure)* $P(\alpha) = p_{tm}/K_p$ *is given as a function of the ratio of the cross-sectional area of the tube and the cross-sectional area of the non-stressed tube. Sketches of the cross-sectional shapes are given for different stages of the tube deformation.*

2D models

The wall is modeled as a membrane (see figure 1.5) under axial tension T (in N/m). Its deformation, characterized by the variable channel height $h(x)$, is governed by:

$$p_{tm}(x,t) = p - p_{ext} = T\kappa \tag{1.17}$$

where for small slopes of the wall the wall curvature κ (in m^{-1}) can be approximated by:

$$\kappa \approx -\frac{\partial^2 h}{\partial x^2} \tag{1.18}$$

3D models

A general approach to a structural model, capable to describe the deformation of a body, is based on a variational approach, which yields the equation governing the displacement of each point of the body due to a load applied on this body. This model is usually solved by the Finite Element Method (FEM).
Heil ([18]) proposed to solve the deformation of a cylindrical shell, governing the deformation of the wall of the tube through which a steady flow passes, by using a geometrically non-linear Kirchhoff-Love shell theory.

Whatever model used, the properties of a solid material can be described by two quantities, i.e. E and ν:

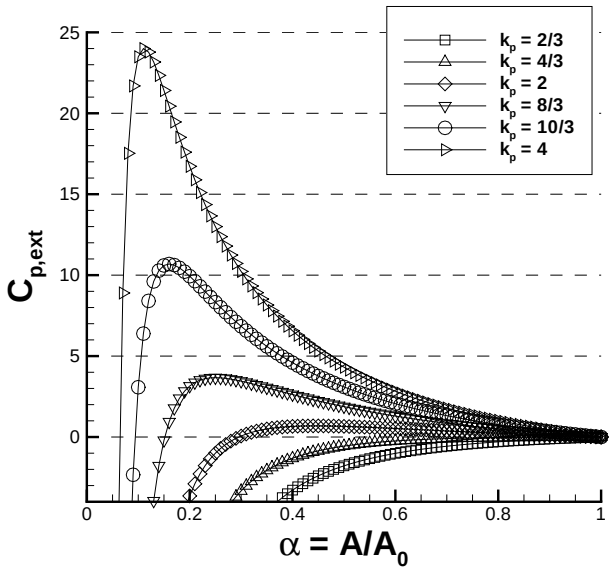

FIGURE 1.7: *Result of coupling the Bernoulli equation for incompressible flow with the tube law.* $C_{p,ext} = \frac{p_{ext}-p_0}{1/2\rho u_0^2}$, $k_p = \frac{K_p}{1/2\rho u_0^2}$.

- *Young modulus* The Young modulus E, or modulus of elasticity, is a characteristic of the elasticity of a material. It is defined as the slope of the stress-strain diagram in the linear elastic regime:

$$\sigma = E\epsilon \tag{1.19}$$

  where σ (expressed in Pascal, or N/m^2) is the stress and ϵ (dimensionless) is the strain. E is expressed in Pascal.

- *Poisson ratio* An element of material will deform when subjected to load, both in axial and lateral direction. The Poisson ratio is defined as:

$$\nu = \frac{lateral\ strain}{axial\ strain} \tag{1.20}$$

  The solid material will be considered as homogeneous and isotropic. The value of ν, considered constant, can range from almost 0 to 0.5.

1.4.3 Examples of flow models

1D flow, 1D tube

The problem of steady, $1D$ flow in a $1D$ tube is traditionally solved (e.g. [49]) by the set of equations formed by the steady part of the continuity equation 1.3, the momentum equation 1.2 and the tube law 1.11:

$$\frac{d(uA)}{dx} = 0 \tag{1.21-a}$$

$$u\frac{du}{dx} = -\frac{1}{\rho}\frac{dp}{dx} - Ru \tag{1.21-b}$$

$$p_{tm}(x) = p(x) - p_{ext} = P(A(x))K_p \tag{1.21-c}$$

The pressure p and the velocity u are averaged over the tube. The effect of gravity on the flow has been neglected. The last term of the second equation, Ru, represents the viscous resistance of the flow and it is assumed that R is positive.
By combining these three equations, the change of area with the length of the tube is found as:

$$\frac{1}{A}\frac{dA}{dx} = \frac{-Ru}{c^2 - u^2} \tag{1.22}$$

where

$$c = \sqrt{\frac{A}{\rho}K_p\frac{dP(A)}{dA}} \tag{1.23}$$

is the speed of propagation of a long, small amplitude pressure (or area) wave along the flexible tube with a cross-sectional area A ([30]).
Assuming the tube law, equation 1.11, to be valid locally, we find:

$$c = \left(\frac{3}{2}\frac{K_p}{\rho}\frac{1}{\alpha^{\frac{3}{2}}}\right)^{\frac{1}{2}} \tag{1.24}$$

so that:

$$\frac{c}{u_0} = \left(\frac{3}{4}k_p\frac{1}{\alpha^{\frac{3}{2}}}\right)^{\frac{1}{2}} \tag{1.25}$$

It then follows that since $k_p \geq 4/3$, see figure 1.7, that $c/u_0 > 1/\alpha^{\frac{3}{4}}$. Since $\alpha \leq 1$ we see that for α close to 1, i.e. small deformations, the propagation speed is slightly above the flow velocity.

Equation 1.22 predicts an interesting phenomenon, known as "choking". Assume that, at the upstream end of the tube, the averaged fluid velocity u is less than the wave speed c. Since $R > 0$, Equation 1.22 implies that $\frac{1}{A}\frac{dA}{dx} < 0$, i.e. the tube cross-sectional area decreases in the direction of the flow. The continuity equation states that $\frac{1}{u}\frac{du}{dx} + \frac{1}{A}\frac{dA}{dx} = 0$ so that $\frac{1}{u}\frac{du}{dx} > 0$, i.e. the flow is accelerated in the streamwise direction. Provided the tube is long enough, we will therefore approach a location at which the "speed index" $S = u/c \to 1$ and thus $dA/dx \to -\infty$, the tube collapses. Clearly, this situation is physically unrealisable, implying that steady flows are impossible if the flow rate becomes so large that u approaches c anywhere in the tube. Alternatively, if $S > 1$ at some point along the tube, then variations in downstream conditions cannot propagate upstream. This underlies the wave-speed mechanism of flow limitation that is believed to govern the flow in large airways at high speeds ([9]).
Having identified a collapse mechanism which is similar to the chocking mechanism found in the flow of compressible gases, one might expect the $1D$ collapsible tube equations to have shock-like solutions similar to those in gas flows through Laval nozzles. Experimentally, shock-like structures (known as "elastic jumps") in collapsible tube flow are easily generated (see e.g. [27]). Within the framework of the $1D$ model(see figure 1.8), elastic jumps are

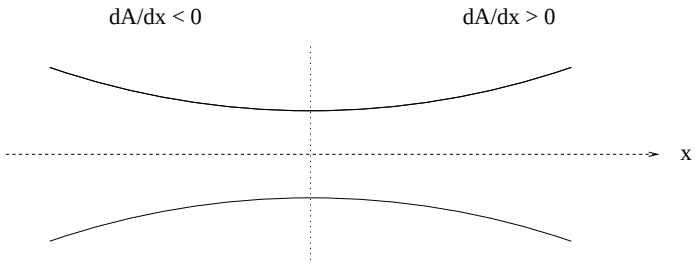

FIGURE 1.8: *Convergent / divergent elastic tube.*

predicted to occur in situations where supercritical ($S > 1$) flow is generated somewhere in a collapsible tube. Experimentally, this is done most effectively by pinching the tube at a far upstream location; the reduction in cross-sectional area increases the fluid velocity u while the reduction in wall stiffness simultaneously reduces the wave-speed c. The ensuing supercritical flow is still governed by equation 1.22, which now predicts that $dA/dx > 0$. Hence the cross-sectional area A increases and, provided the tube is long enough, the reduction in fluid velocity u now leads to a situation in which $dA/dx \to \infty$ at some point. As in the case of choking, this locally violates the model's assumptions. However, a shock-like transition region, in which the flow speed is reduced from super- to subcritical, can instead develop upstream of the point where $dA/dx \to \infty$ would occur. The application of jump conditions (similar to those used in gas dynamics) across the elastic jump ([39], [49], [7]) establishes how the flow changes as it passes from the supercritical to the subcritical regime. The location of the elastic jump is determined by the downstream boundary conditions, which can influence only the subcritical region of the flow downstream of the jump. Standing waves can appear either upstream or or downstream of elastic jumps through the effects of longitudinal bending or tension, attenuated by viscous effects ([38], [8]).

To describe flows in the Starling Resistor (see figure 1.4), the governing equations 1.2, 1.3 and 1.10 must be supplemented by boundary conditions describing the rigid parts of the system. The tube area must also be prescribed at either end of the collapsible tube, where it is mounted onto the rigid pipes ($A_{up} = A_{down} = A_0$). However, with the model given by equations 1.2, 1.3 and 1.10, it is only possible to prescribe the cross-sectional area at a single location. To overcome this problem, Mc Clurken et al. ([38]) augmented the tube law, which only represents the effect of the tube's transverse bending stiffness, by terms which represent the effects of the wall elasticity in the axial direction:

$$p_{tm} = K_p P(A) - T\frac{d^2 A}{dx^2} \tag{1.26}$$

where T is the longitudinal tension in N/m.

Another improvement to the $1D$ model was proposed by Cancelli and Pedley ([4]). The flow very likely will separate just downstream of a constriction that appears in the highly collapsed part of the tube. This implies that the energy loss in the flow is enhanced and therefore incomplete pressure recovery will occur in the region downstream of the narrowest point. To model this loss, the momentum equation 1.2 was replaced, downstream of the narrowest

point, by:

$$\chi u \frac{du}{dx} = -\frac{1}{\rho}\frac{dp}{dx} \tag{1.27}$$

where χ is a dimensionless non-negative quantity, less than 1.

The steady flow model described by equations 1.3, 1.26 and 1.27, which for the sake of clarity is repeated here as:

$$\frac{d(uA)}{dx} = 0 \tag{1.28-a}$$

$$\chi u \frac{du}{dx} = -\frac{1}{\rho}\frac{dp}{dx} \tag{1.28-b}$$

$$p - p_{ext} = K_p P(A) - T\frac{d^2 A}{dx^2} \tag{1.28-c}$$

The tube law is given by equation 1.12:

$$P(A) = 1 - \alpha^{-\frac{3}{2}} \quad for\ \alpha < 1 \tag{1.29}$$

This model was exhaustively analyzed by Jensen and Pedley ([25]).
In larger arteries the small viscous losses represented by R in equation 1.2 were found to be of minor importance and were therefore neglected. Jensen and Pedley found that, in the case of $\chi = 1$ everywhere in the tube, there is a critical value of the flow rate Q, that depends on the longitudinal tension T, above which the steady flow problem has no solution, i.e. the presence of the longitudinal tension alone does not prevent choking. However, when $\chi < 1$ after the point of maximum constriction, i.e. the loss due to flow separation is taken into account, a steady solution exists for all positive values of the flow rate Q and longitudinal tension T. Since such loss exists, it follows that the breakdown of steady flow is not caused by choking but must arise from instability of the steady flow solution.

2D flow, 2D tube

Given the large resources required for the numerical solution of the $3D$ problem, much activity in the 1990's has focussed on the $2D$ deformable tube problem illustrated in figure 1.5. The flow is governed by the $2D$ Navier-Stokes equations (equation 1.5-b). The wall is modelled as a membrane under axial tension (equation 1.17).
One of the first articles treating this problem is of Pedley ([41]). The model is based on the lubrication theory, which assumes a small membrane slope and a very low Reynolds number. It is shown how steady flow solutions of the fluid flow may break down if the fluid shear stress reduces the wall tension to zero at some point along the wall.
In a more recent article, Matsuzaki and Fujimura ([37]) combined the flow method with a structural method (equation 1.17) that includes bending stiffness in the tube law. That ensures the existence of steady flow solutions for all values of the tension.
Jensen ([24]) also used lubrication theory to obtain explicit pressure-flow relations for a highly collapsed channel that exhibits flow and pressure-drop limitation through purely viscous mechanisms.
However, even for low Reynolds number flow, the lubrication theory analysis is not valid

because the wall slope becomes large at the downstream end in cases for which the wall tension is small. The next stage was therefore the numerical simulation of the equations of Stokes, coupled with the membrane equations. This was performed by Lowe and Pedley ([32]). The flow equations were solved with a finite element method. Assuming the membrane position given, the pressure and shear stress exerted on the membrane are calculated, after which the membrane position is updated by requiring that the membrane equilibrium equations to be satisfied. This iterative procedure leads to the prediction of the membrane shape, which agreed remarkably well with the lubrication theory results, even when the wall slope was quite large. However, it failed to give a solution for sufficiently small values of the membrane tension.
Rast ([44]) and Luo and Pedley ([33]) performed detailed studies of the flow at finite Reynolds numbers, using the Navier-Stokes equations to describe the flow. Strong collapses of the channel ($\sim 70\ \%$ of the channel width) could be achieved. Downstream of the point of maximum collapse the flow field is similar to that found in the flow over a step. With increasing Reynolds number, recirculating eddies arise. Unfortunately, it appeared to be difficult to obtain convergence for low values of the wall tension. Somehow, below a critical value of the wall tension, depending on the Reynolds number, a solution could not be obtained.

3D flow, 3D tube

The flow in a collapsible tube has been discussed extensively in the 1970's, 1980's and early 1990's, whether from an experimental point of view (Starling resistor) or employing numerical methods using a $1D$ or $2D$ description of the most important physical features involved. However, and despite considerable progress in the understanding of the physics involved, the 1 or $2D$ models miss many potentially important effects such as:

- the significant differences between flow separation in $2D$ and $3D$ flows ([51]).
- the drastic changes in wall stiffness as the tube changes from an axi-symmetric to a non-axi-symmetric buckled state.

The first step to a $3D$ model was made by Heil ([18], [21]). A geometrically non-linear Kirchhoff-Love shell theory (e.g. [54]) was used to describe the tube wall and the lubrication theory for tube flow calculation.
The collapsible tube was modelled as a thin-walled elastic shell (of length L_0, radius R_0 and wall thickness h) which deformation was described by large-displacement, geometrically non-linear shell theory. A linear stress-strain relationship with two elastic constants (Young modulus E and the Poisson ratio ν), was used in the constitutive equation. The tube's undeformed geometry was described by the position vector $\underline{r}_\omega(\zeta^1,\zeta^2)$ on the tube's mid-plane which was parametrised by two Lagrangian coordinates ζ^1 and ζ^2. The vector field $\underline{v}(\zeta^1,\zeta^2)$ which displaces material particles to their new positions $\underline{R}_\omega = \underline{r}_\omega + \underline{v}$ was determined from the principle of virtual displacements:

$$\int_0^{2\pi}\int_0^{L_0/R_0}\left[E^{\alpha\beta\gamma\delta}\left(\gamma_{\alpha\beta}\delta\gamma_{\gamma\delta}+\frac{1}{12}\left(\frac{h}{R_0}\right)^2\kappa_{\alpha\beta}\delta\kappa_{\gamma\delta}\right)-\left(\frac{R_0}{h}\right)(\underline{f}.\delta\underline{R}_\omega)\right]d\zeta^1 d\zeta^2 = 0 \tag{1.30}$$

where $\gamma_{\alpha\beta}$ and $\kappa_{\alpha\beta}$ are the mid-plane strain and bending tensors, respectively, and $E^{\alpha\beta\gamma\delta}$ represents the fourth order tensor of elastic constants; see Heil and Pedley ([21]) for details.

The load vector $\underline{f}$ is given by the combination of the external pressure and the traction that the fluid exerts onto the tube wall. A finite-element method was used to discretise the variational equation 1.30.

In subsequent papers, the lubrication theory was abandoned as the model for the flow computation and replaced by the Stokes equations ([19], [20]). The flow is assumed to be at low or zero-Reynolds number. Figures 1.9 and 1.10 show the results of the deformation of the tube. Figure 1.9 is related to a short tube ($L/D = 2.5$), three-lobe deformation. Figure 1.10 shows different stages of the collapse of a longer tube ($L/D = 5$).

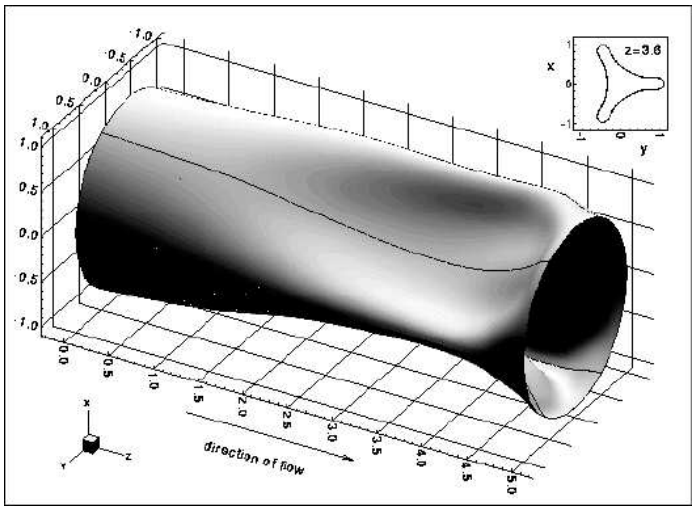

FIGURE 1.9: *Large deformation of a cylindrical shell conveying viscous flow ([19]). The tube has buckled in three lobes (a cross-section of the deformed tube is shown in the top right-hand corner).*

Continuing in that direction, a finite-Reynolds-number model was introduced by replacing the low-Reynolds number flow Stokes model ([17]) by the Navier-Stokes equations for steady flow.

1.4.4 Unsteady flow models

1D

The first step to an unsteady flow model was made by Jensen ([22]). He gave a detailed linear, and weakly non-linear, analysis of the instability of the steady flow. The model used is the same as the steady, $1D$ flow model with the addition of times derivatives $\partial A/\partial t$ and $\partial u/\partial t$ to the mass equation and the modified momentum equation 1.27, respectively. The elasticity equations 1.26 and 1.12 remain unchanged:

$$\frac{\partial A}{\partial t} + \frac{\partial (uA)}{\partial x} = 0 \qquad \text{(1.31-a)}$$

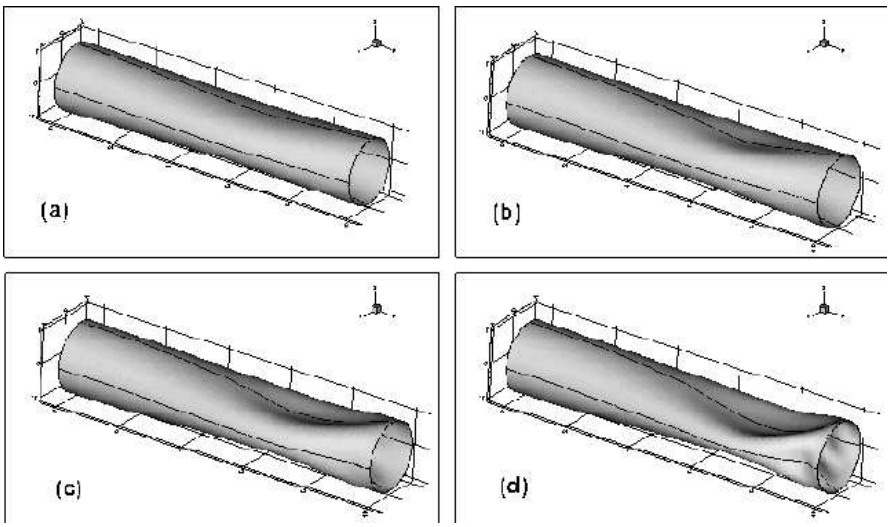

FIGURE 1.10: *Four stages of the axi-symmetrical, three-dimensional deformation of a cylindrical shell (Heil, M.).*

$$\frac{\partial u}{\partial t} + \chi u \frac{\partial u}{\partial x} = -\frac{1}{\rho}\frac{\partial p}{\partial x} \tag{1.31-b}$$

$$p_{tm}(x) = K_p P(A(x)) - T\frac{\partial^2 A}{\partial x^2} \tag{1.31-c}$$

In a subsequent paper, Jensen ([23]) showed results that are similar to the experiments conducted by Bertram et al. ([3]). However, this work was abandoned, because of the severe *a priori* weaknesses of the $1D$ model: first, the solid mechanics involved (e.g. the non-axisymmetric, large deformation of a cylindrical shell) is not well described; second, the fluid mechanics is also rudimentary, primarily because of the *ad hoc* way of representing flow separation and the processes of energy loss and pressure recovery downstream of the constriction. Furthermore, the arguments leading to equation 1.27 were based on steady flow, weakening even more the unsteady flow model.

2D

Unsteady finite-Reynolds-number flows in collapsible channels have been computed by Luo and Pedley ([34], [35], [36]), Liang et al. ([29]) and Pedrizetti ([42]. Given the important role that the wall tension T appeared to play for steady flows, Luo and Pedley ([34]) investigated the system's time-dependent behaviour for different values of T. They found that, for sufficiently large Reynolds number, self-excited oscillations develop when the tension is reduced below a critical value.

3D

Till now, no unsteady $3D$ flow/structure models have been developed.

1.5 Objectives

For 30 years, research on flow in collapsible tubes has been carried out. The initial purpose ([30]) was to describe the flow of blood in veins.
Rapidly, this subject captured the curiosity of many researchers. The flow in collapsible tubes, an easy and straightforward problem at first sight, will reveal itself to be much more complicated than expected: interaction between flow and tube wall, complexity of the flow itself (three-dimensional behaviour, wide range of velocities due to the possible extreme narrowing of the tube), turbulence, boundary layers, flow separation, are just an outline of the complexity of the problem.
The Starling Resistor is a simple experimental device in which many of the features expected to be relevant in biological flow are simulated. An elastic tube (made of rubber for example) with its extremities held fixed, placed in a pressurized chamber, conveys a fluid flow (water, air), with the Reynolds number controlled by means of pressure control at the ends of the tube. The deformation of the tube, as well as the flow behaviour can be observed.
For this configuration theoretical models have been developed:

- lumped parameter models were the first approach, as it is the simplest. However, these models are a too crude approximations of the physical reality.
- $1D$ models were developed next. These $1D$ models give already insight in the phenomena observed.
- The flow in $2D$ channels, in which one part has a collapsible wall, has been studied, both for steady and unsteady flow. Interesting results were found with these models.
- $3D$ models were developed in the 1990's ([18]). They range from the simplest (lubrication theory) to more elaborate (Navier-Stokes equations) flow models, coupled to the non-linear Kirchoff-Love theory for deforming shells in steady flow calculations and large deformation of a tube could be achieved.

The research described above consider the flow as incompressible. This may be due to the circumstance that the problem considered described fluid flow such as blood. However, in the human lungs air flows through a compliant tube and due to the deformation the cross-sectional area decreases, the velocity increases and compressibility effects may become important.

The need for a model of the air flow in human lungs is a $3D$, fluid-structure coupled, unsteady flow model, capable of compressible flow calculations, large deformation of the tube, and with reduced computation time. In this thesis, the tube wall will be three-dimensional, in order to model the tube deformation as realistic as possible. However, a $1D$ flow model, either incompressible or compressible, will be used to reduce calculation time. The loss of any three-dimensional flow effects, such as boundary layer effects and flow separation resulting in eddies downstream of the constriction of the deformed tube is an approximation, but a full $3D$ model, capable of unsteady, both incompressible and compressible flow calculations, applied in the complex system of branching tubes that a human lung is, would not be feasible because of the extreme computing times required.

FLOW MODELING

CHAPTER 2

In this chapter the airflow in a single tube is investigated.
In a straight, undeformable tube, the entrance length of a Poiseuille flow for different Reynolds numbers is discussed. In relation with typical Reynolds numbers that occur in the lung, depending on the generation of the tube considered, it will be shown that a 1D model for the flow is sufficient during normal respiration.
For the Reynolds numbers considered, and for normal respiration, i.e. small deformation of the tubes, an incompressible flow model based on Bernoulli's relation is adequate. This flow model is presented in the second section.
However, during forced expiration, large deformations occur. In the case of strong collapse of the tube, the flow can become compressible. In that case, a flow model based on the relations for isentropic compressible flow or a flow model based on the Euler equations is needed. These flow models are presented in the third section.

2.1 Flow in branching tubes: entrance length

2.1.1 Reynolds numbers in lung tubes

The lung can be modeled as a system of branching tubes. To estimate the Reynolds number throughout the lung, the human lung model described by Hansen and Ampaya ([16]) is used, which is an extension of the Weibel's model ([53]), see the description in the chapter 1. This model gives for each of the 27 generations the number of tubes and their dimensions (diameter, length). By multiplying the number of tubes in generation n with the cross-sectional area of a tube, the total cross-sectional area of the tubes of one generation can be calculated. With a known tidal volume and breathing pattern, it is possible to estimate the mass flow, and thus the Reynolds number, for each individual tube of a certain generation.

Normal respiration

The volume-flow rate $Q(t)$ for normal respiration can be approximated as:

$$Q(t) = \frac{\pi TV}{t_0} \sin\left(\frac{2\pi t}{t_0}\right) \tag{2.1}$$

where TV is the tidal volume (cm^3), i.e. the volume of air involved in a normal inspiration or expiration, and t_0 is the period of one breathing cycle (second). For normal respiration of

an adult human, $TV = 500\ cm^3$ and $t_0 = 5\ s$. We find the maximum flow rate at $t = \frac{t_0}{4}$ as $Q_{max} = 100\pi\ cm^3/s \simeq 0.314\ l/s$. The Reynolds number in each generation is calculated as:

$$Re_D = \frac{U_n D_n}{\nu} \tag{2.2}$$

where U_n is the maximum velocity of the flow, D_n is the diameter of the tube of the n^{th} generation and ν is the kinematic viscosity of air taken here as: $13.3 * 10^{-6}\ m^2/s$. The velocity U_n in a generation is calculated from the mass flow Q_n and the total cross sectional area of the generation $S_{tot,n}$:

$$U_n = \frac{Q_{max}}{S_{tot,n}} = \frac{Q_{max}}{N_n \frac{\pi}{4} D_n^2} \tag{2.3}$$

In figure 2.1, the Reynolds number is given for the 27 generations of the Hansen and Ampaya's model ([16]). In the upper figure, the Reynolds number is given as a function of the cumulative length, whereas in the bottom figure, it is given as a function of the generation number. The Reynolds numbers depicted are the maximal values, which are calculated during maximum flow rate (i.e. at $t = t_0/4$, see equation 2.1).
The Reynolds number is smaller than 2300, which is the upper limit of the steady flow in a tube to remain laminar. The flow is therefore assumed to be laminar during normal breathing, everywhere in the lung airways.
Furthermore, the Reynolds number is very low ($Re \leq 1$) in the last generations ($n > 15$), which means that viscous effects are predominant in this region. However, these last generations represent a small part of the lung, as seen in the upper part of figure 2.1 where Re_D is plotted as function of the location in the lung. From figure 2.1 it can be concluded that during normal respiration the flow can considered to be inviscid. This approximation is valid for the most part of the lung.

Forced expiration

During forced expiration, the flow velocities in the lung tubes increase substantially. Especially, the flow in the first generations will certainly become turbulent.
In figure 2.2, the Reynolds number, calculated for a maximum flow rate of $Q = 10\,l/s$ (for a healthy adult human the maximum expiratory flow rate is an order of magnitude higher than the one for a normal expiration), is given, as a function of the generation number and the cumulative length. As expected, the flow will be laminar in most of the lungs, and turbulent for the first five generations.

2.1.2 Laminar flow in a tube

Assume a tube with a uniform velocity at the entrance. Because of the no-slip condition at the wall, the wall velocity is zero and a boundary layer develops along the wall. The speed of the fluid in the boundary layer is reduced. Since conservation of mass is required, the velocity at the centerline of the tube increases. Infinitely far downstream from the inlet, the flow profile has become parabolic - zero velocity at the wall, maximum velocity at the centerline of the tube and no longer variation in axial direction: the flow is fully developed (see figure 2.3). It is also referred to as Poiseuille flow. The distance between the inlet and the location at which the flow is fully developed is called the entrance length (see [48]).

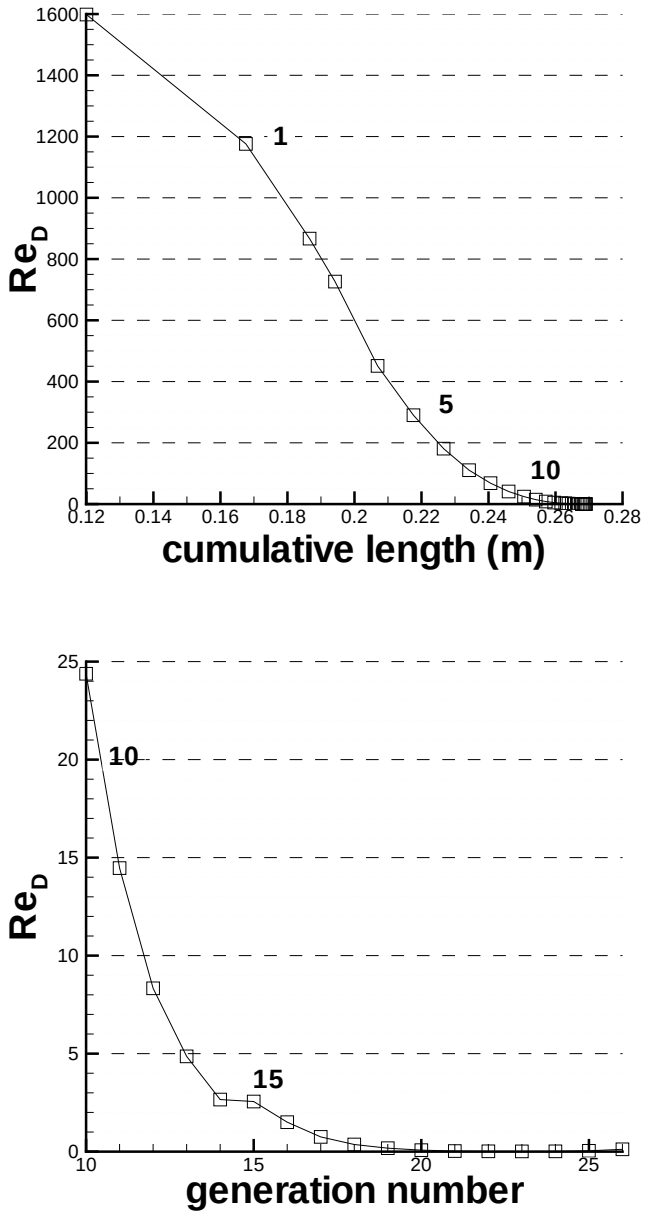

FIGURE 2.1: *Reynolds number versus cumulative length at end of each generation and generation number. The [16] lung model is used to describe the geometry of the lung. The volume-flow* $Q_{max} = 100\pi\ cm^3/s$ *used corresponds to normal respiration.*

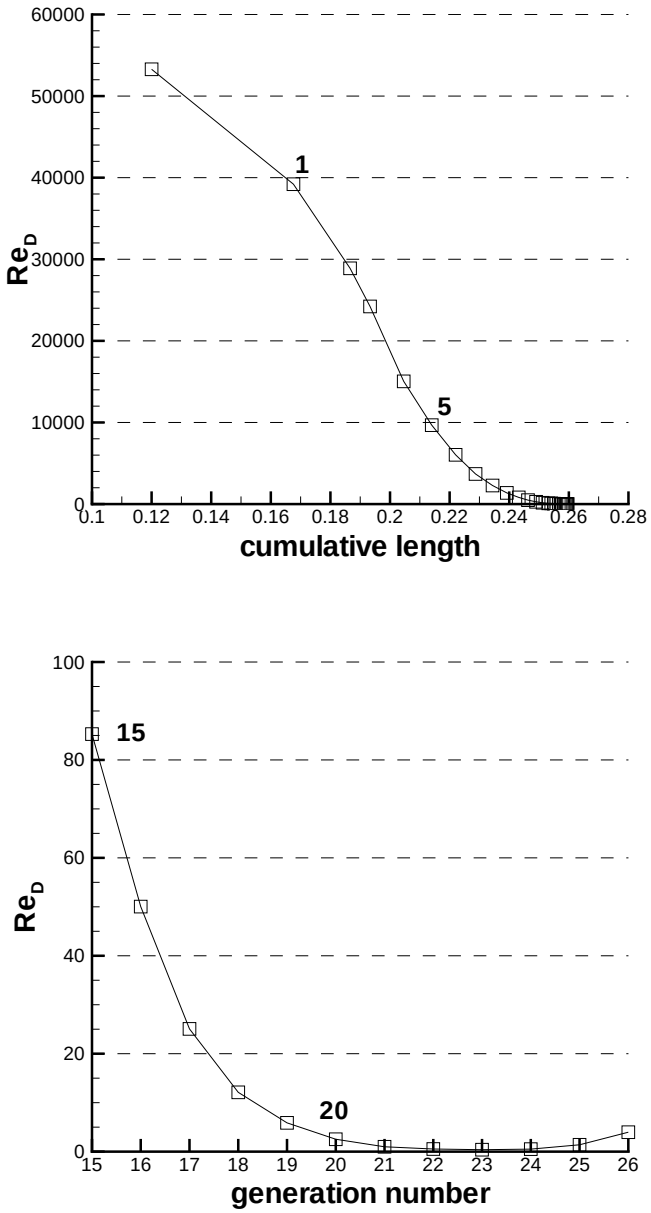

FIGURE 2.2: *Reynolds number versus cumulative length at end of each generation and generation number. The [16] lung model is used to describe the geometry of the lung. The volume-flow* $Q_{max} = 10\, l/s$ *used corresponds to forced expiration.*

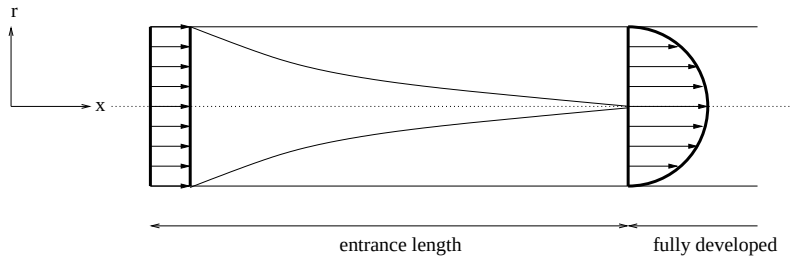

FIGURE 2.3: *Establishment of a Poiseuille flow in a circular pipe: a uniform velocity profile is applied at the entrance; a parabolic velocity profile develops after some length.*

Poiseuille flow

Consider an infinitesimal annular control volume ($2\pi r$, dr, dx) in a tube in which the flow is axi-symmetric and fully developed (see figure 2.4). Two kinds of axial forces apply on this

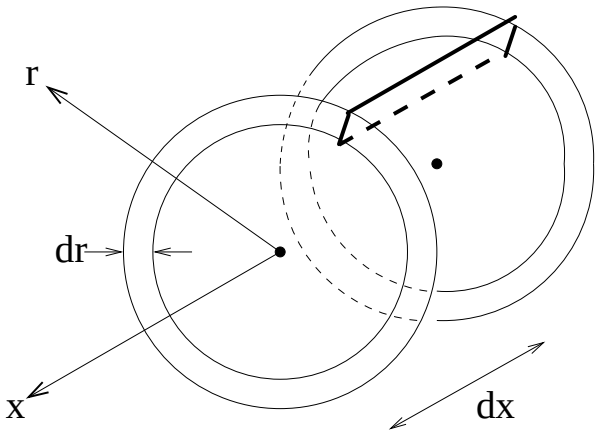

FIGURE 2.4: *Sketch of the annular control volume, bounded by two cross-sectional planes, a cylinder of radius r and a cylinder of radius $r + dr$.*

control volume: pressure forces act on the left and right, shear forces act on the inner and outer cylindrical surfaces of the control volume (see figure 2.5).

- pressure forces

$$\begin{array}{cc} p2\pi r dr & left \\ -\left(p + \frac{\partial p}{\partial x} dx\right) 2\pi r dr & right \end{array} \tag{2.4}$$

- shear forces

$$\begin{array}{cc} -\tau_{rx} 2\pi r dx & inner \\ \left(\tau_{rx} + \frac{\partial \tau_{rx}}{\partial r} dr\right) 2\pi (r + dr) dx & outer \end{array} \tag{2.5}$$

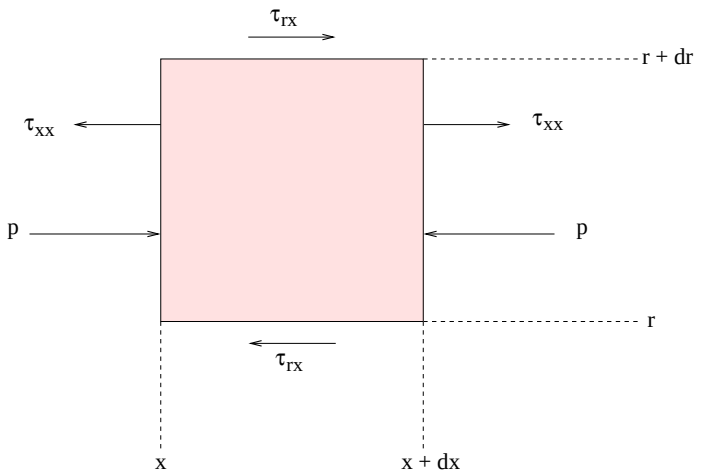

FIGURE 2.5: *Control volume: normal (pressure) and shear (tangential) forces.*

In a fully developed flow the velocity field does not depend on x and the cross-section velocity components are zero, i.e.:

$$\begin{aligned} u(x,r) &= u(r) \\ v(x,r) &= 0 \\ w(x,r) &= 0 \end{aligned} \tag{2.6}$$

so that τ_{xx} will be zero. Also the pressure will depend x only, i.e.:

$$p(x,r) = p(x) \tag{2.7}$$

The sum of the x-component of the forces acting on the control volume must be zero:

$$-\frac{dp}{dx}2\pi r dr dx + \tau_{rx}2\pi dr dx + \frac{\partial \tau_{rx}}{\partial r}2\pi r dr dx + h.o.t. = 0 \tag{2.8}$$

By dividing equation (2.8) by $2\pi r dr dx$, neglecting higher-order terms (h.o.t.) and integrating with respect to r from the pipe axis ($r = 0$) to r, we obtain:

$$\tau_{rx} = \frac{r}{2}\left(\frac{dp}{dx}\right) + \frac{c_1}{r} \tag{2.9}$$

with c_1 a constant.
For a Newtonian fluid, the shear stress is defined as:

$$\tau_{rx} = \mu\frac{du}{dr} \tag{2.10}$$

With equation 2.9 the velocity u can then be derived as:

$$u(r) = \frac{r^2}{4\mu}\left(\frac{dp}{dx}\right) + \frac{c_1}{\mu}\ln r + c_2 \tag{2.11}$$

where c_2 is a second constant. Since at $r = 0$ the velocity must be finite, it follows that:

$$c_1 = 0 \tag{2.12}$$

The no-slip condition at the pipe wall, i.e. $u = 0$ at $r = R$, permits to determine c_2 as:

$$c_2 = -\frac{R^2}{4\mu}\left(\frac{dp}{dx}\right) \tag{2.13}$$

The velocity can now be expressed as:

$$u(r) = \frac{R^2}{4\mu}\left(\frac{dp}{dx}\right)\left(1 - \frac{r^2}{R^2}\right) \tag{2.14}$$

Volume flow rate
From the velocity, the volume flow rate Q through the pipe can be calculated as:

$$Q = \int_A \vec{V}.d\vec{A} = \int_0^R u(r)2\pi r dr \tag{2.15}$$

or:

$$Q = -\frac{\pi R^4}{8\mu}\left(\frac{dp}{dx}\right) \tag{2.16}$$

in m^3/s.
Average velocity
The average velocity is defined as:

$$\overline{V} = \frac{Q}{A} = \frac{Q}{\pi R^2} \tag{2.17}$$

So:

$$\overline{V} = -\frac{R^2}{8\mu}\left(\frac{dp}{dx}\right) \tag{2.18}$$

Point of maximum velocity
The point of maximum velocity can be found by setting $\frac{du}{dr} = 0$ and solving for the corresponding r. From equation (2.14), follows:

$$\frac{du}{dr} = \frac{1}{2\mu}\left(\frac{dp}{dx}\right) r \tag{2.19}$$

$\frac{du}{dr}$ is equal to zero at $r = 0$. The maximum velocity at $r = 0$ becomes:

$$u_{max} = -\frac{R^2}{4\mu}\left(\frac{dp}{dx}\right) = 2\overline{V} \tag{2.20}$$

The velocity profile can be rewritten in terms of the maximum velocity as:

$$\frac{u(r)}{u_{max}} = 1 - \left(\frac{r}{R}\right)^2 \tag{2.21}$$

Pressure drop

In a fully developed flow, the pressure gradient $\frac{dp}{dx}$ is constant. So the pressure drop Δp over a pipe of length L is found from:

$$\frac{dp}{dx} = -\frac{\Delta p}{L} \tag{2.22}$$

The pressure drop Δp can then be expressed in terms of average velocity $\overline{V}$ and the pipe diameter as:

$$\Delta p = 32\mu\overline{V}\frac{L}{D^2} \tag{2.23}$$

The pressure drop can also be expressed as a function of the Reynolds number Re_D by:

$$\Delta p = \frac{64}{Re}\frac{\rho\overline{V}^2}{2}\frac{L}{D} \tag{2.24}$$

where $Re_D = \frac{\rho\overline{V}D}{\mu}$.

2.1.3 Entrance length

The entrance length is the distance between the inlet and the location at which the flow is fully developed. Here this will be investigated in more detail using Computational Fluid Dynamics (CFD). The obtained results will be compared with empirical relations, for typical lung tubes, and for various flow regimes. It will be shown that the length of typical lung tubes is smaller than the entrance length, for the conditions that are observed during both normal respiration and forced expiration.

Calculations of entrance length in a straight tube

Calculations are performed using the commercial CFD package StarCD.
A long tube is considered ($L \gg D$, where L is the length of the tube and D its diameter) to make sure that eventually a fully developed flow will arise. The mesh used for all calculations is presented in figure 2.6 and counts 36000 cells (9 in azimuthal direction, 40 in radial direction and 100 in axial direction). Only the first part of the tube is shown.
A constant velocity of magnitude $\overline{V}$ is set at the inflow boundary. Once the numerical solution has been obtained the location of the axial coordinate at which the flow has become parabolic is determined. The length it takes the flow to become parabolic, i.e. the entrance length, is taken when the maximum velocity, which appears at the centerline of the tube, approaches $2\overline{V}$, i.e. the result from the analytical solution (see equation 2.20). An error of a few percents is allowed, and the results are presented with errors of $1, 2, 3, 4$ and 5 percent in figure 2.7.
The entrance length, expressed in terms of the number of tube diameters, is plotted as a function of the Reynolds number. The Reynolds numbers used in the calculations range from 50 to 500. Such Reynolds numbers are typical for most of the generations of the lungs during normal respiration.

It is obvious that the entrance length increases when the allowed error is reduced. For instance the entrance length for which the deviation from the maximal velocity is less than 1 percent is double that if the entrance length for which a deviation of 5 percent of the maximal velocity is allowed.

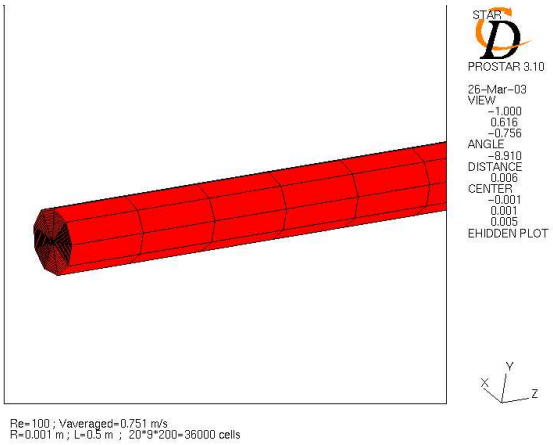

FIGURE 2.6: *StarCD mesh used for calculations of the entrance length. The mesh is equidistant in each direction.* $D = 0.002\ m$, $L = 0.5\ m$, $100 * 40 * 9$ *cells in* x, r *and* θ *direction.* $\overline{V} = 0.751\ m$, $Re_D = 100$.

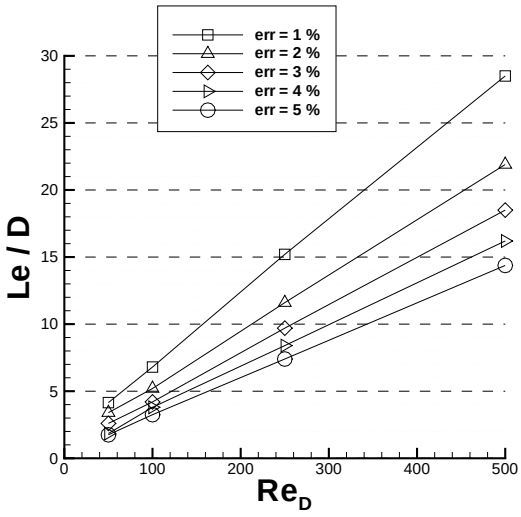

FIGURE 2.7: *Entrance length in a straight tube, for various Reynolds numbers* $Re_D = \frac{\rho \overline{V} D}{\mu}$. *The entrance length is here defined as the length at which the maximum calculated velocity is equal to the analytical maximum velocity* $2\overline{V}$, *with an error of* $1, 2, 3, 4$ *and* 5 *percent.*

For typical lung tubes, $L/D \sim 2$, and in any case $L/D < 5$. The calculated entrance lengths are mostly far above this value. For low Reynolds numbers, the entrance length is of the order of the length of a lung tube. The flow might then become fully developed somewhere near the end of the tube. However, in the lung such Reynolds numbers do not occur in many cases. For normal respiration, typical Reynolds number range from 1 to 1600 (see figure 2.1). For

forced expiration, Reynolds numbers range from 1 to 60000 (see figure 2.2). Obviously, the largest part of the lung, during normal respiration or even more during forced expiration, the flow cannot be considered as fully developed.

Entrance length versus Reynolds number relations

Various authors have proposed empirical relations for laminar flow ($Re_D \leq 2500$)to express the entrance length L_e as a function of the diameter D of the tube and of the Reynolds number $Re_D = UD/\nu$.
Nikuradse (see [48]), derived from measurements:

$$\frac{L_e \nu}{R^2 U} = 0.04 \quad \text{or} \quad \frac{L_e}{D} = 0.01 Re_D \tag{2.25}$$

where ν is the kinematic viscosity, $R = \frac{D}{2}$ is the radius of the tube and U is the averaged velocity in a section of the tube.

Schiller (1922) (see [47]):

$$\frac{L_e \nu}{R^2 U} = 0.115 \quad \text{or} \quad \frac{L_e}{D} = 0.029 Re_D \tag{2.26}$$

Schlichting (1934) (see [48]):

$$\frac{L_e \nu}{R^2 U} = 0.16 \quad \text{or} \quad \frac{L_e}{D} = 0.04 Re_D \tag{2.27}$$

Langhaar (1942) (see [28]):

$$\frac{L_e \nu}{R^2 U} = 0.232 \quad \text{or} \quad \frac{L_e}{D} = 0.058 Re_D \tag{2.28}$$

The entrance lengths from these authors, expressed in terms of number of diameters, are plotted for different Reynolds numbers in figure 2.8. These semi-empirical results are in accordance with the ones found from the calculations (see figure 2.7), specifically when comparing with the more recent proposed relations.
The most recent results ([28]) do match with an accuracy of 99 percent for the maximal velocity. Of course one can question which error should be used in practice. Theoretically, for a given discretization, the entrance length will become infinitely long when the accepted error is required to be zero. In the calculations an error of the maximal velocity less than a certain percentage has been chosen. However, one can imagine that a quantity like:

$$L_2(x) = \frac{1}{V} \sqrt{\frac{1}{\pi R^2} \int \int_{\Omega} (u(x,r)_{starCD} - u(x,r)_{analytic})^2 d\Omega} \tag{2.29}$$

where Ω denotes the cross-section,is more appropriate.
The result of this section is that during forced expiration (and even during normal breathing), fully developed pipe flow will not occur in the larger airways since the Reynolds number in

these tubes are higher than 50. For this Reynolds number L_e/D becomes in the order of 2.5, which fits the geometric properties of a human lung.
A further implication is that to first approximation the flow can be considered inviscid, i.e. the effects of viscosity are negligible, since in the developing flow the boundary layers remain relatively thin. This is a reasonable approximation for most of the lungs, except for the last generations, where the Reynolds number is small.

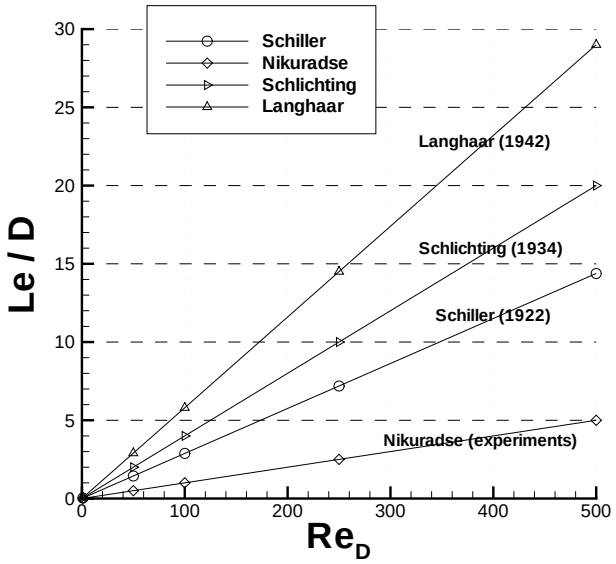

FIGURE 2.8: *Entrance length in straight tubes versus Reynolds number: empirical relations from various authors.*

2.2 Incompressible fbw

For most of the time during normal respiration, and at least during some stages of forced expiration, the air flow will behave as an incompressible flow, i.e. the compressibility effects are negligible. Only in the case when the tubes are strongly collapsed, the Mach number might become high enough to question this hypothesis. Then a compressible flow model is needed.
We will now describe the steady, quasi-1D, inviscid, incompressible flow model

Continuity equation

Considering a fixed control volume ϑ bounded by a surface Γ, the continuity equation can be expressed in integral form as:

$$\frac{\partial}{\partial t}\int_{\vartheta}\rho d\vartheta + \int_{\Gamma}\rho\overrightarrow{V}.d\overrightarrow{A} = 0 \tag{2.30}$$

where $\overrightarrow{V}$ is the velocity and $d\overrightarrow{A} = \overrightarrow{n}dA$ is the surface area normal vector.
Since the flow is considered steady, the first term of equation 2.30 is zero. Therefore, for the control volume formed by the tube wall and two consecutive cross flow planes, equation 2.30 becomes:

$$\int_{\Gamma}\rho\overrightarrow{V}.d\overrightarrow{A} = -\rho_1 V_1 A_1 + \rho_2 V_2 A_2 = 0 \tag{2.31}$$

For an incompressible flow, $\rho_1 = \rho_2$. The continuity equation can then be expressed as:

$$V_1 A_1 = V_2 A_2 = VA = \text{constant} \tag{2.32}$$

where 1 and 2 denote two consecutive locations along the tube axis.

Momentum equation

From the Navier-Stokes equations, the inviscid momentum equation, called Euler equation, can be written as:

$$\frac{\partial\overrightarrow{V}}{\partial t} + \left(\overrightarrow{V}.\overrightarrow{\nabla}\right)\overrightarrow{V} = -\frac{1}{\rho}\overrightarrow{\nabla}p + \overrightarrow{g} \tag{2.33}$$

where $\overrightarrow{V}$ is the velocity, p is the pressure and $\overrightarrow{g}$ is the acceleration of the gravity. The effects of gravity are considered to be negligible.
The second term on the left-hand side can be expressed as:

$$\left(\overrightarrow{V}.\overrightarrow{\nabla}\right)\overrightarrow{V} = \overrightarrow{\nabla}\left(\frac{|\overrightarrow{V}|^2}{2}\right) - \overrightarrow{V}\times(\overrightarrow{\nabla}\times\overrightarrow{V}) \tag{2.34}$$

For incompressible flow the Euler equation can be rewritten as:

$$\frac{\partial\overrightarrow{V}}{\partial t} + \overrightarrow{\nabla}\left(\frac{|\overrightarrow{V}|^2}{2} + \frac{p}{\rho}\right) = \overrightarrow{V}\times\left(\overrightarrow{\nabla}\times\overrightarrow{V}\right)\Big) \tag{2.35}$$

Equation 2.35 implies that for steady flow:

$$\overrightarrow{V}.\overrightarrow{\nabla}\left(\frac{|\overrightarrow{V}|^2}{2} + \frac{p}{\rho}\right) = 0 \tag{2.36}$$

This implies that:

$$\frac{|\overrightarrow{V}|^2}{2} + \frac{p}{\rho} = \text{constant along a streamline} \tag{2.37}$$

Since all streamlines originate from the same upstream condition the constant will be the same through the whole tube. Equation 2.37 is referred as the Bernoulli relation for incompressible flow. It states that the total energy is constant. The Bernoulli equation is valid between any two points in a steady, inviscid, incompressible flow.

2.3 Compressible flow

2.3.1 Steady, isentropic compressible flow

In the case of compressible flow the Bernoulli relation can be derived as follows: for steady, inviscid flow equation 2.33, with equation 2.34, becomes:

$$\vec{\nabla}\frac{|\vec{V}|^2}{2} + \frac{1}{\rho}\vec{\nabla}p = \vec{V} \times \left(\vec{\nabla} \times \vec{V}\right) \tag{2.38}$$

Now assuming that the flow is barotropic, i.e. $\rho = \rho(p)$, we find:

$$\vec{V}.\vec{\nabla}\left(\frac{|\vec{V}|^2}{2} + \int \frac{dp}{\rho}\right) = 0 \tag{2.39}$$

So that Bernoulli's relation is:

$$\frac{1}{2}|\vec{V}|^2 + \int \frac{dp}{\rho} = \text{constant along a streamline} \tag{2.40}$$

The condition that the flow is barotropic is satisfied in case that the flow is isentropic. That implies that shock waves may not occur, or, since the entropy production by a (normal) shock wave is $\vartheta(M-1)^3$, with M the Mach number upstream of the shock, that, as a rule of thumb weak shock waves with $M_{upstream} < 1.3$ are allowed.

Note that equation 2.40 reduces to equation 2.37 for $\rho =$ constant.
For a calorically perfect gas ($p = \rho RT$, $e = c_v T$), such as air at the conditions prevailing in the lungs, isentropic flow implies the pressure-density relation:

$$p = c\rho^{\gamma} \tag{2.41}$$

which is known as the Poisson relation. In equation 2.41 γ is the ratio of the specific heats. Substituting in equation 2.40 then gives:

$$\frac{1}{2}|\vec{V}|^2 + \frac{\gamma}{\gamma-1}\frac{p}{\rho} = \text{constant} \tag{2.42}$$

The constant can be related to the upstream condition $\vec{V} = V_0\vec{e}_x$, p_0, ρ_0, which leads to:

$$\frac{\rho}{\rho_0} = \left[1 + \frac{\gamma-1}{2}M_0^2\left(1 - \frac{|\vec{V}|^2}{|\vec{V}_0|^2}\right)\right]^{\frac{1}{\gamma-1}} \tag{2.43-a}$$

and

$$\frac{p}{p_0} = \left[1 + \frac{\gamma-1}{2}M_0^2\left(1 - \frac{|\vec{V}|^2}{|\vec{V}_0|^2}\right)\right]^{\frac{\gamma}{\gamma-1}} \tag{2.43-b}$$

with $M_0 = \frac{V_0}{a_0}$ and $a_0^2 = \gamma RT_0 = \gamma\frac{p_0}{\rho_0}$. In this way the velocity is related to the pressure and density.

Employing the continuity equation for the $1D$ flow in a tube, equation 2.31, which is valid for incompressible as well as compressible flow, one finds the following velocity-area relation for $1D$, isentropic flow:

$$\frac{V(x)}{V_0}\left[1+\frac{\gamma-1}{2}M_0^2\left(1-\frac{V^2(x)}{V_0^2}\right)\right]^{\frac{1}{\gamma-1}}=\frac{A_0}{A(x)} \tag{2.44}$$

For given $\frac{A_0}{A(x)}$ this relation can be solved easily for $V(x)$ using the Newton iteration procedure. The result is shown in figure 2.9 for $M_0 = 0.01$, 0.05 and 0.1, inflow Mach numbers that might occur in the flow in lungs.

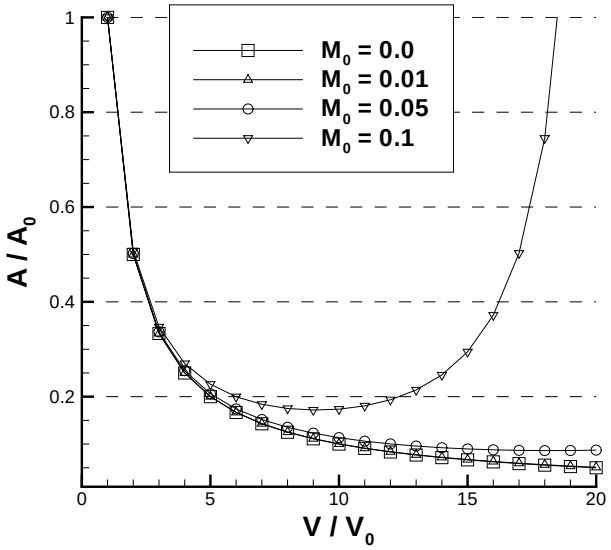

FIGURE 2.9: *The velocity / cross-sectional area relationship for isentropic compressible flow. The ratio of the specific heats is* $\gamma = 1.4$.

Note that for given inlet conditions p_0, ρ_0, V_0 the velocity is limited to:

$$\left(\frac{V(x)}{V_0}\right)_{max}=\frac{1}{M_0}\left[\frac{2}{\gamma-1}\left(1+\frac{\gamma-1}{2}M_0^2\right)\right]^{\frac{1}{2}} \tag{2.45}$$

because at that value the vacuum condition is reached. For $M_0 = 0.01$ this maximum velocity is $\frac{V(x)}{V_0} = 223.6$. For $M_0 = 0.1$ this maximum is 27.4.
Furthermore, for

$$\left(\frac{V(x)}{V_0}\right)_{sonic}=\frac{1}{M_0}\left[\frac{2}{\gamma+1}\left(1+\frac{\gamma-1}{2}M_0^2\right)\right]^{\frac{1}{2}} \tag{2.46}$$

the flow reaches the speed of sound, i.e. becomes sonic. Above this velocity the local flow is supersonic. For supersonic flow the relation between cross-sectional area $A(x)$ and flow velocity $V(x)$ switches character, i.e. for decreasing $A(x)$ the velocity decreases, while for increasing $A(x)$ the flow accelerates. The cross-sectional area associated with the sonic conditions is:

$$\left(\frac{A(x)}{A_0}\right)_{min} = \frac{M_0}{\left[\frac{2}{\gamma+1}\left(1+\frac{\gamma-1}{2}M_0^2\right)\right]^{\frac{\gamma+1}{2(\gamma-1)}}} \approx \left(\frac{\gamma+1}{2}\right)^{\frac{\gamma+1}{2(\gamma-1)}} M_0 + \vartheta(M_0^3) \qquad (2.47)$$

For $M_0 = 0.1$ the sonic velocity is reached for $\frac{V}{V_0} = 9.14$. The minimum cross-sectional area has a value of $\frac{A}{A_0} = 0.17$, see figure 2.9.
It appears from the above relation that for the small Mach numbers of relevance for the flow in lung tubes the critical cross-sectional area increases linearly with inflow Mach number as $1.2^3 M_0 \approx 1.73 M_0$, i.e. it takes less deformation before the flow chokes.

For the case of isentropic compressible flow we can couple the $1D$ fluid dynamics to the $1D$ solid dynamics, i.e. the tube law, in a similar fashion as we did for the incompressible flow using the Bernoulli relation. Employing equation 2.43-b we find:

$$\frac{p-p_{ext}}{\frac{1}{2}\rho V_0^2} = \frac{K_p}{\frac{1}{2}\rho_0 V_0^2}\left(1-\frac{1}{\alpha^{\frac{3}{2}}}\right) = \frac{p-p_0}{\frac{1}{2}\rho_0 V_0^2} - \frac{p_{ext}-p_0}{\frac{1}{2}\rho_0 V_0^2} \qquad (2.48)$$

with $\alpha = A/A_0$. It then follows with

$$\frac{p-p_0}{\frac{1}{2}\rho_0 V_0^2} = \frac{2}{\gamma M_0^2}\left(\frac{p}{p_0}-1\right) \qquad (2.49)$$

that

$$\frac{2}{\gamma M_0^2}\left[\left(1+\frac{\gamma-1}{2}M_0^2(1-v^2)\right)^{\frac{\gamma}{\gamma-1}}-1\right] = C_{p,ext} + k_p\left(1-\frac{1}{\alpha^{\frac{3}{2}}}\right) \qquad (2.50)$$

with $v = V/V_0$ and

$$C_{p,ext} = \frac{p_{ext}-p_0}{\frac{1}{2}\rho_0 V_0^2} \qquad (2.51\text{-a})$$

and

$$k_p = \frac{K_p}{\frac{1}{2}\rho_0 V_0^2} \qquad (2.51\text{-b})$$

Using the velocity / cross-sectional area relation, equation 2.44, written as:

$$\alpha v = \left[1+\frac{\gamma-1}{2}M_0^2(1-v^2)\right]^{\frac{-1}{\gamma-1}} \qquad (2.52)$$

from which, for given α, v is found, equation 2.50 yields:

$$C_{p,ext} = \frac{2}{\gamma M_0^2}\left[(\alpha v)^{-\gamma}-1\right] - k_p\left(1-\frac{1}{\alpha^{\frac{3}{2}}}\right) \qquad (2.53)$$

This results in the dimensionless transmural pressure as function of the dimensionless cross-sectional area for different values of the tube compliance and for different values of the inlet Mach number. For $M_0 = 0.0001, 0.01, 0.05$ and for 0.1 the result is given in figure 2.10. Note that these results are similar to the ones for incompressible flow: for values of k_p less

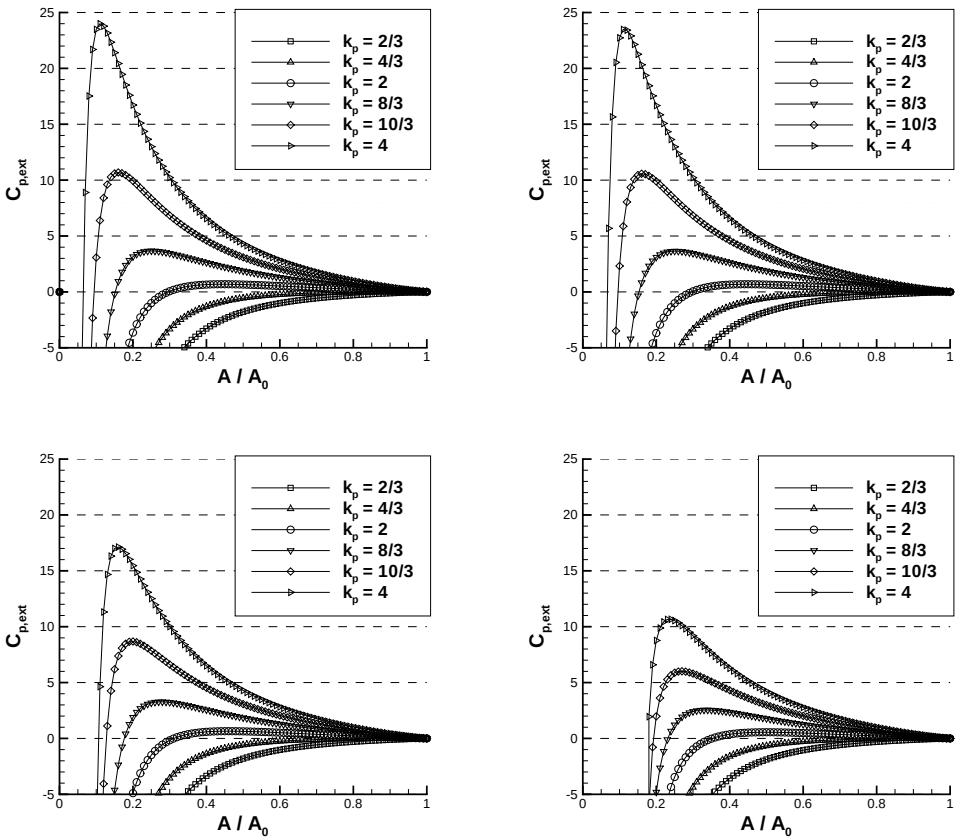

FIGURE 2.10: *Dimensionless transmural pressure as function of the dimensionless cross-sectional area for different values of the tube dimensionless stiffness.* $M_0 = 0.0001$ *(upper, left),* $M_0 = 0.01$ *(upper, right),* $M_0 = 0.05$ *(lower, left) and* $M_0 = 0.1$ *(lower, right).*

than $4/3$ the tube cannot sustain an external pressure; for values of k_p larger than $4/3$ the tube can support a transmural pressure and there are two values of A/A_0 that correspond to an equilibrium solution, a low value (large deformation) and a high value (small deformation); there is a limiting value of the dimensionless transmural pressure above which there is no solution, i.e. the tube will collapse. Shown in figure 2.10 is the solution branch for subsonic flow. There is also a branch for supersonic flow, for which the pressure is lower than for subsonic flow, that is in the region for negative $C_{p,ext}$'s not shown in the plot.

The limiting value of $C_{p,ext}$ is found by finding the maximum of $C_{p,ext}(\alpha)$, i.e. for α's that satisfy:

$$\frac{dC_{p,ext}}{d\alpha} = 0 \tag{2.54}$$

From equation 2.53 it then follows:

$$\frac{dC_{p,ext}}{d\alpha} = -\frac{2}{M_0^2}(\alpha v)^{-\gamma-1}\frac{d}{d\alpha}(\alpha v) - \frac{3}{2}k_p\frac{1}{\alpha^{\frac{5}{2}}} \tag{2.55}$$

From equation 2.52 we find:

$$\frac{d}{d\alpha}(\alpha v) = vM_0^2(\alpha v)^{\gamma}\frac{dv}{d\alpha} \tag{2.56}$$

leading to:

$$\frac{dC_{p,ext}}{d\alpha} = \frac{-2}{\alpha}\frac{dv}{d\alpha} - \frac{3}{2}k_p\frac{1}{\alpha^{\frac{5}{2}}} \tag{2.57}$$

Finally we find $\frac{dv}{d\alpha}$ from equation 2.44 as:

$$\frac{dv}{d\alpha} = \frac{-v}{\alpha - vM_0^2(\alpha v)^{2-\gamma}} \tag{2.58}$$

In the case of incompressible flow ($M_0 = 0$ and $\alpha v = 1$) we could find the value of α for which the maximum is reached, see equation 1.16 . For isentropic compressible flow an analytic solution, which depends on M_0, could not been found. The numerically found value is presented in figure 2.11. It shows that with increasing inflow Mach number the maximum possible $C_{p,ext}$ decreases rapidly. For example, for $k_p = 4$ the value of $C_{p,ext}$ is halved when the inflow Mach number increases from 0 to 0.1.
Actually, the value of k_p for which the tube cannot support any transmural pressure is found by considering $\frac{dC_{p,ext}}{d\alpha}$ at $\alpha = 1$. For $\alpha = 1$ it follows that $v = 1$, see also figure 2.9. It then immediately follows that:

$$\frac{dC_{p,ext}}{d\alpha} = \frac{2}{1 - M_0^2} - \frac{3}{2}k_p \tag{2.59}$$

If $\frac{dC_{p,ext}}{d\alpha}$ is positive for $\alpha = 1$ then a transmural pressure cannot be supported, therefore we find that:

$$k_p > \frac{4}{3(1 - M_0^2)} \tag{2.60}$$

This indicates that with increasing M_0 the minimal compliance k_p required to prevent collapse, increases.

2.3.2 Non-isentropic, inviscid flow

In case the flow in the tube is unsteady or non-isentropic we cannot reduce the momentum equation to an algebraic relation as the Bernoulli relation. In that case we have to consider the full equations. The analysis is restricted to the case the cross-section of the tube is so slowly varying that we may assume the flow to be one-dimensional.

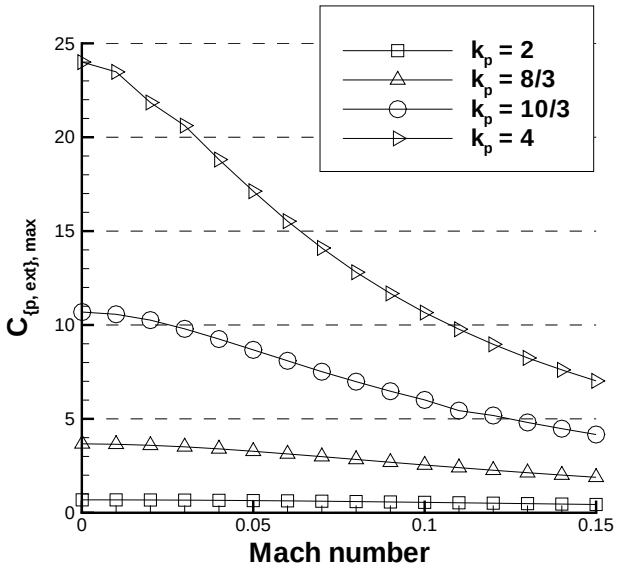

FIGURE 2.11: *Maximum value of dimensionless transmural pressure as function of the Mach number for various values of the dimensionless compliance k_p. ($\gamma = 1.4$).*

2.3.3 Euler equations for quasi 1D flow

In integral conservation form, the Euler equations are written as:

$$\frac{\partial}{\partial t}\int_V \varphi dV + \int_S \underline{F}(\varphi).\underline{n}dS = 0 \tag{2.61}$$

where φ is the column vector with conserved variables, $\underline{F}(\varphi)$ is the flux vector and V is a control volume bounded by a closed surface S and $\underline{n}$ is the outward normal to S:

$$\varphi = \begin{pmatrix} \rho \\ \rho u \\ \rho e_T \end{pmatrix} \tag{2.62}$$

and

$$\underline{F} = \begin{pmatrix} \rho u \\ \rho u^2 + p \\ (\rho e_T + p)u \end{pmatrix} = \begin{pmatrix} \rho u \\ \rho u^2 + p \\ \rho h_T u \end{pmatrix} \tag{2.63}$$

In equation 2.63 $e_T = e + 1/2u^2$ is the total energy with e the internal energy. The quantity $h_T = e_T + p/\rho$ is the total enthalpy. For a quasi-1D flow, the control volume V is bounded by three surfaces S_i, $i = 1, 2, 3$ (see figure 2.12). Replacing the first term in equation 2.61 by the time-derivative of the control-volume averaged value of $\varphi(x,t)$ in control volume V_k the Euler equations are rewritten as:

$$\frac{\partial \varphi_k}{\partial t} + \frac{1}{V_k}\sum_{i=1}^{3} \underline{F_i}(\varphi).\underline{S_i} = 0 \tag{2.64}$$

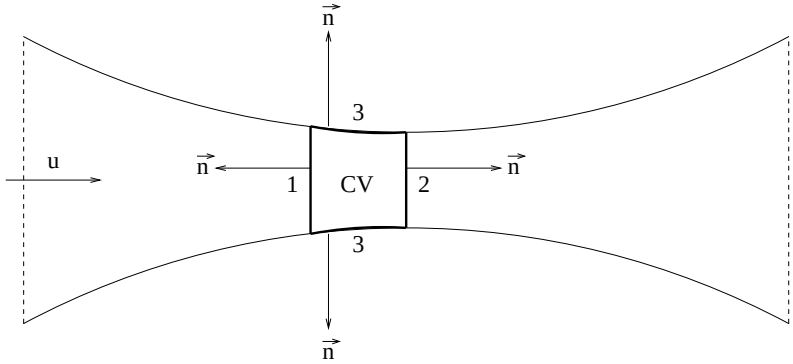

FIGURE 2.12: *Control volume (CV) in a deformed, quasi-1D tube. The control volume is bounded by the tube wall (3), the upstream cross-sectional plane (1) and the downstream cross-sectional plane (2).*

where φ_k is defined as:

$$\varphi_k(t) = \frac{1}{V_k} \int_{V_k} \varphi(\overrightarrow{x}, t) dV \tag{2.65}$$

This form is the Euler equation that corresponds to the Finite-Volume form of the equations. Equation 2.64 states that the temporal variation of the quantity φ_k associated with the control volume V_k is equal to the sum of the fluxes through the three surfaces S_i, $i = 1, 2, 3$.

The time updating used is a Jameson modified Runge-Kutta scheme. Steady-flow calculations are obtained in a non-time accurate fashion (non constant time steps in space are used to save calculation time). The flux term are calculated with a flux-splitting method, based on the Van Leer method (see [52]). The perfect gas assumption is chosen as the equation of state.

2.3.4 Flux splitting

The flux quantities need to be evaluated at the control volume boundaries. The control volume is formed by the surfaces indicated in figure 2.12. Since the solution is known only as the cell-averaged value, neither the conserved variables nor the fluxes are known at the interface boundaries. In case it is necessary to assign the cell-averaged value to a specific point within the cell, it would be assigned to the centroid of the cell. For supersonic flow, the theory of characteristics predicts that all information propagates from upstream to downstream. For subsonic flow, however, information can propagate both upstream to downstream and downstream to upstream. Thus, the flux calculation must be such that it calculates the fluxes at a given cell boundary based on cell-averaged values only from the upstream side of the boundary for supersonic flow, and from both sides of the boundary for subsonic flow. Such a flux evaluation is called an upwind scheme.
There are a large number of upwind schemes available. The Van Leer flux splitting is briefly described here, and the Advection Upstream Splitting Method (AUSM) flux splitting of Liou and Steffen ([31]), which is a modification of the Van Leer method, is presented in some more detail.

Van Leer flux splitting

Van Leer flux splitting (see [52]) is a logical approach to the problem of the flux calculation. The flux vector is analyzed in order to determine the eigenvectors of its Jacobian $\frac{dF}{d\varphi}$, which are the wave speeds of the set of Euler equations. For the quasi-1D equations, there are three speeds: $u + a$, u and $u - a$. The flux is split into respective contributions from each wave speed, with a positive, or left, flux component coming from the positive wave speeds and a negative, or right, flux component coming from the negative wave speeds. If the flow is supersonic, only flux components from the upstream direction are non-zero. For subsonic flow, both left and right flux components are non-zero.

Advection Upstream Splitting Method (AUSM)

The original authors are Liou and Steffen (see [31]). The Advection Upstream Splitting Method (AUSM) is a method similar in principle to the Van Leer flux splitting. The Liou-Steffen flux vector splitting uses Van Leer's approach to split the flux vector in two separate components. However, the flux term is now divided into two parts, the convective flux and the pressure flux, as:

$$\underline{F} = \underline{F_c} + \underline{F_p} = \begin{pmatrix} \rho u \\ \rho u^2 \\ \rho h_T u \end{pmatrix} + \begin{pmatrix} 0 \\ p \\ 0 \end{pmatrix} \tag{2.66}$$

or

$$\underline{F} = M_{1/2} \begin{pmatrix} \rho a \\ \rho u a \\ \rho h_T a \end{pmatrix} + \begin{pmatrix} 0 \\ p \\ 0 \end{pmatrix} \tag{2.67}$$

The Mach number $M_{1/2}$ is the "convective" Mach number. It can be defined as:

$$M_{1/2} = M_L^+ + M_R^- \tag{2.68}$$

The definition for the left and right Mach numbers are taken from the Van Leer method:

$$M^{\pm} = \begin{cases} \pm\frac{1}{4}(M \pm 1)^2 & \text{if } |M| \leq 1 \\ \\ \frac{1}{2}(M \pm |M|) & \text{if } |M| > 1 \end{cases} \tag{2.69}$$

This equation shows that the convective Mach number simply reduces to the sign of Mach number for a supersonic flow, while it employs Van Leer's Mach number splitting for a subsonic flow.

The pressure term is treated separately. It is defined so that communication in both directions is allowed:

$$p = p_L^+ + p_R^- \tag{2.70}$$

where p^+ and p^- are defined as:

$$p^{\pm} = \begin{cases} \pm\frac{p}{4}(M \pm 1)^2(2 \mp M) & \text{if } |M| \leq 1 \\ \\ \frac{p}{2}\frac{(M \pm |M|)}{M} & \text{if } |M| > 1 \end{cases} \tag{2.71}$$

Again, the pressure term becomes the - signed - upwind pressure for a supersonic flow. From equations 2.67, 2.68 and 2.70, the flux at any cell boundary becomes:

$$\underline{F} = (M_L^+ + M_R^-) \begin{pmatrix} \rho a \\ \rho u a \\ \rho h_T a \end{pmatrix}_{(L\ or\ R)} + \begin{pmatrix} 0 \\ p_L^+ + p_R^- \\ 0 \end{pmatrix} \tag{2.72}$$

where $L\ or\ R$ is defined as:

$$\begin{pmatrix} \rho a \\ \rho u a \\ \rho h_T a \end{pmatrix}_{(L\ or\ R)} = \begin{cases} ()_L & \text{if } M_{1/2} \geq 0 \\ ()_R & \text{if } M_{1/2} < 0 \end{cases} \tag{2.73}$$

2.3.5 Time discretisation

The time updating will be performed using a Runge Kutta scheme. Equation 2.74 outlines the scheme. The modification is that the solution at each stage is always with respect to the original n level solution. At each stage, the residual using the most current solution available is calculated as normal, and then a new stage solution is calculated by equation 2.74. At the end, the $n+1$ level solution is simply the last stage calculation. Any value of M may be used, $M = 4$ is the most common.

$$\begin{gathered} \varphi^0 = \varphi^n \\ \varphi^k = \varphi^0 - \tfrac{\Delta t}{M-k+1} F^{k-1} \quad k = 1 \ldots M \\ \varphi^{n+1} = \varphi^n \end{gathered} \tag{2.74}$$

Non constant time steps are used. The time step is calculated for each control volume, so that a wave is not allowed to travel more than one half of a control volume during one time step.

2.3.6 Unsteady flow calculations

The Euler solver as described so far uses non-constant time steps in space, i.e. is not time-accurate. This choice allows to choose large time steps in the regions where the changes of the flow solution are small in order to reduce calculation time. However, the need of unsteady flow calculations dictates a time-accurate solution. That implicates a constant time step, which will be small. For the calculation the non-constant time steps are computed and the smallest one will be chosen, ensuring accuracy of the calculations at any point of the flow domain.
Having a time-accurate solver, unsteady flow calculations can be performed. This will be achieved in two steps. First a steady flow solution is calculated, specifying boundary conditions at time t=0, which is the initial solution. Then the unsteady flow calculation is performed, starting from this initial solution, and applying unsteady boundary conditions at each time t.

2.3.7 Boundary conditions

Characteristics of the system
The Euler equations (2.64) can be expressed in a non-conservative form as:

$$\frac{\partial U}{\partial t} + A(U)\frac{\partial U}{\partial x} = 0 \tag{2.75}$$

with U the column vector containing the primitive flow variables, i.e.:

$$U = \begin{pmatrix} \rho \\ u \\ p \end{pmatrix} \tag{2.76}$$

A is the Jacobian matrix, which can be found to be:

$$A = \begin{pmatrix} u & \rho & 0 \\ 0 & u & \frac{1}{\rho} \\ 0 & \rho a^2 & u \end{pmatrix} \tag{2.77}$$

where a is the speed of sound, defined as the partial derivative of the pressure with respect to the density at constant entropy, i.e.:

$$a^2 = \left(\frac{\partial p}{\partial \rho}\right)_s \tag{2.78}$$

The eigenvalues λ of the matrix A are the solution of:

$$|A - \lambda I| = 0 \tag{2.79}$$

where I is the identity matrix.
We find:

$$\begin{aligned} \lambda_1 &= u \\ \lambda_2 &= u + a \\ \lambda_3 &= u - a \end{aligned} \tag{2.80}$$

These three eigenvalues are real, so that the system is hyperbolic in (x, t), irrespective of the local Mach number, i.e. both for subsonic and for supersonic flow. One characteristic direction corresponds to the streamline direction and the remaining two directions correspond the directions of acoustic wave propagation.
The propagation properties in a one-dimensional flow are expressed in a straightforward way by the characteristic variables, which are described by the compatibility relations for one-dimensional flow. The compatibility relations are found by multiplying equation 2.75 with the left eigenvectors related to the eigenvalues $\lambda_1, \lambda_2, \lambda_3$. This results in:

$$\begin{aligned} &\tfrac{\partial \rho}{\partial t} - \tfrac{1}{a^2}\tfrac{\partial p}{\partial t} + u\left(\tfrac{\partial \rho}{\partial x} - \tfrac{1}{a^2}\tfrac{\partial p}{\partial x}\right) = 0 && \text{along } \tfrac{dx}{dt} = u \\ &\tfrac{\partial u}{\partial t} + \tfrac{1}{\rho a}\tfrac{\partial p}{\partial t} + (u + a)\left(\tfrac{\partial u}{\partial x} + \tfrac{1}{\rho a}\tfrac{\partial p}{\partial x}\right) = 0 && \text{along } \tfrac{dx}{dt} = u + a \\ &\tfrac{\partial u}{\partial t} - \tfrac{1}{\rho a}\tfrac{\partial p}{\partial t} + (u - a)\left(\tfrac{\partial u}{\partial x} - \tfrac{1}{\rho a}\tfrac{\partial p}{\partial x}\right) = 0 && \text{along } \tfrac{dx}{dt} = u - a \end{aligned} \tag{2.81}$$

The first compatibility relation can be expressed as:

$$\frac{p}{\rho^\gamma} = \text{constant along } \tfrac{dx}{dt} = u \tag{2.82}$$

which implies that the entropy is constant along the streamlines, with a jump to a higher value as the streamline passes through a shock wave. The other two compatibility relations can be

written as:

$$\begin{aligned} \frac{\partial}{\partial t}\left(u \pm \frac{2a}{\gamma-1}\right) \quad &\mp \quad \frac{\rho^{\gamma-1}}{(\gamma-1)a}\frac{\partial}{\partial t}(\frac{p}{\rho^{\gamma}}) \\ &+ \quad (u \pm a)\left[\frac{\partial}{\partial x}\left(u \pm \frac{2a}{\gamma-1}\right) \mp \frac{\rho^{\gamma-1}}{(\gamma-1)a}\frac{\partial}{\partial x}\frac{p}{\rho^{\gamma}}\right] = 0 \\ &\quad \text{along } \tfrac{dx}{dt} = u \pm a \end{aligned} \tag{2.83-a}$$

For isentropic flow the two Riemann invariants follow as:

$$u \pm \tfrac{2a}{\gamma-1} = \text{constant} \quad \text{along } \tfrac{dx}{dt} = u \pm a \tag{2.84}$$

The boundary conditions may be divided into numerical and physical boundary conditions. The number of physical boundary conditions which may be specified depends on whether the flow is subsonic or supersonic at the boundary considered.

Subsonic inflow
At a subsonic inlet, there are two inward-running characteristics, the ones associated with $\lambda_1 = u$ and $\lambda_2 = u + a$ and one outward-running, the one associated with $\lambda_3 = u - a$. We can thus prescribe only two physical conditions, leaving one numerical condition. This numerical condition is determined by the third of the compatibility relations, equation 2.81-c, which describes the upstream traveling acoustic wave. In the numerical method, two different physical boundary conditions are implemented. The first one prescribes the *total* pressure p_{tot} and *total* temperature T_{tot}, the second one prescribes the *static* pressure p and *static* temperature T.

Supersonic inflow
For a supersonic inflow, all the characteristics are inward-running, and we are free to specify all flow variables.

Subsonic outflow
At a subsonic outflow boundary, there is one inward-running characteristic, the one associated with $\lambda_3 = u - a$ and two outward-running characteristics the ones associated with $\lambda_1 = u$ and $\lambda_2 = u + a$. Therefore only one physical condition may be prescribed. In the numerical method, the static pressure is prescribed, and the remaining variables ρ and u are determined using the compatibility relations 2.81-a and 2.81-b.

Supersonic outflow
For a supersonic outflow, all characteristics are outward-running. Thus, no physical conditions may be prescribed.

2.3.8 Results

During forced expiration the velocity in the human lung will start from zero but will increase to possibly transonic speed at the throat of the elastic tubes. Thereby three different flow regimes may be encountered (incompressible flow, subsonic compressible flow and transonic flow). These three regimes will be treated here with the S2-nozzle as an example.

The method presented was developed by Put ([43]). It has been validated for the NACA 0012 airfoil and for the parallel-jet emanating from the A1-nozzle in particular. The method solves the Euler equations on both a structured and unstructured mesh, using the Finite Volume Method described for the $1D$ case. The flux term $\underline{F}$ are calculated using Liou's AUSM$^+$ FVS scheme. As an example, calculations for the flow in a quasi- one-dimensional nozzle are presented next.

S2-nozzle

The nozzle used is the two-dimensional S2-nozzle ([1]), symmetric with respect to $y = 0$ plane, symmetric with respect to x-axis, to which a straight inlet and outlet section have been added. This nozzle is chosen as test-case because it resembles a lung tube that is partially collapsed. Its geometry is presented in figure 2.13 (bottom). For each x-position, the half height $h/2$ of the nozzle is given. Its length is $L = 0.275\ m$, and its height is $h = 0.063\ m$ at the inlet and outlet. The height at the throat ($x = 0$) is $h^* = 0.03\ m$. The converging - diverging part is defined as a circular arc of radius $R = 0.4\ m$, which center is located at ($x = 0, y = h^* + R$). The geometry can be resumed as:

$$\begin{array}{lll} x \in (-0.15, -0.1137) & h = 0.063 \\ x \in (-0.1137, 0.1137) & h = 2\left[\left(\frac{h^*}{2} + R\right) - \sqrt{R^2 - x^2}\right] \\ x \in (0.1137, 0.15) & h = 0.063 \end{array} \tag{2.85}$$

The mesh used for the calculations presented consists of 240, one-dimensional cells. The ratio between the area at the inlet A_0 and the area at the throat A^* is $\frac{A_0}{A^*} = 2.1$ ($\alpha = 0.476$). All dimensions are expressed in m.

Incompressible flow

$u_0 = 10\ m/s$

The total conditions at the inlet are prescribed, using the static density, the velocity and the static pressure: $\rho_0 = 1\ kg/m^3$, $u_0 = 10\ m/s$ and $p_0 = 101000\ Pa$, respectively. The static pressure: $p_0 = 101000\ Pa$ is prescribed at the outlet. From these quantities it follows that the speed of sound is $a_0 = \sqrt{\gamma p_0/\rho_0} = 376.03\ m/s$, so that the inflow Mach number is $M_0 = 0.027$. Therefore, the total conditions are:

$$\begin{array}{ll} p_{tot} = p_0\left[1 + \frac{\gamma-1}{2}M_0^2\right]^{\frac{\gamma}{\gamma-1}} & = 101050.0\ N/m^2 \\ \rho_{tot} = \rho_0\left[1 + \frac{\gamma-1}{2}M_0^2\right]^{\frac{1}{\gamma-1}} & = 1.00035\ kg/m^3 \end{array}$$

so that it follows from the gas law for a perfect gas that:

$$T_{tot} = \frac{p_0}{R\rho_0} = 351.967\ K$$

with $R = 287\ J/(kgK)$.
The result of this calculation is shown in figure 2.13. Acceleration of the flow occurs in the

converging part of the nozzle. After a maximum velocity at the throat of $u/u_0 = 2.10$, the outlet velocity becomes the same as the inlet velocity since outlet and inlet cross-sectional areas are equal.

For air, as in the present case, it is considered that a change of 5% in density is a lower limit of notable compressibility effects. Below this limit, changes in density caused by changes in velocity have no substantial effects on the flow field. In our case, we observe a maximum change in density of about 0.12%, located at the throat of the nozzle ($x = 0\ m$). Thus the compressibility effects can be neglected.
Furthermore, the flow is also considered incompressible when the free-stream Mach number ($M_0 = u_0/a_0$) is smaller than 0.3. For the present inlet Mach number of 0.027 the Mach number is everywhere in the nozzle smaller than 0.055, i.e. very small.

In the pressure and density distribution small wiggles can be observed at the inlet and outlet of the converging and diverging part of the nozzle, i.e. $x = \pm 1.1\ m$, respectively. Also at the throat wiggles are apparent. Calculations conducted for lower inlet Mach numbers showed that these wiggles increase with decreasing inlet velocities. The present numerical method for compressible flow may require a preconditioner if calculations at low speed are to be considered.

Residuals
The L_2-norm of the residuals of the density is shown on figure 2.17. The L_2-norm is defined as:

$$L_2(\rho) = \sqrt{\frac{1}{N}\sum_{i=1}^{N}\left(\frac{\rho_i^{n+1} - \rho_i^n}{\Delta t_i}\right)^2} \tag{2.86}$$

with N the number of cells, the superscript n the iteration number and Δt_i the local time step.
When the L_2-norm becomes smaller than 10^{-6}, the calculation is considered converged. Figure 2.17 shows that the method converges, though very slowly and with large variation in the residual.

Comparison with incompressible flow and isentropic compressible flow results

Figure 2.15 shows a comparison of the results of the Euler method with results for incompressible flow and results of isentropic compressible. The results of the Euler method agree very well with the results of the isentropic compressible flow. The comparison shows that at the inlet Mach number of 0.027 the incompressible flow solution gives a 0.25% lower value of $u(x)/u_0$ at most. The difference in pressure coefficient is about 0.862% at most, with the compressible flow solution giving the lower value, i.e. a higher transmural pressure. This implies that compressible flow results lead to collapse earlier than incompressible flow results as we have seen before.

$u_0 = 50\ m/s$

Calculations have also been conducted using the static density, the velocity and the static

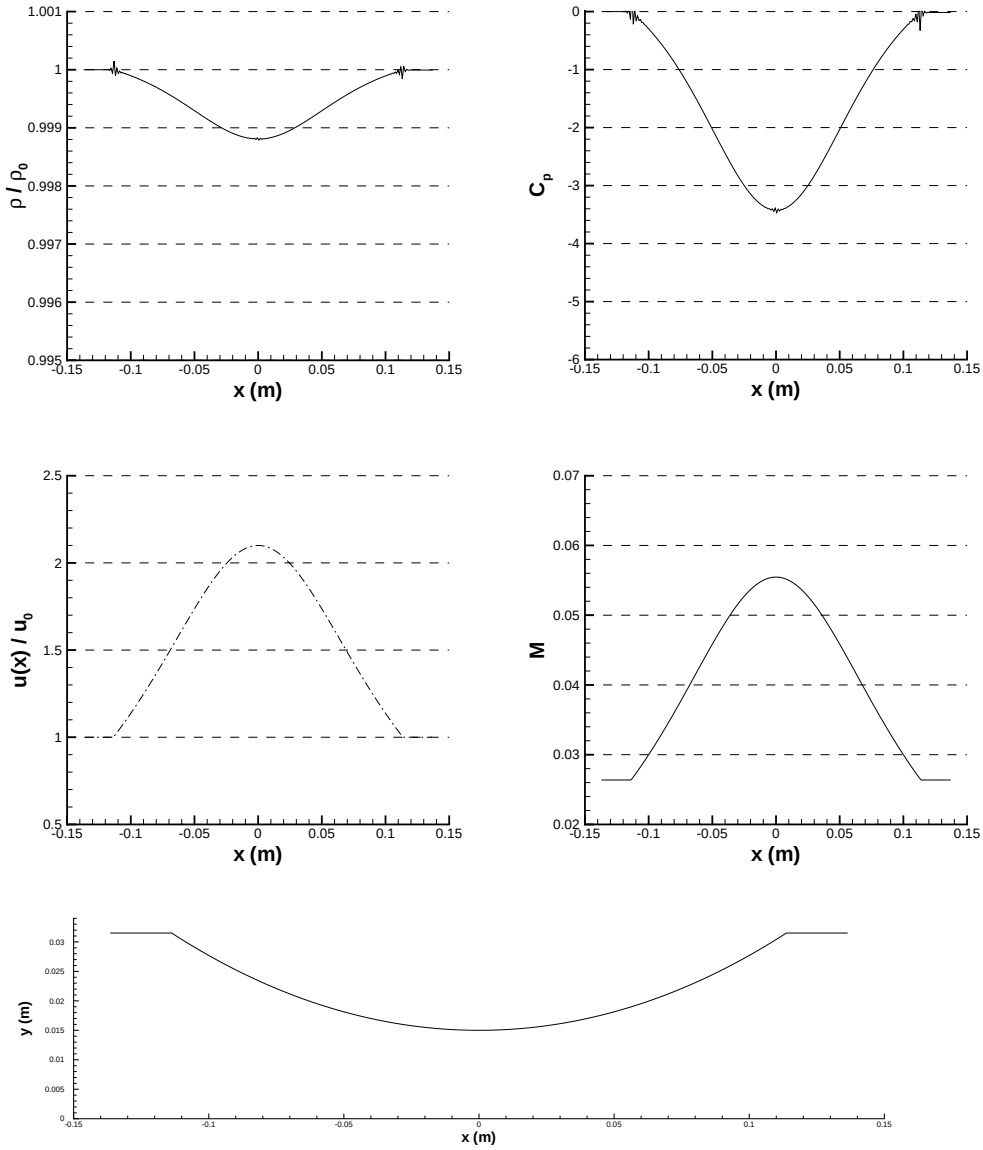

FIGURE 2.13: *Numerical solution of the quasi-*$1D$ *Euler equations for* 240 *cells. Dimensionless density, pressure, velocity and Mach number profiles of the flow in the S2-nozzle (below).* $u_0 = 10\ m/s$, $p_0 = 101000\ N/m^2$, $\rho_0 = 1\ kg/m^3$. *The height* h *of the nozzle and the x-position are expressed in* $[m]$*). The flow may be considered incompressible everywhere in the nozzle.*

pressure as: $\rho_0 = 1\ kg/m^3$, $u_0 = 50\ m/s$ and $p_0 = 101000\ Pa$, respectively. The static pressure: $p_0 = 101000\ Pa$ is prescribed at the outlet. From these quantities it follows that

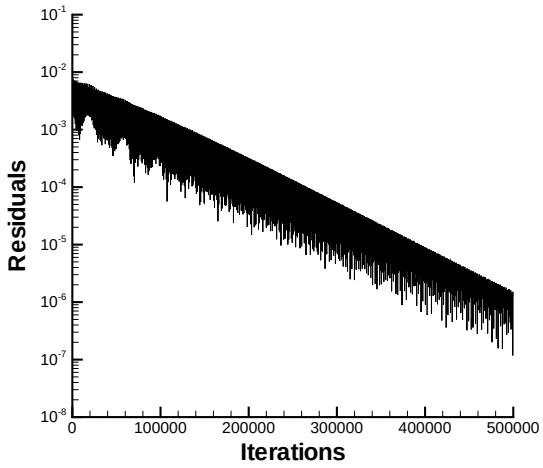

FIGURE 2.14: *L_2-norm of the residuals of ρ, for the case: $u_0 = 10\ m/s$, $p_0 = 101000\ N/m^2$, $\rho_0 = 1\ kg/m^3$, $n = 240$ cells.*

the speed of sound is $a_0 = \sqrt{\gamma p_0/\rho_0} = 376.03\ m/s$, so that the inflow Mach number is $M_0 = 0.133$. Therefore, the total conditions are:

$$\begin{aligned} p_{tot} &= p_0 \left[1 + \tfrac{\gamma-1}{2} M_0^2\right]^{\frac{\gamma}{\gamma-1}} &= 102255.5\ N/m^2 \\ \rho_{tot} &= \rho_0 \left[1 + \tfrac{\gamma-1}{2} M_0^2\right]^{\frac{1}{\gamma-1}} &= 1.008864\ kg/m^3 \end{aligned}$$

so that it follows from the gas law for a perfect gas that:

$$T_{tot} = \frac{p_0}{R\rho_0} = 353.161\ K$$

The result of this calculation is shown in figure 2.16. Acceleration of the flow occurs in the converging part of the nozzle. After a maximum velocity at the throat of $u/u_0 = 2.17$, the outlet velocity becomes the same as the inlet velocity since outlet and inlet cross-sectional areas are equal.

The maximum change in density is slightly above 3%, located at the throat of the nozzle ($x = 0\ m$). Thus also for $u_0 = 50\ m/s$ the compressibility effects can be neglected.
For the present inlet Mach number of 0.133, much smaller than 0.3, the flow in the nozzle can be considered incompressible.

The wiggles in the pressure and density distribution have almost disappeared. The residuals for the calculation are presented in figure 2.17. The numerical method converges now more than three times as fast.

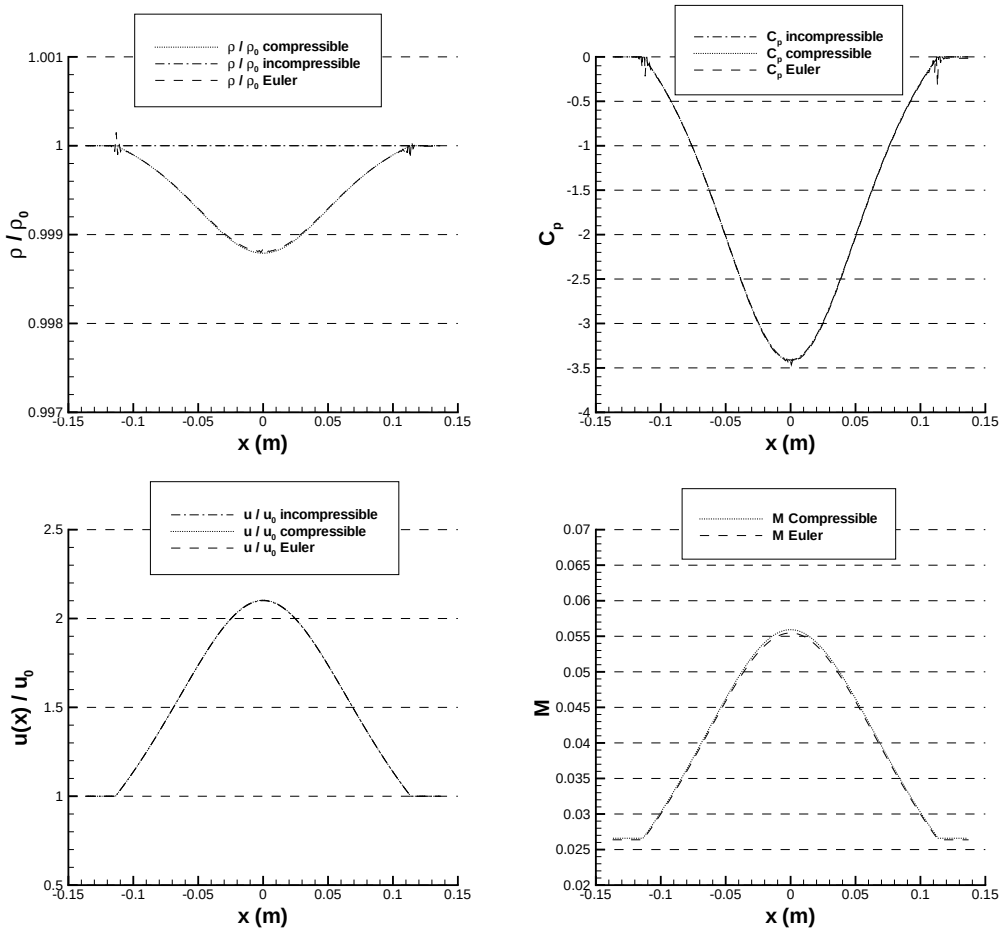

FIGURE 2.15: *Comparison of the numerical solution of the Euler equations with incompressible flow and isentropic compressible flow results.* $u_0 = 10\ m/s$, $p_0 = 101000\ N/m^2$, $\rho_0 = 1\ kg/m^3$.

Comparison with incompressible flow and isentropic compressible flow results

Figure 2.18 shows a comparison of the results of the Euler method with results for incompressible flow and results for isentropic compressible flow. Again, the results of the Euler method agree very well with the results of the isentropic compressible flow relations. The comparison shows that for the inlet Mach number of 0.133 the incompressible flow solution gives a 3% lower value of $u(x)/u_0$ at most. The difference in pressure coefficient is about 6.6% at most, with the compressible flow solution giving the lower value, i.e. a higher transmural pressure.

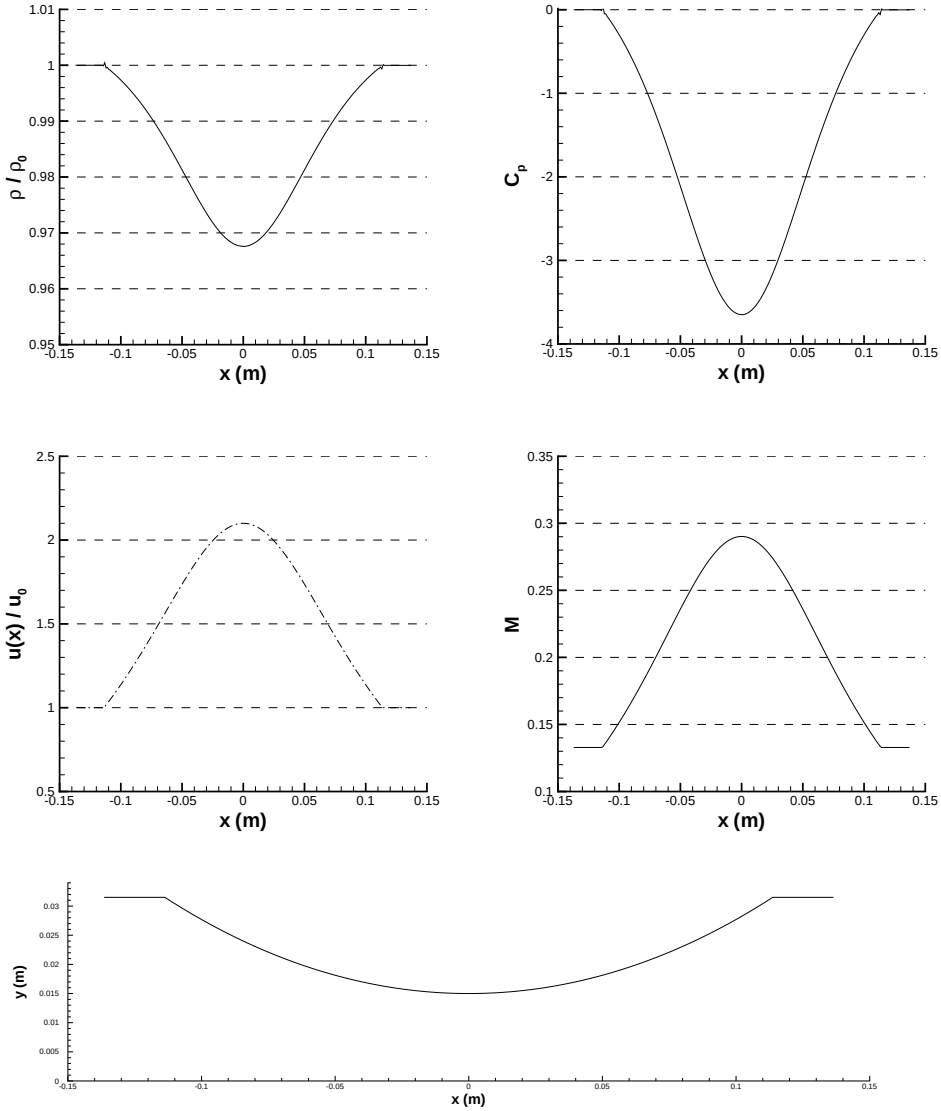

FIGURE 2.16: *Numerical solution of the quasi-*$1D$ *Euler equations for* 240 *cells. Dimensionless density, pressure, velocity and Mach number profiles of the flow in the S2-nozzle (below).* $u_0 = 50\ m/s$, $p_0 = 101000\ N/m^2$, $\rho_0 = 1\ kg/m^3$. *The height* h *of the nozzle and the x-position are expressed in* $[m]$*). The flow may be considered incompressible everywhere in the nozzle.*

Compressible, subsonic flow

In this example the inlet velocity is doubled to $100\ m/s$. The nozzle is unchanged, inlet density and static pressure, outlet static pressure are unchanged. For this case the inlet Mach

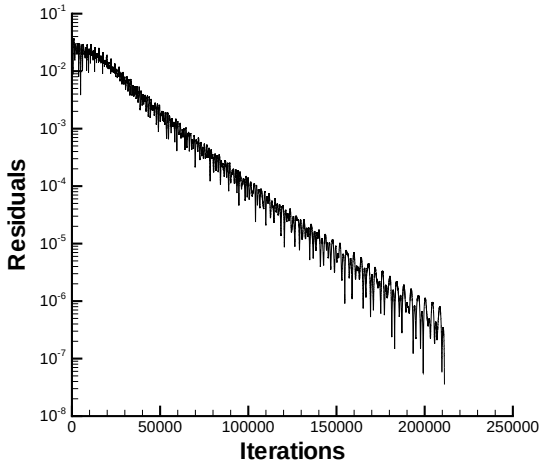

FIGURE 2.17: *L_2-norm of the residuals of ρ, for the case: $u_0 = 50\ m/s$, $p_0 = 101000\ N/m^2$, $\rho_0 = 1\ kg/m^3$, $n = 240$ cells.*

number is now 0.2659 and the total conditions are: $p_{tot} = 106089\ N/m^2$, $\rho_{tot} = 1.03574\ kg/m^3$ and $T_{tot} = 356.894\ K$. Results are shown in figure 2.19.
In the nozzle the inlet Mach number increases rapidly from the inlet value of 0.266 to a maximum of 0.72 in the throat so that the flow must be considered compressible. However, the flow remains subsonic and downstream of the throat the Mach number decreases again. The maximum velocity now is $u/u_0 = 2.594$, substantially higher than for $u_0 = 50\ m/s$. This is due to the lower value of the density that necessitates a higher velocity in order to preserve the mass flow. The density decreases to a value around 20% below the inlet value, also demonstrating that the flow is really compressible. The pressure at the throat is lower than for $u_0 = 50\ m/s$, now the maximum C_p is around -5.2.

The residuals for the calculation are presented in figure 2.20. The rate of convergence is very similar to the one we saw for $u_0 = 50\ m/s$.

Comparison with incompressible flow and isentropic compressible flow results

The results of the incompressible flow, the isentropic compressible flow and the ones calculated with the Euler compressible flow method are presented in figure 2.21 Again, the results of the Euler method agree with the ones obtained for isentropic compressible flow. The incompressible flow solution gives a 20% lower value of $u(x)/u_0$ at the throat than the compressible flow solutions. The difference in pressure coefficient is about 34%.

Critical value of the Mach number

Using the formulation of isentropic compressible flow it is possible to find the inlet Mach number for which the nozzle will choke, i.e. reach the speed of sound in the throat. It is not

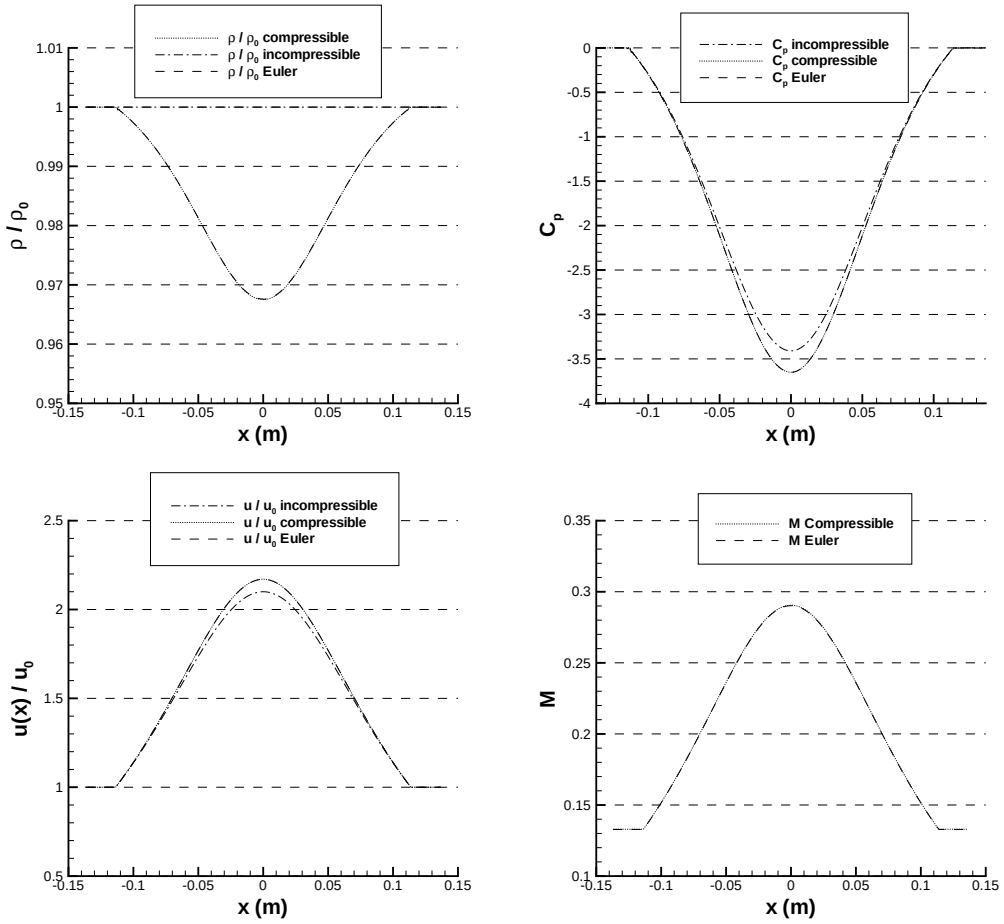

FIGURE 2.18: *Comparison of numerical solution of Euler equations with incompressible flow and isentropic compressible flow results.* $u_0 = 50\,m/s$, $p_0 = 101000\,N/m^2$, $\rho_0 = 1\,kg/m^3$.

possible to increase M_0 to values exceeding this critical value.

The mass-flow through the nozzle is constant. At the inlet the mass-flow is $\dot{m}_0 = \rho_0 u_0 A_0$. At the sonic throat the mass-flow will be:

$$\dot{m}^* = \rho^* u^* A^* = \rho^* a^* A^* = \rho^* \sqrt{\gamma R T^*} A^* \tag{2.87}$$

In the nozzle the flow is isentropic, so that the total pressure and total temperature are constant, i.e.:

$$p_{tot} = p_0 \left[1 + \frac{\gamma - 1}{2} M_0^2\right]^{\frac{\gamma}{\gamma-1}} = p^* \left[\frac{\gamma + 1}{2}\right]^{\frac{\gamma}{\gamma-1}} \tag{2.88-a}$$

$$T_{tot} = T_0 \left[1 + \frac{\gamma - 1}{2} M_0^2\right] = T^* \left[\frac{\gamma + 1}{2}\right] \tag{2.88-b}$$

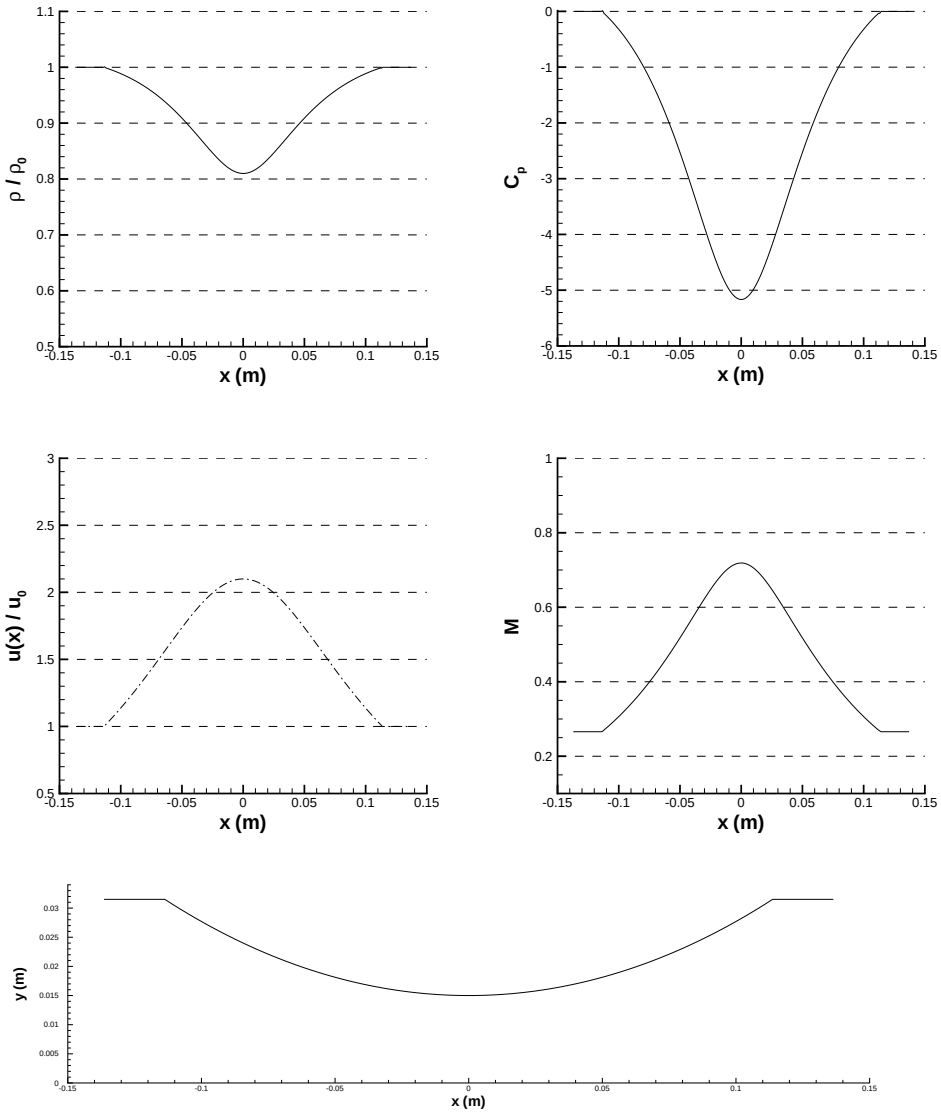

FIGURE 2.19: *Numerical solution of the quasi-*$1D$ *Euler equations for* 240 *cells. Density, pressure, velocity and Mach number profiles of the flow in the S2-nozzle (below).* $u_0 = 100$ m/s, $p_0 = 101000$ N/m^2, $\rho_0 = 1$ kg/m^3. *The flow is compressible everywhere in the nozzle.*

$$\rho_{tot} \quad = \quad \rho_0 \left[1 + \frac{\gamma - 1}{2} M_0^2\right]^{\frac{1}{\gamma - 1}} = \rho^* \left[\frac{\gamma + 1}{2}\right]^{\frac{1}{\gamma - 1}} \tag{2.88-c}$$

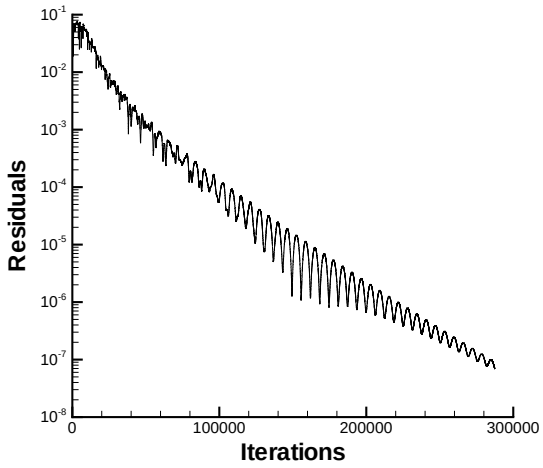

FIGURE 2.20: *L_2-norm of the residuals of ρ, for the case: $u_0 = 100\ m/s$, $p_0 = 101000\ N/m^2$, $\rho_0 = 1\ kg/m^3$, $n = 240$ cells.*

Here the quantities with superscript $*$ describe the value of the quantities for a local Mach number of 1.0, i.e. they represent the sonic values.
It follows:

$$\begin{aligned} \dot{m}^* &= \rho_0 \sqrt{\gamma R T_0} A_0 \frac{\rho^*}{\rho_0} \left(\frac{T^*}{T_0}\right)^{\frac{1}{2}} \frac{A^*}{A_0} \\ &= \rho_0 V_0 A_0 \frac{A^*}{A_0} \frac{1}{M_0} \left[\frac{2}{\gamma+1}\left(1 + \frac{\gamma-1}{2} M_0^2\right)\right]^{\frac{\gamma+1}{2(\gamma-1)}} \end{aligned} \tag{2.89}$$

So, as long as $m^*/m_0 \geq 1$ the flow will be realizable, i.e.

$$\frac{m^*}{m_0} = \frac{A^*}{A_0} \frac{1}{M_0} \left[\frac{2}{\gamma+1}\left(1 + \frac{\gamma-1}{2} M_0^2\right)\right]^{\frac{\gamma+1}{2(\gamma-1)}} \geq 1 \tag{2.90}$$

For the S2-nozzle $A_0/A^* = 2.1$ and it follows that $M_{0,max} = 0.28968$ is the maximum inlet Mach number, which is only slightly above the Mach number of the final example.

2.4 Conclusion

For the flow conditions considered, as a reasonable first approximation, in the lung tubes the flow may be considered using the isentropic compressible flow relations. Furthermore, for not too extreme conditions it suffices to use the incompressible flow relations.

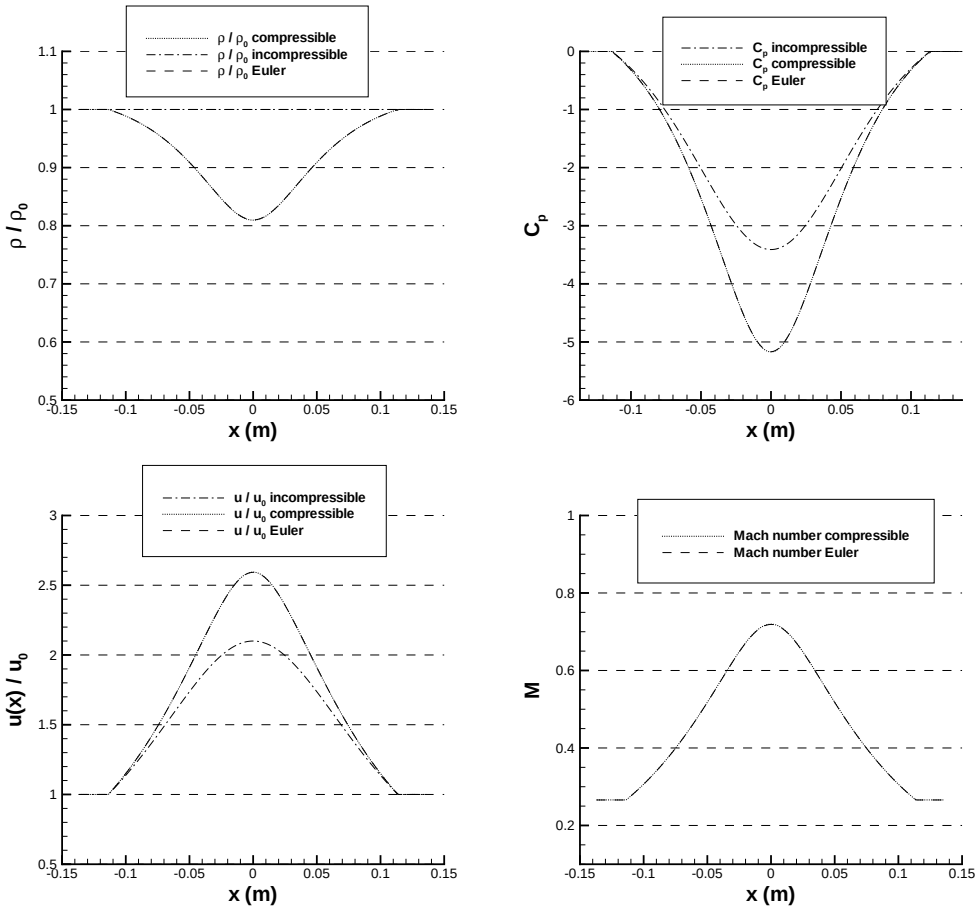

FIGURE 2.21: *Comparison of solution of Euler equations for compressible flow with incompressible flow and isentropic compressible flow results.* $u_0 = 100\,m/s$, $p_0 = 101000\,N/m^2$, $\rho_0 = 1\,kg/m^3$.

STRUCTURAL MODELING

CHAPTER 3

In this chapter, a model for the deformation of an elastic tube is presented. A general introduction to the finite-element method (FEM) is given. Then, the numerical implementation of the model for a structural deformation is detailed. Finally, as a validation of this method, various test-cases are investigated.

3.1 Objectives

In this section, the deformation of a three-dimensional hollow tube due to an external load is investigated. The flow inside this tube will lead to a different pressure inside the tube compared to the pressure in the region external to the tube and therefore a distributed load will be present on the tube wall. The external pressure is kept constant, while in general the internal pressure will vary according to the flow velocity. During expiration, the pressure inside the tube will be lower than the external pressure, i.e. the tube will collapse.
The deformation of the tube wall is computed using a finite-element method (FEM). The tube wall is discretized into elements, which form a mesh. In each element, a finite number of points is chosen, the so-called "nodal points", or "nodes". The displacement of each nodal point, as a consequence of the loads applied on all elements, will represent the deformation of the tube wall.

3.2 Structural model

The model presented here will allow small as well as large deformations, governed by a linear and a non-linear partial differential equation, respectively. The linear formulation provides a direct prediction of the (small) deformation, while the non-linear formulation is based on a non-linear form of the strain to refine the solution.

A body subject to an external load will deform. An equilibrium is reached when the internal forces compensate the external forces:

$$\overrightarrow{\nabla}.\overline{\overline{\sigma}} = \overrightarrow{f}_{ext}\,\delta(\overrightarrow{x} - \overrightarrow{x}_{force}) \tag{3.1}$$

$\overline{\overline{\sigma}}$ is the stress tensor, $\overrightarrow{f}_{ext}$ is the vector of the external load and $\delta(\overrightarrow{x} - \overrightarrow{x}_{force})$ is the Dirac delta function with argument $\overrightarrow{x} - \overrightarrow{x}_{force}$, where $\overrightarrow{x}_{force}$ is the location of the external force.

The $3 * 3$ stress tensor is symmetric, i.e.:

$$[\overline{\overline{\sigma}}] = \begin{bmatrix} \sigma_{xx} & \sigma_{xy} & \sigma_{xz} \\ \sigma_{yx} & \sigma_{yy} & \sigma_{yz} \\ \sigma_{zx} & \sigma_{zy} & \sigma_{zz} \end{bmatrix} \tag{3.2}$$

The diagonal elements of $\overline{\overline{\sigma}}$ are the normal stress components, while the off-diagonal elements of $\overline{\overline{\sigma}}$ are the shear stress components. The elements of the stress tensor are a function of the strain. The $3 * 3$ strain tensor is also symmetric, i.e.:

$$[\overline{\overline{\epsilon}}] = \begin{bmatrix} \epsilon_{xx} & \epsilon_{xy} & \epsilon_{xz} \\ \epsilon_{yx} & \epsilon_{yy} & \epsilon_{yz} \\ \epsilon_{zx} & \epsilon_{zy} & \epsilon_{zz} \end{bmatrix} \tag{3.3}$$

The diagonal elements of the strain are related to the extension of an infinitesimal element along the coordinate directions, while the off-diagonal terms are related with the deformation of the infinitesimal element from a cube into a parallelepiped.
Because $\overline{\overline{\sigma}}$ and $\overline{\overline{\epsilon}}$ are symmetric, we write the 6 independent elements in a $6 * 1$ column vector as:

$$\{\sigma\} = \{\sigma_{xx}, \sigma_{yy}, \sigma_{zz}, \sigma_{xy}, \sigma_{yz}, \sigma_{xz}\}^T \tag{3.4-a}$$

$$\{\epsilon\} = \{\epsilon_{xx}, \epsilon_{yy}, \epsilon_{zz}, 2\epsilon_{xy}, 2\epsilon_{yz}, 2\epsilon_{xz}\}^T \tag{3.4-b}$$

The stress can be expressed in terms of the strain as:

$$\{\sigma\} = [D]\{\epsilon\} \tag{3.5}$$

where the $6 * 6$ matrix $[D]$ represents the elasticity of the material, which we assume constant. $[D]$ is a function of the Young modulus E and of the Poisson ratio ν. The elasticity matrix is written as:

$$[D] = \frac{E(1-\nu)}{(1+\nu)(1-2\nu)} \cdot \begin{bmatrix} 1 & \frac{\nu}{1-\nu} & \frac{\nu}{1-\nu} & 0 & 0 & 0 \\ \frac{\nu}{1-\nu} & 1 & \frac{\nu}{1-\nu} & 0 & 0 & 0 \\ \frac{\nu}{1-\nu} & \frac{\nu}{1-\nu} & 1 & 0 & 0 & 0 \\ 0 & 0 & 0 & \frac{(1-2\nu)}{2(1-\nu)} & 0 & 0 \\ 0 & 0 & 0 & 0 & \frac{(1-2\nu)}{2(1-\nu)} & 0 \\ 0 & 0 & 0 & 0 & 0 & \frac{(1-2\nu)}{2(1-\nu)} \end{bmatrix} \tag{3.6}$$

The final step is to relate the strain ϵ to the displacement vector $\{u\} = \{u, v, w\}^T$, which represents the displacement of an infinitesimal element due to the stress.
In case the displacements are small the elements of the tensor $\overline{\overline{\epsilon}}$ are:

$$\epsilon_{ij} = \frac{1}{2}\left(\frac{\partial u_i}{\partial x_j} + \frac{\partial u_j}{\partial x_i}\right) \tag{3.7}$$

with $x_1 = x$, $x_2 = y$ and $x_3 = z$, while $u_1 = u$, $u_2 = v$ and $u_3 = w$, which in terms of the column vector $\{\epsilon\}$ can be expressed as:

$$\{\epsilon\} = \{B(u)\} = [B_L]\{u\} \tag{3.8}$$

with $[B_L]$ the $6 * 3$ matrix with partial derivatives:

$$[B_L] = \begin{bmatrix} \frac{\partial}{\partial x} & 0 & 0 \\ 0 & \frac{\partial}{\partial y} & 0 \\ 0 & 0 & \frac{\partial}{\partial z} \\ \frac{\partial}{\partial y} & \frac{\partial}{\partial x} & 0 \\ 0 & \frac{\partial}{\partial z} & \frac{\partial}{\partial y} \\ \frac{\partial}{\partial z} & 0 & \frac{\partial}{\partial x} \end{bmatrix} \tag{3.9}$$

In the non-linear case we have:

$$\{\epsilon\} = [B_L]\{u\} + [B_{NL}(u)]\{u\} \tag{3.10}$$

where $B_{NL}(u)$ is the $6 * 3$ matrix defined as:

$$\{\epsilon_{NL}\} = \frac{1}{2} \begin{bmatrix} \theta_x^T & 0 & 0 \\ 0 & \theta_y^T & 0 \\ 0 & 0 & \theta_z^T \\ 0 & \theta_z^T & \theta_y^T \\ \theta_z^T & 0 & \theta_x^T \\ \theta_y^T & \theta_x^T & 0 \end{bmatrix} \begin{Bmatrix} \theta_x \\ \theta_y \\ \theta_z \end{Bmatrix} = [B_{NL}(u)]\{u\} \tag{3.11}$$

in which:

$$\{\theta_.\} = \left\{ \frac{\partial u}{\partial .}, \frac{\partial v}{\partial .}, \frac{\partial w}{\partial .}, \right\}^T, etc \tag{3.12}$$

So in summary we have the following system of partial differential equations for the displacements $\{u\} = \{u, v, w\}^T$:

$$\overrightarrow{\nabla} . \overline{\overline{\sigma}} = \overrightarrow{f}_{ext}\, \delta(\overrightarrow{x} - \overrightarrow{x}_{force}) \tag{3.13}$$

with the elements of $\overline{\overline{\sigma}}$ contained in $\{\sigma\}$, and:

$$\{\sigma\} = [D]\{\epsilon\} \tag{3.14}$$

with:

$$\{\epsilon\} = [[B_L] + [B_{NL}(u)]]\{u\} \tag{3.15}$$

where B_L is defined in 3.9 and $B_{NL}(u)$ in 3.11.

Now equation 3.1 can be rewritten as:

$$\overrightarrow{\nabla} . \overline{\overline{\sigma}}_{linear}(u) - \overrightarrow{f}_{ext}\, \delta(\overrightarrow{x} - \overrightarrow{x}_{force}) = \psi(u) \tag{3.16-a}$$

$$\psi(u) = -\overrightarrow{\nabla} . \overline{\overline{\sigma}}_{non-linear}(u) \tag{3.16-b}$$

and

$$\{\sigma_{linear}\} = [D][B_L]\{u\} \tag{3.17-a}$$

$$\{\sigma_{non-linear}\} = [D][B_{NL}(u)]\{u\} \tag{3.17-b}$$

This suggests an iterative solution procedure for $\{u\}$:

$$\{u^{k+1}\} = \{u^k\} + \{\Delta u^k\} \tag{3.18}$$

for $k = 1 \ldots n$, n the number of iterations, $\{u^1\} = 0$, with $\{u^k\}$ the previous solution and $\{\Delta u^k\}$ satisfying:

$$\overrightarrow{\nabla}.\overline{\overline{\sigma}}_{linear}\left(\{\Delta u^k\}\right) = \overrightarrow{f}_{ext}\,\delta(\overrightarrow{x} - \overrightarrow{x}_{force}) - \overrightarrow{\nabla}.\left(\overline{\overline{\sigma}}_{linear}\left(\{u^k\}\right) + \overline{\overline{\sigma}}_{non-linear}\left(\{u^k\}\right)\right) \tag{3.19}$$

The solution for $\{u\}$ is reached as soon as $|\Delta u^k| \leq$ tolerance. In practice the linear formulation is sufficiently accurate for small displacements $\{u\}$. However, for the present application to collapsing tubes one expects large displacements, i.e. the non-linear formulation is used, for which the linear solution serves as initial guess.

3.3 Finite-element method (FEM)

In this section the basic concepts of the finite-element method are briefly described. More detailed information on the finite-element method and its numerical implementation can be found in [56].
Posing the problem in general terms, we seek an equation, from which the unknown u can be obtained, in an integral form as:

$$\int_\Omega w\overrightarrow{\nabla}.\overline{\overline{\sigma}}d\Omega = \int_\Omega w\overrightarrow{f}_{ext}\,\delta(\overrightarrow{x} - \overrightarrow{x}_{force})d\Omega \tag{3.20}$$

where $w = w(\overrightarrow{x})$ is a set of prescribed functions, Ω is the domain in which the model is applied and Γ is the boundary of the domain (see figure 3.1). Equation 3.20 can be rewritten as:

$$\int_\Omega \overline{\overline{\sigma}}\overrightarrow{\nabla}.wd\Omega + \int_\Omega w\overrightarrow{f}_{ext}\,\delta(\overrightarrow{x} - \overrightarrow{x}_{force})d\Omega = \int_\Gamma w\left(\overline{\overline{\sigma}}.\overrightarrow{n}\right)d\Gamma = 0 \tag{3.21}$$

This formulation is known as the weighted residuals method.
In the present finite-element method the unknown displacement $\{u(\overrightarrow{x}, t)\}$ is approximated in terms of basis functions, also called shape functions, $N(\overrightarrow{x})$, and the weight function w is chosen equal to the basis functions, i.e. we formulate a Galerkin Finite-Element Method.

In the finite-element method the region Ω, on which the problem is to be solved, is subdivised into nonoverlaping elements (see figure 3.1). The subdivision is called the mesh. The subdivision must satisfy:

- the number of elements Ω^e must be finite
- all elements together must form the complete region Ω
- elements must not overlap. Only the boundaries of an element may coincide with the ones of the neighboring elements.

In each element a finite number of points are chosen, referred to as nodal points. For each nodal point a basis function N_i is defined. These basis functions must satisfy:

- $N_i = 1$ at nodal point i and 0 at all other nodal points.
- within an element, N_i is continuous and at least once differentiable.

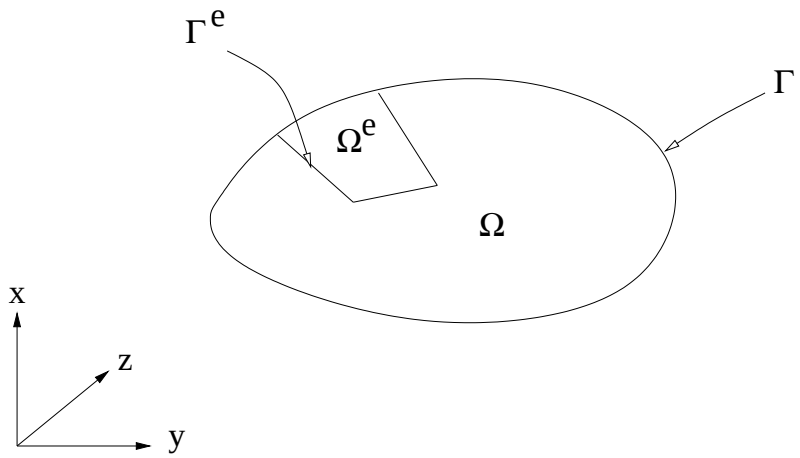

FIGURE 3.1: *Partition of the domain Ω into subdomains Ω^e*

3.3.1 Numerical implementation

Elements

Hexahedral, 20-node (corner nodes and mid-side nodes), elements are used (see figure 3.2). These kind of elements is called the *Serendipity family*.

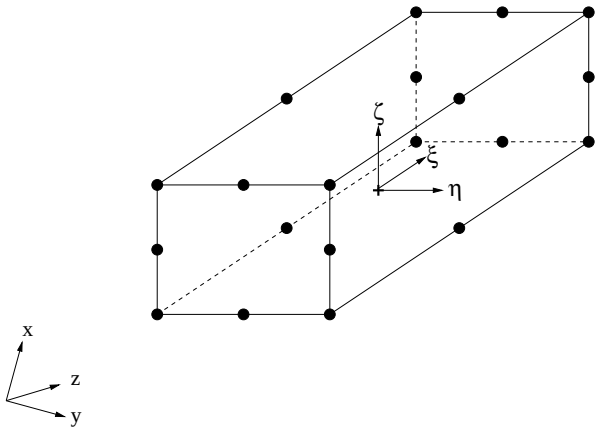

FIGURE 3.2: *20-node hexahedral element (Serendipity family)*

Shape functions

In each element a finite number of points are chosen, referred to as nodal points. For each nodal point a basis function $N_i(\overrightarrow{x})$ is defined such as

$$u^e(\overrightarrow{x}, t) = \sum_{i=1}^{n} u_i(t) N_i(\overrightarrow{x}) \tag{3.22}$$

with $n = 20$ the number of nodes in the element.
The basis functions $N_i(\overrightarrow{x})$ must satisfy:

- $N_i(\overrightarrow{x}) = 1$ in nodal point i and 0 at all other nodal points.
- within an element, $N_i(\overrightarrow{x})$ is continuous and at least once differentiable.

In the local (element) coordinate system ξ, η, ζ with origin at the centroid of the element and ξ, η, ζ the axes along the edges of the element, the 8 corner nodes are at ($\xi = \pm 1, \eta = \pm 1, \zeta = \pm 1$). The 12 mid-side nodes are at ($\xi = 0, \eta = \pm 1, \zeta = \pm 1$) ; ($\xi = \pm 1, \eta = 0, \zeta = \pm 1$) and ($\xi = \pm 1, \eta = \pm 1, \zeta = 0$). For each corner node, we will define shape functions as:

$$N_i(\overrightarrow{\xi}) = \frac{1}{8}(1 + \xi\xi_i)(1 + \eta\eta_i)(1 + \zeta\zeta_i)(\xi\xi_i + \eta\eta_i + \zeta\zeta_i - 2) \tag{3.23}$$

for $\xi \in (-1, 1)$, $\eta \in (-1, 1)$, $\zeta \in (-1, 1)$ and zero outside the element.
A typical mid-side node shape function associated with ($\xi_i = 0$, $\eta_i = \pm 1$ and $\zeta_i = \pm 1$) is:

$$N_i(\overrightarrow{\xi}) = \frac{1}{4}(1 - \xi^2)(1 + \eta\eta_i)(1 + \zeta\zeta_i) \tag{3.24}$$

for $\xi \in (-1, 1)$, $\eta \in (-1, 1)$, $\zeta \in (-1, 1)$ and zero outside the element.

Displacement

The displacement components in the three directions (x, y, z) of each node are:

$$\{u_i\} = \begin{Bmatrix} u_i \\ v_i \\ w_i \end{Bmatrix} \tag{3.25}$$

The vector of the displacements $\{u\}$ is defined as:

$$\begin{aligned} \{u\} &= \{u_1, \ldots, u_i, \ldots, u_n\}^T \\ &= \{u_1, v_1, w_1, \ldots, u_i, v_i, w_i, \ldots, u_n, v_n, w_n\}^T \end{aligned} \tag{3.26}$$

for $i = 1 \ldots n$, with n is the number of nodes.

Linear stiffness matrix

Strain
The strain tensor $\{\epsilon\}$ is defined as a linear form of the displacements as:

$$\{\epsilon\}^e = \sum_{i=1}^{20} [B_i]^e \{u_i\}^e \tag{3.27}$$

where $\{u_i\}^e$ is the displacement vector in one element defined as:

$$\{u_i\}^e = \{u_i, v_i, w_i\}^T \tag{3.28}$$

where i represents the i^{th} node of element e.
$[B_i]^e$ is a (6×3) matrix and is defined at each node of the element e:

$$[B_i]^e = \begin{bmatrix} \frac{\partial N_i}{\partial x} & 0 & 0 \\ 0 & \frac{\partial N_i}{\partial y} & 0 \\ 0 & 0 & \frac{\partial N_i}{\partial z} \\ \frac{\partial N_i}{\partial y} & \frac{\partial N_i}{\partial x} & 0 \\ 0 & \frac{\partial N_i}{\partial z} & \frac{\partial N_i}{\partial y} \\ \frac{\partial N_i}{\partial z} & 0 & \frac{\partial N_i}{\partial x} \end{bmatrix} \tag{3.29}$$

where N_i are the shape functions associated with node i of element e.

Stiffness matrix
The stiffness matrix $[K]$, that represents the stiffness of the material is defined in one element as:

$$[K]^e = \int_{\Omega^e} [B]^{eT} [D] [B]^e \, dV^e \tag{3.30}$$

Assembling equation 3.30 on the domain Ω as:

$$[K] = \sum_{e=1}^{m} [K]^e \tag{3.31}$$

where m is the number of elements and $[K]$ the stiffness matrix of the whole domain, i.e. for all the nodes of the mesh. The linear form of the deformation is rewritten from equation 3.1 as:

$$\left[\int_{\Omega} [B]^T [D] [B] \, dV \right] \{u\} = \{f_{ext}\} \tag{3.32}$$

$\{f_{ext}\}$ is the $(3n \times 1)$ vector associated with the external loads, $\{u\}$ is the $(3n \times 1)$ vector of the unknown displacements, and $[K]$ is a $(3n \times 3n)$ symmetric matrix, where n is the number of nodes.

Equilibrium equation

The equilibrium equation, i.e. the balance between internal and external forces, is defined as:

$$\{\psi^k\} = \left\{ \int_{\Omega} \left[\bar{B}\right]^T \{\sigma\} \, dV \right\} - \{f_{ext}\} \tag{3.33}$$

Superscript k denotes the iteration at the previous step.
The matrix $\left[\bar{B}\right]$ is now defined as a non-linear form of the displacements. It will be detailed in the next section (*Non-linear calculation*), but can be simply expressed as a linear part $[B_L]$ and a non-linear part $[B_{NL}(u)]$:

$$\left[\bar{B}\right] = [B_L] + [B_{NL}(u)] \tag{3.34}$$

The linear part $[B_L]$ is the one defined by equation 3.9. $\{\psi^k\}$ are the residuals of the balance of the total forces acting on the body, and should theoretically be equal to zero. If not, the force balance is not fulfilled, and a correction of the deformation is given by a non-linear calculation of the displacements.

Non-linear strain-displacement relation

In the same way as for the linear stiffness matrix $[K]$, the non-linear stiffness matrix $\left[\bar{K}\right]$ can be expressed as:

$$\left[\bar{K}\right] = [K_L] + [K_{NL}] = \int_\Omega \left[\bar{B}\right]^T [D] \left[\bar{B}\right] dV \tag{3.35}$$

where $\left[\bar{B}\right] = [B_L] + [B_{NL}(u)]$ and $[B_{NL}(u)]$ is defined by equation 3.11.
$[K_L]$ is the linear stiffness matrix $[K]$ (see equation 3.31), and $[K_{NL}]$ is the geometrical non-linear part defined as:

$$[K_{NL}] = \int_\Omega [B_{NL}]^T [D] [B_{NL}] dV \tag{3.36}$$

The correction $\{\Delta u^k\}$ of the deformation needed if the residuals $\{\psi^k\}$ are not equal to zero, is calculated as:

$$\left[\bar{K}\right] \{\Delta u^k\} = \left[\int_\Omega \left[\bar{B}\right]^T [D] \left[\bar{B}\right] dV\right] \{\Delta u^k\} = -\{\psi^k\} \tag{3.37}$$

where $\{\psi^k\}$ is the vector of the residuals of the force balance at step k. $\left[\bar{K}\right]$ is the non-linear stiffness matrix representing the properties of the material, and $\{\Delta u^k\}$ is the vector of the correction of the displacement.
The update of the displacements is given by:

$$\{u^{k+1}\} = \{u^k\} + \{\Delta u^k\} \tag{3.38}$$

$\{u^{k+1}\}$ gives a more accurate deformation of the body. This non-linear calculation can be repeated as long as the residuals $\{\psi^k\}$ are too large.

3.3.2 Boundary conditions

Three types of boundary conditions are used in the present study.

1. Clamped ends
   The body is clamped at one or two ends. That is, the displacements for all degrees of freedom: u, v, w of each of the nodes at the clamped edges are set to zero.
2. Symmetry. The nodes in the plane of symmetry remain within the plane of symmetry.
3. Wall contact. In case wall contact occurs, the nodes associated with the contact must remain in the plane of symmetry at which contact occurs.

Prescribed displacements
Once the system of equations is established, the boundary conditions must be incorporated.

Clearly, the equations cannot be solved without applying the boundary equations. A minimum number of prescribed displacements is needed to prevent unlimited rigid body motion. Mathematically, this is interpreted as the stiffness matrix being singular, i.e. the inverse of the stiffness matrix does not exist ([10]).
We will rewrite the equations in order to isolate the degrees of freedom affected by the boundary conditions:

$$\begin{bmatrix} [K_{11}] & [K_{12}] \\ [K_{21}] & [K_{22}] \end{bmatrix} \begin{Bmatrix} \{u_1\} \\ \{u_2\} \end{Bmatrix} = \begin{Bmatrix} \{f_1\} \\ \{f_2\} \end{Bmatrix} \tag{3.39}$$

where $\{u_1\}$ is the vector of unknowns, $\{u_2\}$ is the vector of the specified degrees of freedom. Equation 3.39 can be rewritten as:

$$\begin{bmatrix} [K_{11}] & [0] \\ [K_{21}] & [K_{22}] \end{bmatrix} \begin{Bmatrix} \{u_1\} \\ \{u_2\} \end{Bmatrix} = \begin{Bmatrix} \{f_1\} - [K_{12}]\{u_2\} \\ \{f_2\} \end{Bmatrix} = \begin{Bmatrix} \{f_1^*\} \\ \{f_2^*\} \end{Bmatrix} \tag{3.40}$$

From the first line of equation 3.40, $\{u_1\}$ can be evaluated, as being the only unknown of the equation. The second line is thus redondant. However, we will retain it and rewrite it to conserve the symmetry and the dimensions of the system. We will rewrite the system as:

$$\begin{bmatrix} [K_{11}] & [0] \\ [0] & [I] \end{bmatrix} \begin{Bmatrix} \{u_1\} \\ \{u_2\} \end{Bmatrix} = \begin{Bmatrix} \{f_1^*\} \\ \{u_2\} \end{Bmatrix} \tag{3.41}$$

For the cases 1 and 2 specified above, the displacements of the degrees of freedom will be set to zero, i.e. $\{u_2\}$ is a zero vector. The system is now complete, and the solution $\{u_1\}$ can be computed.

Contact condition
For reason of symmetry it is possible to consider only a part of a tube. When the collapse is such that wall contact occurs, wall contact will occur in a plane of symmetry.
The contact condition is implemented in two steps:

- First, when contact arises, the coordinates X^i of the nodes concerned will become negative, i.e. they will cross the plane of symmetry. These nodes will be forced to move to the location of the contact by setting: $\{u_2^i\} = -X^i$. Furthermore, the other nodes will be affected by a load: $-\left[K_{12}^i\right]\{u_2^i)\}$, following equation 3.40 ($\left[K_{12}^i\right]$ represents the term of $[K_{12}]$ corresponding to the nodes i).
- Then, the contact nodes are forced to remain at the contact, which will be obtained by setting the vector: $\{u_2^i\}$ to zero.

3.4 Validation

The deformation of a body, such as a bar or a tube, under external loads is considered. Linear as well as non-linear cases are handled. For the validation three test-cases are investigated:

1. *deformation of a bar under discrete load*
   The deformation will be compared with the analytic solution. The stress will also be investigated.

2. *deformation of a tube under discrete load*
   The results will be compared with the ones produced with the commercial package ANSYS.

3. *deformation of a tube under distributed load*
   As first step, the calculation will be performed for a quarter of a tube. As for the bar, the deformation will be compared with the analytical solution, and a stress analysis will be conducted. As second step, calculations for a complete tube will be performed, in order to verify the symmetry conditions used in the model.

3.4.1 Deformation of a bar under discrete load

The bending of a bar is investigated in this section. A bar, clamped at one end, is put under external load (for example, a weight at the end). The analytical solution of the bending (maximum deflection, bending moment) is known for the 1-dimensional case (see [15]). Calculations are performed for long bars, which can be considered in a 1-dimensional approximation. The results are compared with the analytical solution.

Deformation

The geometry investigated is presented in figure 3.3. The square bar, of length $L = 1\ m$ and height $h = 0.01\ m$, is clamped at the end $z = 0$. A load $F = -F_y = -10^{-3}\ N$ is applied in the last section ($z = L$). The calculation is performed with an elasticity defined by the Young modulus $E = 10^7\ Pa$ and the Poisson ratio $\nu = 0$.

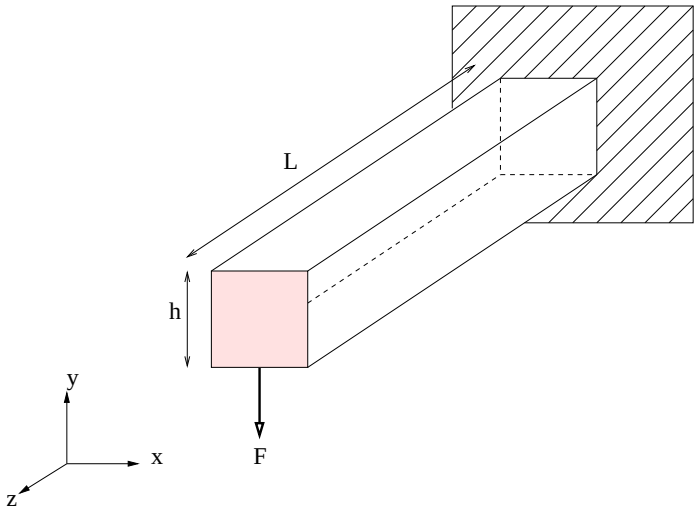

FIGURE 3.3: *Bending of a square bar. The load is a discrete force: $F = -F_y$, applied at the end $(z = L)$. The bar is clamped at $(z = 0)$.*

The analytical solution gives the maximum deflection δ (which is the deflection at $z = L$) as:

$$\delta = \frac{FL^3}{3EI} \tag{3.42}$$

where F is the applied force, L is the length of the bar, E is the Young modulus and I is the moment of inertia. Since the cross-section of the bar considered is square, the moments of inertia I_x and I_y are equal: $I_x = I_y = I$.
The moment of inertia I for a square section of side h is derived in *Appendix A*:

$$I = \frac{h^4}{12} \tag{3.43}$$

For the case considered: $I = 8.33.10^{-10}\ m^4$, yielding in a maximum deflection of $\delta = -0.04\ m$.

The mesh used contains 100 elements ($1 \times 1 \times 100$) and thus 1208 nodes. Since the nodes are ordered section by section from the clamped end to the free end, the node numbering corresponds to the coordinate in the z-direction.
The deformation calculated is shown in figure 3.4. The displacements in the y-direction are plotted versus the z-coordinate, i.e. in the axial direction, for both the linear and the non-linear case. At $z = 0$, the displacement is zero, since the bar is clamped. The displacement v at $z = L$, where the maximum deflection of the bar occurs, is: $v(z = L) = -0.04\ m$ for the linear case. This result exactly equals the one predicted by the analytical solution.
The figure shows also the deflection for the non-linear case. The bending of the bar is slightly larger, and the maximum deflection is computed as: $v(z = L) = -0.042\ m$. The deformation found for the non-linear case may be expected to be almost identical to the deformation for the linear case since the deflection is small ($(\delta/L) \simeq 0.04 = 4h/L$).

Stress analysis

Next, the normal stresses that appear in the bar during the bending are considered. The dimensions of the square bar: $L = 1\ m$, $h = 0.01\ m$, the applied load: $F = -10^{-3}\ N$ and the elastic properties: $E = 10^7\ Pa$, $\nu = 0$ are unchanged. The mesh used again contains 100 elements ($1 \times 1 \times 100$) and 1208 nodes.
The force F applied at the end of the bar, along the negative y-axis, induces a shear force V, in opposite direction, and a bending moment M, with the same sign as the force (see [15], p:223). In this case, $F = -F_y < 0$, thus $M < 0$ (see figure 3.5).
The normal stress σ_z is related to the bending moment as (see [15], p:260):

$$\sigma_z = \frac{My}{I} \tag{3.44}$$

where $I = I_x = I_y$ is the moment of inertia of the square section of the bar (see equation 3.43).
The bending moment M is a function of the force F and the distance to the point of application of this load:

$$M = F(z_{max} - z) \tag{3.45}$$

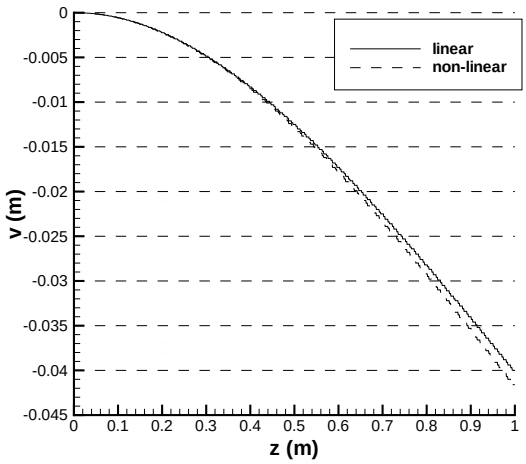

FIGURE 3.4: *Bending of a square bar (discrete load). The displacements in y-direction are plotted versus the z-coordinate (i.e. in the axial direction), for linear and non-linear case.* $L = 1\ m$, $h = 0.01\ m$, $E = 10^7\ Pa$, $\nu = 0$, $F = -F_y = -10^{-3}\ N$; *mesh:* $100 * 1 * 1$ *in the* $z-, x-$ *and* $y-$ *directions.*

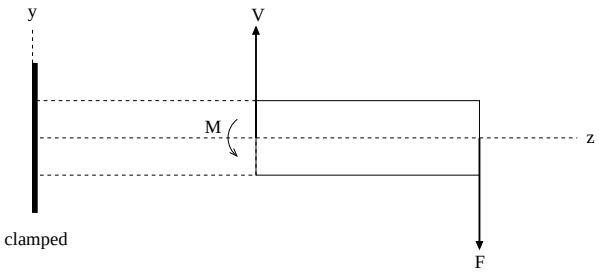

FIGURE 3.5: *Force and moment balance in a bar.*

where $z_{max} = L$ is the location of the free end.
Since $M < 0$ and $I > 0$, the normal stress σ_z is of the same sign as y, i.e. is positive when $y > 0$ (upper half of the bar) - tensile stress - and negative when $y < 0$ (lower half of the bar) - compressive stress (see figure 3.6). When $y = 0$, i.e. the mid-side plane of the bar, $\sigma_z = 0$.
For the non-linear case, the normal stress σ_z is given in figure 3.7. The stress calculated at the integration points is plotted as a function of the elements number; the first element being at the clamped end at $z = 0$, the last element is at the free end at $z = z_{max}$. In each element, three stresses are selected: in the upper ($y > 0$) and lower ($y < 0$) part of the bar, and at the mid-side plane ($y = 0$).
Clearly, we can see the positive, negative and zero stress, as predicted. The stress is maximal at the clamped end ($z = 0$) and decreases linearly to zero at the free end at $z = z_{max} = L$, as predicted by equations 3.44 and 3.45. The maximum stress, at $z = 0$, is: $\sigma_z^{max}(z = 0) =$

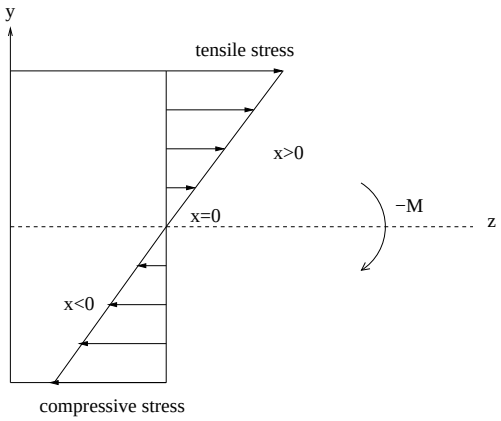

FIGURE 3.6: *Normal stress in a bended beam.*

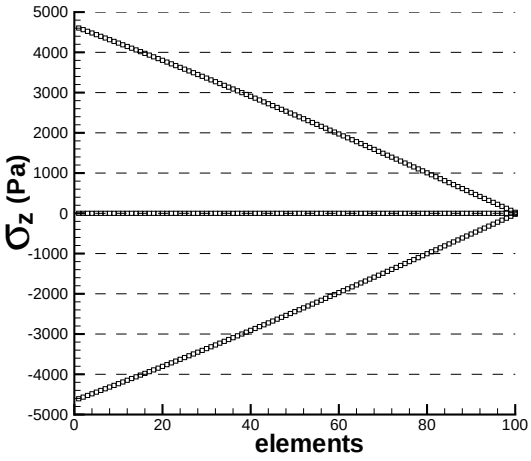

FIGURE 3.7: *Normal stress in a bar, clamped at the first section ($z = 0$) and loaded at the last section ($z = z_{max}$)*

$4600\ Pa$.
From equations 3.43, 3.44 and 3.45, the analytical solution can be calculated as: $\sigma_z^{max} = 4647\ Pa$. Again, the agreement between the results of the numerical simulation and the analytical solution is very good.

3.4.2 Deformation of a tube under discrete load

In this section the load is a discrete force. We consider a tube clamped at one end ($z = 0$ plane), as shown on figure 3.8. The length of the tube is L and R_{in} and R_{out} are the radii of the internal and external cylinder,respectively. The discrete force is located within the $y = 0$

plane, at ($x = \pm Rout, y = 0, z = 3/5L$), which implies that there are two planes of symmetry: the plane $x = 0$ and the plane $y = 0$. Therefore, we need to consider only one quarter of the tube. Symmetry is enforced by setting the displacements in the x-direction for the nodes in the $x = 0$ plane and the displacements in the y-direction for the nodes in the $y = 0$ plane to zero. The force is pointing in the direction towards the tube: $F = -F_x$. The dimensions

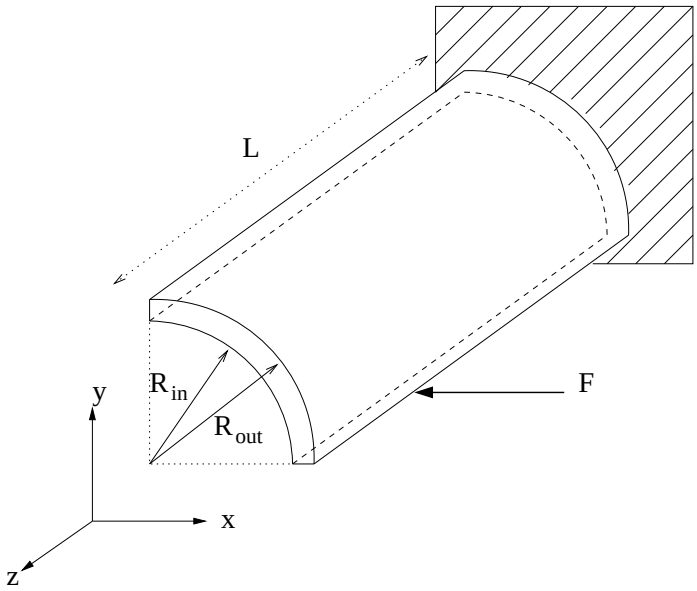

FIGURE 3.8: *Tube clamped at one side subject to a discrete force. The load is a discrete force: $F = -F_x$, applied at the point $(x = \pm R_{out}, y = 0, z = \frac{3}{5}L)$. Because of symmetry it suffices to consider one quarter of the tube only.*

of the tube are $L = 50\ m$, $R_{in} = 10\ m$ and $R_{out} = 11\ m$. The elasticity is defined by the Young modulus E and the Poisson ratio ν: $E = 7.10^{10}\ Pa$, $\nu = 0.3$. The load is: $F_x = 10^9\ N$.

The mesh used contains 50, 20-node, hexahedral elements: $1 * 10 * 5$ elements in cylindrical coordinates r, θ, z, which yields 428 nodes. Since there are 10 elements in the circumferential direction, and the elements have mid-side nodes, the cross-section in the planes $z = 0$ and $z = L$ counts 53 nodes.

The deformation (see the deformed shape, figure 3.9d), where by symmetry a complete tube has been reconstructed, is compared with the deformation obtained with the commercial package ANSYS. Calculations with ANSYS have been performed with the same data: same mesh (50 elements), same type of elements (20 nodes, hexahedral elements).

In figure 3.9, the displacements of the inside nodes of the last section ($z = L, x > 0, y > 0$) in all three directions x, y, z are presented, for both the linear and the non-linear case. The first node (node $= 1$) initially corresponds to ($x = R_{in}, y = 0, z = L$). The last node (node $= 21$) initially corresponds to ($x = 0, y = R_{in}, z = L$). The results are compared with the ones produced by ANSYS.

The simulation for the linear case (see section *Numerical implementation*) gives the main deformation: a collapse of the tube starts in the x-direction (in the direction of the force applied), while, by reaction, it inflates in the y-direction. The displacements in the z-direction (axial extension) are small and non-significant compared to the displacements in the two other directions. The results of the simulations are in a very good agreement with the ones produced with ANSYS, since the displacements in all directions are found to be exactly the same.
The simulation for non-linear case (see also section *Numerical implementation*) gives a correction to the deformation obtained for the linear case. The effect is that the displacements in the x-direction are slightly larger, i.e. the collapse increases. Again, the results of the simulation is in good agreement with ANSYS, as long as displacements in x-direction as considered. Displacements in y and z-direction differ slightly.
In the non-linear case the convergence is reached with about 30 iterations.

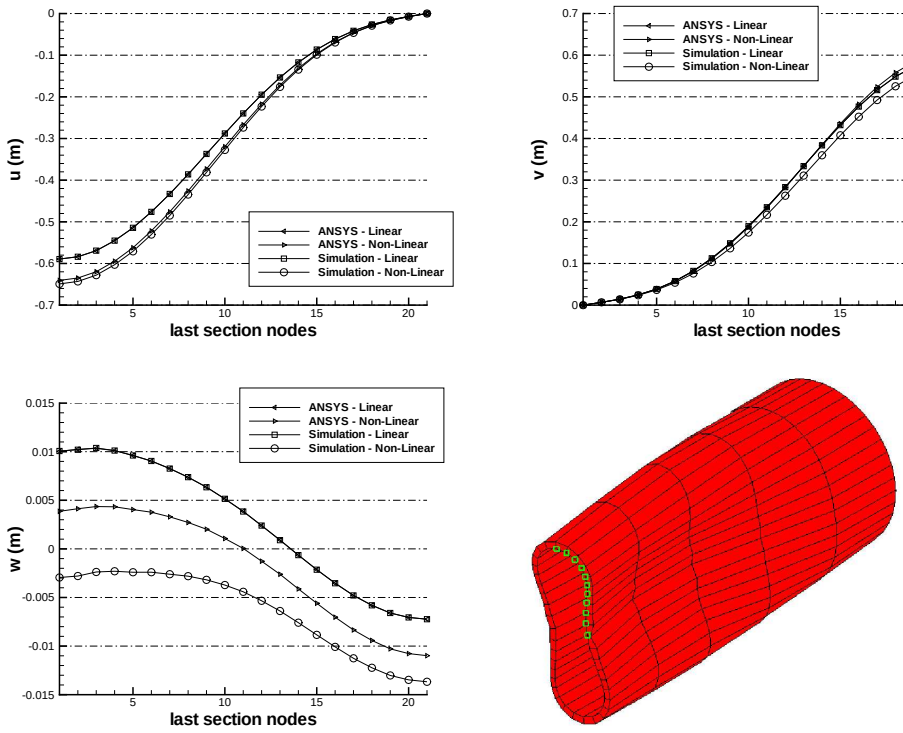

FIGURE 3.9: *Tube clamped at one end ($z = 0$) subject to a discrete force applied at ($x = \pm R_{out}, y = 0, z = \frac{3}{5}L$). Displacements in x, y and z direction for the inside nodes in the last section, for the linear and the non-linear case. Results are compared with the ones produced with ANSYS. Due to symmetry, the deformation is computed for the fourth quarter of the tube. $L = 50\ m$, $R_{in} = 10\ m$, $R_{out} = 11\ m$, $E = 7.10^{10}\ Pa$, $\nu = 0.3$; mesh: $5 * 10 * 1$ in the z, θ, R directions.*

3.4.3 Deformation of a tube under distributed load

Complete tube

The bending of a hollow tube is presented in this section. A sketch of this case is given in figure 3.10. The hollow tube is clamped at one end ($z = 0$). A force F in negative $y-$direction is applied at the other end ($z = z_{max}$), which is distributed uniformly over the section $z = z_{max}$.
By analogy, this case can be compared to the one-dimensional analytical solution presented in the previous section *Bending of a bar* (see figure 3.3). However, the moment of inertia for a circular ring instead of a rectangular cross-section must be used in the analytical expressions. To be able to compare results with those of the one-dimensional case, the dimensions of the tube must be such that three-dimensional effects are minimized, i.e. the length L of the tube must be much larger than the diameter D of the cross-section: $L \gg D$. Also, the thickness t of the ring must be a lot smaller than the mean radius r: $t \ll r$, as required in the derivation of the moment of inertia (equation 3.46).

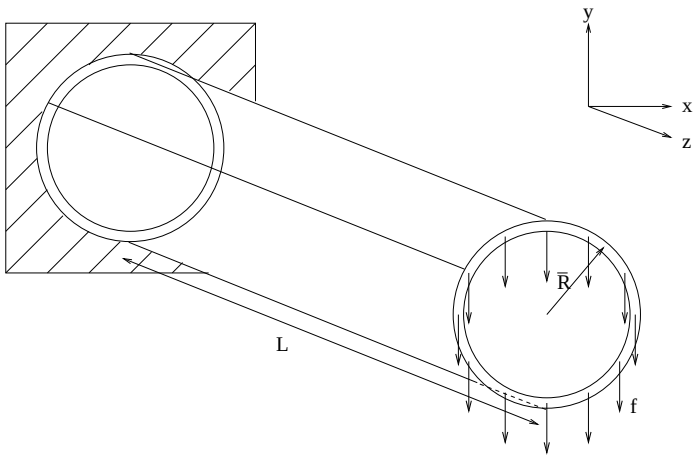

FIGURE 3.10: *Bending of a tube: a load $F = -F_y$ is applied uniformly distributed at the end of a clamped tube. $F = 2\pi R f$, f is the force applied per unit length.*

Moment of inertia
The moment of inertia of a circular ring is derived in *Appendix A*. Assuming that the thickness t of the ring is much smaller than the mean radius r: $t \ll r$, the moment of inertia can be calculated as:

$$I = I_x = I_y = \pi r^3 t = \frac{\pi D^3 t}{8} \tag{3.46}$$

The moments of inertia I_x and I_y with respect to x and y, respectively, are equal since these are axes of symmetry of the circular ring.

Deformation

The simulation was performed using $r = 5.05\ 10^{-3}\ m$, $t = 10^{-4}\ m$, $L = 1\ m$, $E = 10^6\ Pa$, $\nu = 0$ and $F = -10^{-5}\ N$.
The mesh contains 200 elements ($1 \times 10 \times 20$ in radial, circumferential and axial direction) and 1450 nodes. Note that now the whole tube is discretized, though the plane $x = 0$ is a plane of symmetry.
The moment of inertia is calculated from equation 3.46: $I = 4.046.10^{-11}\ m^4$. The analytical solution of the maximum deflection (equation 3.42) is: $\delta = 8.24.10^{-2}\ m$.
In figure 3.11, the displacements in the x-direction of all the nodes are plotted, for both the linear and the non-linear calculations. The maximum deflection is found at the end of the tube, where the load is applied. For the linear calculation, the maximum deflection is: $v_{max} = 8.23.10^{-2}\ m$, which closely matches the result of the one-dimensional analytical solution.
Since the deformation is small, the non-linear case gives only a small correction to this displacement.

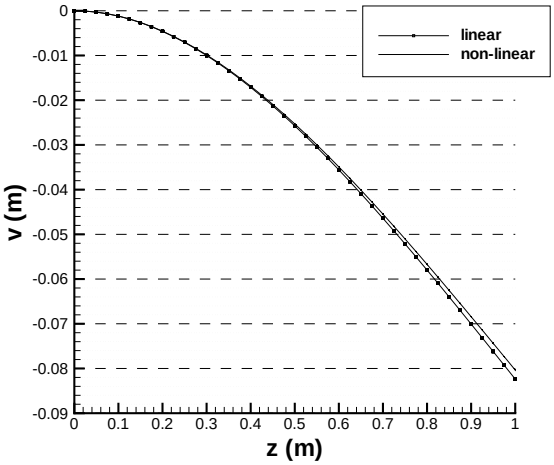

FIGURE 3.11: *Bending of a thin walled beam of circular cross-section, clamped at the first section ($z = 0$) and uniformly loaded at the last section ($F = F_{z_{max}}(y)$). The displacements in y-direction are plotted versus the z-coordinate (i.e. in the axial direction), for linear and non-linear calculations. $L = 1\ m$, $r = 5.05.10^{-3}\ m$, $t = 10^{-4}\ m$, $E = 10^6\ Pa$, $\nu = 0$; mesh: $1 * 10 * 20$ in the r, θ, z directions.*

Stress analysis

From equations 3.44 and 3.45, the normal stress is defined as:

$$\sigma_z = \frac{My}{I} = \frac{F(z_{max} - z)y}{I} \tag{3.47}$$

For a square bar, x was the half side of a section(see figure 3.5). By analogy, for a tube, x is defined as: $x = r \sin\theta$ (see figure 3.12).

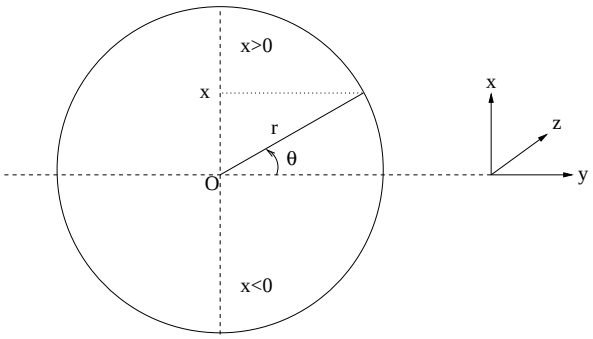

FIGURE 3.12: *Definition of x*

In this case, the load F is applied as $F = -F_y$. In figure 3.13, the stress in axial direction σ_z is depicted for the non-linear case. The stress is on the ordinate and the sections of the tube are on the abscissa. Within one section, the symmetry of σ_z, from a positive maximum ($x = r, y = 0$), through 0 ($x = 0, y = r$) and to a negative maximum ($x = -r, y = 0$) can be observed. The other half of the tube ($y < 0$) is completely symmetric. The non-linear case gives as maximum normal stress (see figure 3.13): $\sigma_z^{max} = 1148\ Pa$.
The one-dimensional analytical solution for the maximum normal stress, found at ($x = r, y = 0$), is calculated from equation 3.47 as: $\sigma_z^{max} = 1185\ Pa$.

Semi-tube

In the previous section, the bending of a hollow tube was investigated. The results matched the analytical, one-dimensional solution for the maximum deflection as well as for the normal stress. Now, the case of semi-a tube, clamped at one side, and loaded at the free side, is performed. Because of symmetry we consider one quarter of a tube with symmetry conditions. This permits to check if the boundary conditions are correctly implemented.

Moment of inertia

For a section of a semi circular ring, the x-axis is not an axis of symmetry. Thus, the two moments of inertia with respect to the x-axis I_x for a circular ring cannot be used in this case. Instead, the moment of inertia will be taken with respect to an axis BB, parallel to the y-axis (as the load will be applied in the x-axis) and passing through the centroid C (see *Appendix A* for more information).
The moment of inertia for a semi circular ring is:

$$I_{BB} = \frac{\pi}{4}(b^2 - a^2)\bar{y}^2 - \frac{2}{3}(b^3 - a^3)\bar{y} + \frac{\pi}{16}(b^4 - a^4) \tag{3.48}$$

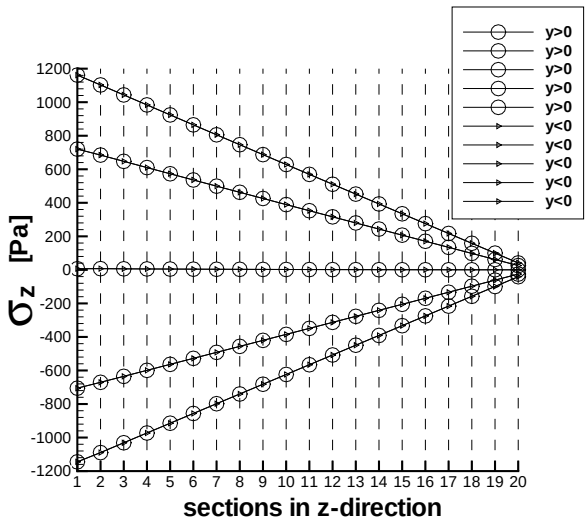

FIGURE 3.13: *Normal stress in a thin walled circular beam, clamped at the first section ($z = 0$) and uniformly loaded at the last section ($z = z_{max}$). $L = 1\ m$, $r = 5.05.10^{-3}\ m$, $t = 10^{-4}\ m$, $E = 10^6\ Pa$, $\nu = 0$; mesh: $1 * 10 * 20$ in the r, θ, z directions.*

where a and b are the radii of the two concentric circles of the ring, and $\bar{x}, \bar{y}$ are the coordinates of the centroid, calculated as:

$$\bar{x} = \bar{y} = \frac{4}{3\pi} \frac{b^3 - a^3}{b^2 - a^2} \tag{3.49}$$

Deformation

A sketch of the model is given in figure 3.14. A distributed load $f = -f_y$ is applied at the last section $z = z_{max}$, and the tube is clamped at the first section $z = 0$. To be able to compare the results with the one-dimensional analytical solution, the tube is such that the length L is a lot larger than the mean radius r, and the thickness t is a lot smaller than the mean radius.
The calculations were performed with the same dimensions as for the case of the complete tube, i.e.: $r = 5.05\ 10^{-3}\ m$, $t = 1\ 10^{-4}\ m$, $L = 1\ m$, $E = 10^6\ Pa$, $\nu = 0$. However, the load: $F = -5 * 10^{-7}\ N$ is markedly reduced.
The mesh contains 100 elements ($1 \times 10 \times 20$) and 828 nodes.

From equation 3.48, the moment of inertia is calculated as: $I_{BB} = 1.92\ 10^{-12}\ m^4$. And the analytical solution for the maximum deflection is calculated from equation 3.42 as: $\delta = 8.7\ 10^{-2}\ m$.
The displacements in y-direction for the linear and non-linear calculation are given in figure 3.15. The displacements for the last nodes, located at $z = z_{max}$, show the maximum deflection. For the linear calculation, we find: $v_{max} = 8.68\ 10^{-2}\ m$, which matches the analytical solution.
As for the tube, the difference between the linear and non-linear calculated displacements is

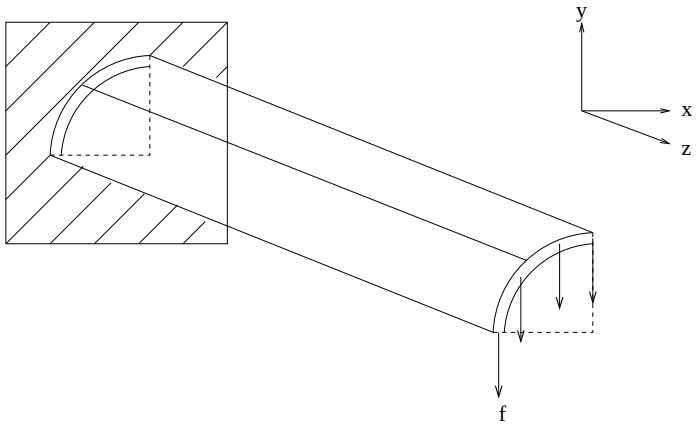

FIGURE 3.14: *Bending of a semi-tube: a distributed load f is applied at the end of a clamped semi-tube. Only one quarter of the tube is considered because of symmetry with respect to the vertical plane.*

small, since the deformation is small.

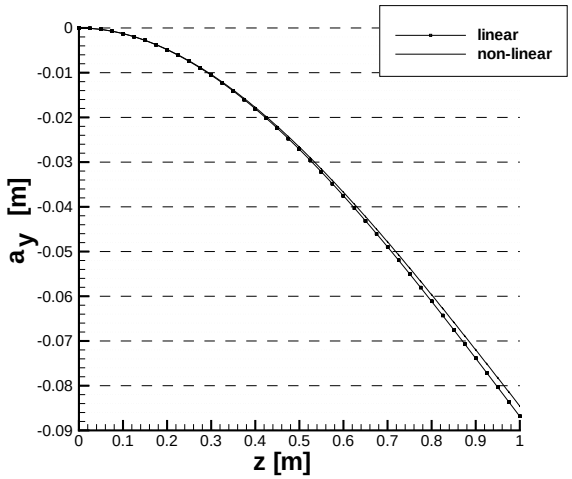

FIGURE 3.15: *Bending of a thin walled semi-tube, clamped at the first section ($z = 0$) and loaded at the last section ($F = F_{z_{max}}(y)$). The displacements in y-direction are plotted versus the z-coordinate (i.e. in the axial direction), for linear and non-linear calculations.*

Stress analysis

The normal stress is still calculated from equation 3.47 as:

$$\sigma_z = \frac{My}{I} = \frac{F(z_{max} - z)y}{I} \tag{3.50}$$

However, the definition for x is different than the one for the tube. The axis of reference, which was the x-axis for the tube, is now the BB-axis. Thus x varies from $-\bar{x}$ to $r - \bar{x}$, where $\bar{x}$ is the x-coordinate of the centroid, and r is still the mean radius of the circular ring (see figure 3.16).
In our case, $\bar{x} = 3.215\ 10^{-3}$ (see equation 3.49). From equation 3.47, we find as analytical solution for the maximum positive and negative normal stress ($x = r, y = 0, z = L$ and $x = 0, y = r, z = L$, respectively):

$\sigma_z^+(r, 0, L) = 475\ Pa$
$\sigma_z^-(0, r, L) = -705.7\ Pa$

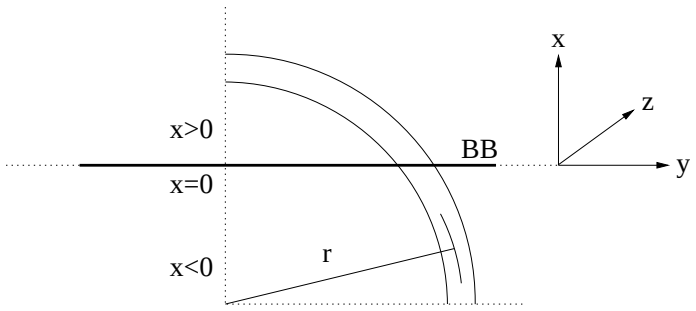

FIGURE 3.16: *Definition of x*

The results of the non-linear calculation for the normal stress are plotted in figure 3.17.
σ_z is positive when $x > \bar{x}$ and negative when $x < \bar{x}$. The positive and negative maximum are found as:

$\sigma_z^+(r, 0, L) = 432\ Pa$
$\sigma_z^-(0, r, L) = -652\ Pa$

3.5 Tube law

The tube law was introduced in section 1.4.2, see also figure 1.6. It gives a relation between the dimensionless transmural pressure $P = p_{tm}/K_p$ with $K_p = E(h/R)^3/[12(1 - \nu^2)]$ and the dimensionless area $\alpha = A/A_0$ for an infinitely long tube subjected to a constant transmural pressure p_{tm}.
A stability analysis (see [14]) shows that three parts of the tube law must be considered.

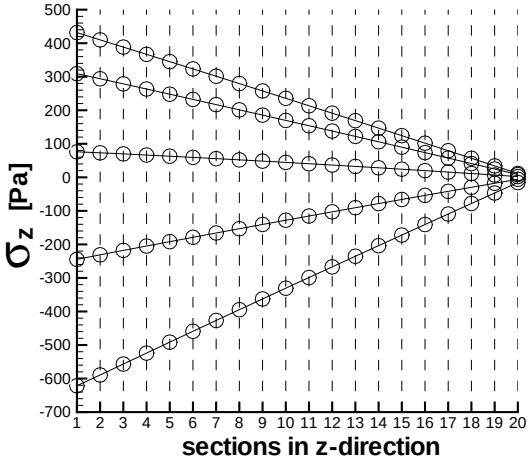

FIGURE 3.17: *Normal stress in a thin walled semi-tube, clamped at the first section ($z = 0$) and loaded at the last section ($z = z_{max}$)*

The case considered here refers to an initially almost perfect circular cylinder. This cylinder will not buckle for $P(\alpha)$ above -3. For $P(\alpha) \leq -3$ ($\alpha \sim 0.4$) the tube experiences large changes in cross-sectional area for a small change of the pressure. The shape of the buckling cross-section remains elliptical. At $\alpha = 0.27$, point contact occurs, which means that opposite walls get into contact. The cross-section consists now of two lobes. When the transmural pressure increases further, the contact area increases and the open portion of the cross-section is reduced but remains similar in shape. A line contact appears at $\alpha = 0.21$. Actually, between point contact at $\alpha = 0.27$ and line contact at $\alpha = 0.21$ a very rapid decrease in transmural pressure to large negative values is observed. After line contact, the change in area of the tube cross-section decreases slowly as the transmural pressure decreases rapidly.

Employing the present finite-element method the case is considered of a tube of finite length L and diameter D. The tube wall is subjected to a constant pressure difference, p_{tm}, the external pressure being higher than the internal pressure. Both ends of the tube are clamped. It is assumed that the tube has two planes of symmetry, which allows a two-lobe shape to develop. The initial shape of the tube is elliptical with the ratio of the minor axis and the major axis being equal to $0.9/1.1$. The thickness of the wall of the tube equals 10 % of the averaged radius of the tube, i.e. $h/R = 0.1$.
The solution of the problem, e.g. the cross-sectional area $A(z)/A_0$, depends on P, defined above, and on L/D. Of course the end conditions (clamped here) will also have an influence on the solution, but for $L/D \gg 1$ the tube law should be recovered.
The values chosen for the different parameters are: $E = 1 * 10^4\ Pa$, $\nu = 0.3\ [-]$, $h/R = 0.1$ (resulting in $K_p = 0.9157\ Pa$), $D = 0.2\ m$, $L/D = 5$, 10 and 20, $P = (p - p_{ext})/Kp = 0$ to -15.
The quarter tube wall is discretized with 10, 20-node elements in azimuthal direction. In radial direction one element is used, primarily because the present implementation of the

method is restricted to one element in this direction. It is expected that for the relatively thin tube walls considered in the present study that this is adequate. In axial direction the number of elements depends on L/D, i.e. we choose $2 * L/D$ elements, which implies that the size of the elements is independent of the length of the tube. The solution is obtained by starting at a small value of P, obtain the converged solution and subsequently using this as the initial guess for the solution at a somewhat smaller value of P, etc.

The results of the present method, in the form of the dimensionless minimum cross-sectional area $\alpha = A^*/A_0$ as function of the dimensionless pressure difference P, are presented in figure 3.18. It shows that the result for $L/D = 10$ and $L/D = 20$ do not differ very much, indicating that the asymptotically two-dimensional solution is obtained for $L/D = 10$. It also shows that the shorter tube deforms less than the longer tube, i.e. the shorter the tube the stiffer. The solution shows that for small negative values of P the deformation is small but that for $P < -3$ ($\alpha \simeq 0.9$) the tube cross-sectional area decreases rapidly, more or less linearly with P (slope $dP/d\alpha \simeq 5.6$). For P around -6.5 ($\alpha \simeq 0.28$) the opposite tube walls touch, which discontinuously slows down the decrease in cross-sectional area. For $P < -6$ the cross-sectional area decreases linearly with slope $dP/d\alpha \simeq 85$.
Comparison of the present results with results for an infinite tube obtained with ANSYS shows a reasonable agreement. Differences may be due to differences in the mesh, specifically the number of elements used across the wall thickness.
The present results also illustrate that though the two forms of the tube law, i.e. $P(\alpha) = -\alpha^{-3/2}$ and $P(\alpha) = 1 - \alpha^{-3/2}$ of Flaherty et al. ([12]), give an adequate correlation for $P < -6$, the correlation for mildly loaded tubes is poor. For a given loading P the tube deforms much more according to the tube law than predicted by the present method.

In order to investigate the influence of the mesh on the solution we computed the solution for the case $L/D = 5$ for a number of meshes, i.e. a mesh of $5 * 5 * 1$, the one used for figure 3.18, namely $10 * 10 * 1$ and the $20 * 20 * 1$ mesh. The results are presented in figure 3.19. This figure indicates that the result for the $10 * 10 * 1$ mesh is very similar to the one for $20 * 20 * 1$ and may therefore be considered to be grid-converged. It motivated the choice for the meshes used for obtaining the results of figure 3.18. In the result for the coarse mesh and to a lesser extent in the result for the medium mesh, slope discontinuities are present. Analysis of the numerical results indicated that each slope discontinuity is related to an increase by one of the number of elements of the opposite tube walls that are in contact.

Figure 3.20 presents the shape of the geometry for a number of values of the dimensionless transmural pressure. Initially the deformation of the tube walls increases rapidly for decreasing P. For $P < -6.5$ two opposite tube walls start to come into contact and the deformation is less rapid for decreasing P.

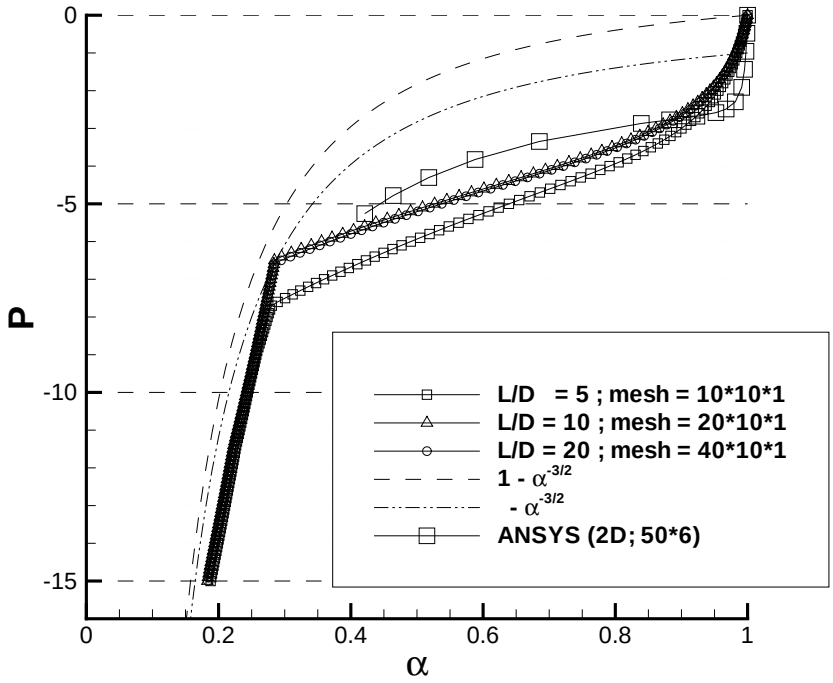

FIGURE 3.18: *The tube law. A comparison of the present results for different L/D with two relationships ($P(\alpha) = p_{tm}/K_p = -\alpha^{-3/2}$ and $P(\alpha) = p_{tm}/K_p = 1 - \alpha^{-3/2}$, with $\alpha = A_{min}/A_0$ ([12])) is presented. Also included is the result of a two-dimensional calculation ($L/D = \infty$, mesh $50 * 6$) using the software ANSYS. $K_p = E(h/R)^3/(12 * (1 - \nu^2))$.*

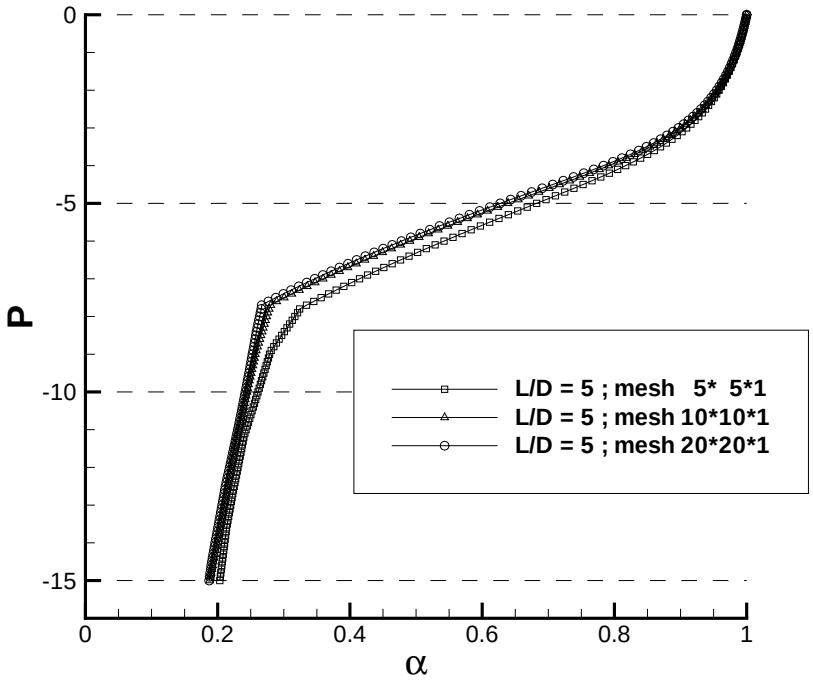

FIGURE 3.19: *Result for a tube with $L/D = 5$ for different meshes: 5*5*1, 10*10*1, 20*20*1.*

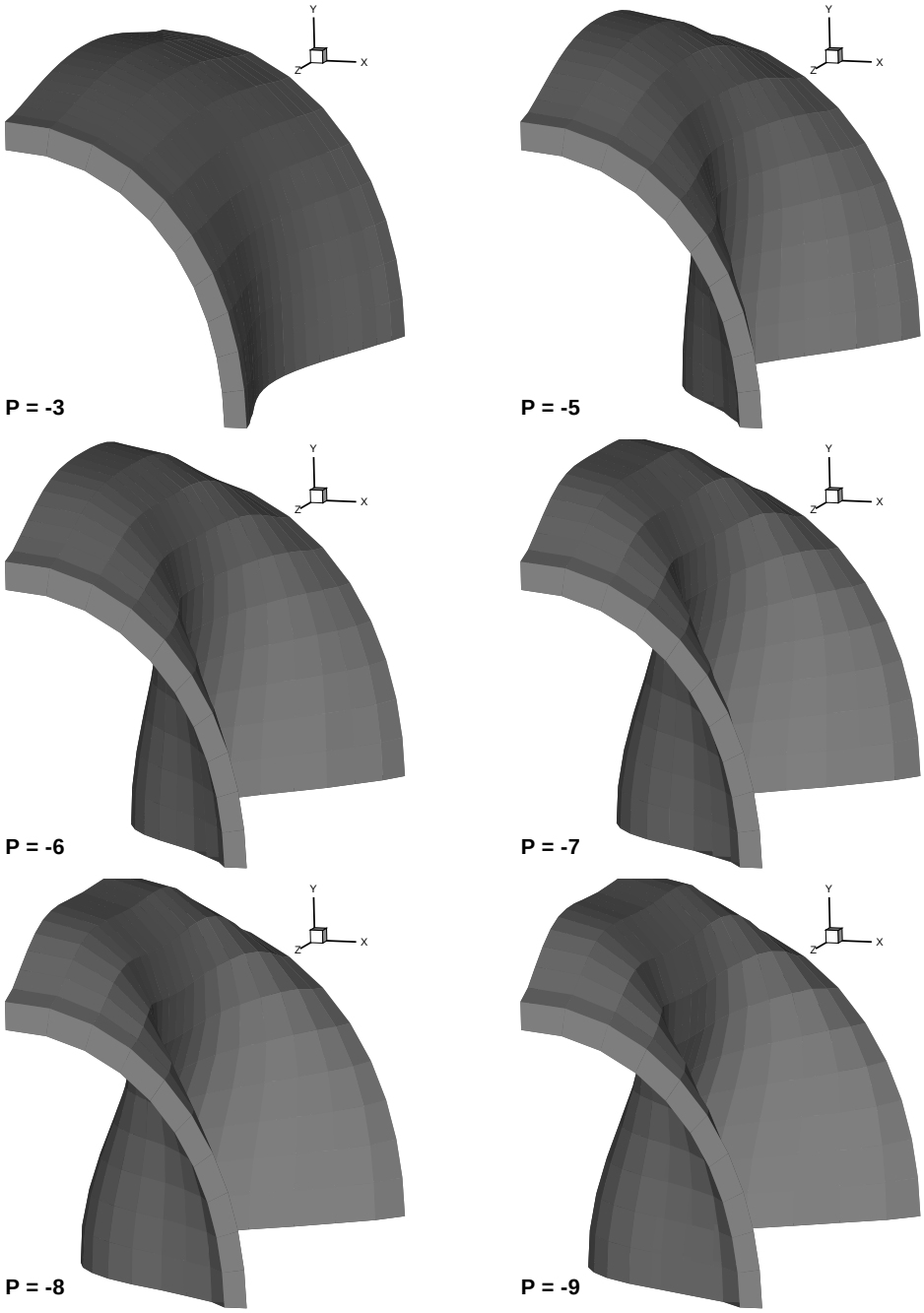

FIGURE 3.20: *The shape of the tube for various values of the dimensionless transmural pressure.* $L/D = 5$*, mesh:* $10 * 10 * 1$*. Because of symmetry only one quarter of a tube is shown.*

COUPLING FLOW / STRUCTURAL MODELS

CHAPTER 4

Biofluids are transported in deformable vessels, i.e. tubes. When the transmural pressure is negative, the vessel may collapse. In the case of collapse opposite walls come into contact with each other and the cross-sectional area of the vessel is reduced considerably. The dynamics of collapsible tubes depends on the coupling of the fluid mechanics (flow) and solid mechanics (deformation of the tube wall). An example of such fluid-structure interaction is the tube law, an empirical relation between transmural pressure and cross-sectional area for the case of a slender tube of constant cross-section subject to a constant transmural pressure. When large structural deformations are considered, three-dimensional calculations must be carried out. However, three-dimensional fluid-structure coupling, when transient flows in human lungs are considered, is too ambitious for the present study. Not only the difficulty of the model and its implementation, but also the computer resources needed are too excessive for such calculations. In this chapter, the three-dimensional deformation of the tube is coupled with a one-dimensional flow model. After a brief description of the numerical implementation of the coupling of the flow model and structural model, various cases of the flow through a flexible tube will be investigated to validate this approach of fluid-structure interaction.

4.1 Coupling: implementation

A brief description of the numerical implementation of the coupled model is presented here. The flow field is calculated for a given deformed tube wall by combining the equation of mass conservation with the Bernoulli equation. A Finite Element Method (FEM) is used to compute the tube wall deformation (see chapter 3). The flow model has as input the cross-sectional area as a function of the axial coordinate: $A(z), z\epsilon[0 \ldots L]$, where L is the length of the tube. The computed flow field, specifically the calculated axial distribution of the pressure, serves as an input to the structural model. The (internal) pressure $p(z)$ allows to calculate the transmural pressure (internal - external pressure) and thus the load applied on the tube wall. From an initial tube wall shape, an iterative process will lead to a solution of the tube wall shape and of the flow field.
For the flow domain and for the solid domain a different mesh is used. A finer mesh is used for the $1D$ flow model for a better accuracy. An interpolation procedure permits to handle the transfer of data between the two meshes.

4.1.1 Flow domain

A velocity is prescribed on the left-hand side of the tube ($z = 0$) as a boundary coundition. From the continuity equation, the velocity $w(z)$ is calculated at each cell of the flow domain mesh. The Bernoulli equation for incompressible flow (see chapter 2) is used to compute the pressure $p(z)$ since the flow is considered incompressible.

4.1.2 Structure domain

A Finite Element Method (FEM) is used to compute the deformation of a finite-thickness shell (see chapter 3). A load, depending on the inside pressure imposed by the flow, is applied on the external face of the shell in the normal direction. When convergence is obtained, i.e. the internal forces are in equilibrium with the external load, the new shape is found.
The structure mesh consists of 20-node, hexahedral elements. A mesh of an open part of a shell with $N_r * N_\theta * N_z$ elements, with $N_r = 1$, contains $5*N_\theta+3*(N_z+1)+2*(N_\theta+1)*N_z$ nodes, i.e. $3*[5 * N_\theta + 3)(N_z + 1) + 2 * (N_\theta + 1) * N_z]$ degrees of freedom. Since the tube wall is not expected to be compressed when the tube deforms the number of elements in the radial direction is taken as: $N_r = 1$. An example of a cylindrical hollow tube is shown in figure 4.1. Only one quarter of a shell is used for the calculation since a two-lobe (thus doubly symmetric) tube deformation is expected.

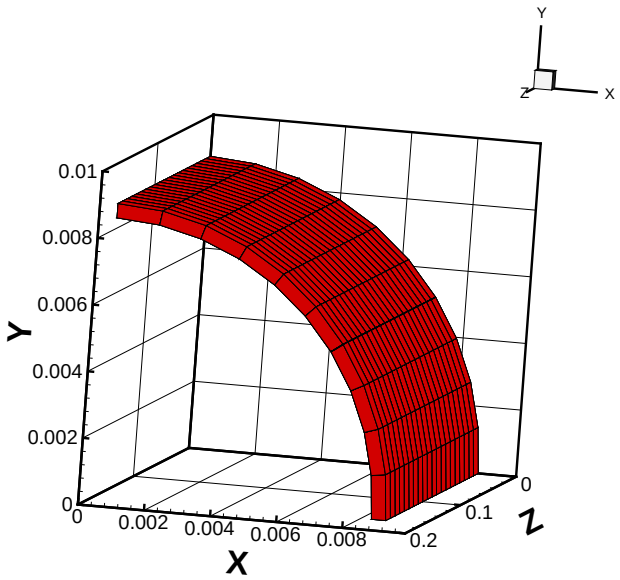

FIGURE 4.1: *Theoretical initial state of the tube, where the cross-sectional area is circular. Because of symmetry, only one quarter of the configuration is considered in the computations.* $N_r = 1$, $N_\theta = 10$, $N_z = 10$. *The number of* 20*-nodes elements* 100*, the number of nodes is* 803

Note that not all nodes used in the computations are plotted. Indeed, 20-node elements (see

figure 4.2) are not a standard in plotting programs. Therefore we split the elements into two, 8-node bricks, which leaves 8 nodes unplotted per elements (number 10, 12, 14, 16, 17, 18, 19, 20). Figure 4.2 also shows which nodes are plotted.

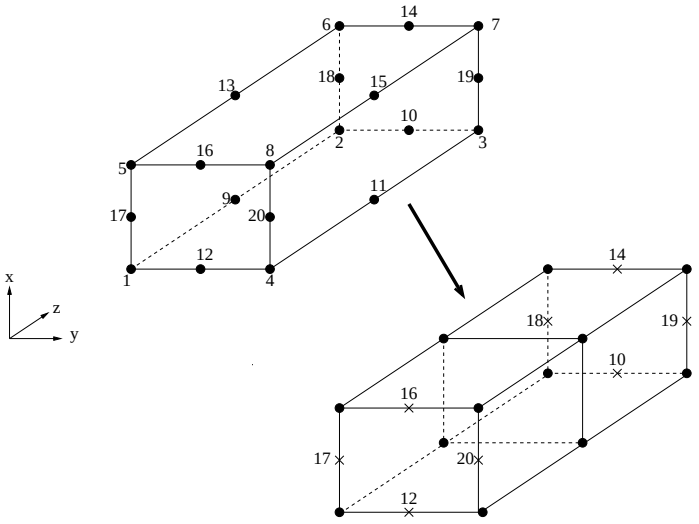

FIGURE 4.2: *In all mesh plots, the* 20*-node elements used in the computations are split into two* 8*-node bricks, leaving eight nodes (number* 10, 12, 14, 16, 17, 18, 19, 20*) unplotted.*

A perfectly circular-shaped hollow tube under uniform, inward load cannot collapse. To be able to collapse, the shape of a hollow tube must be non-circular. A solution often used is to convert the circular cross-section into an elliptical shape. This is illustrated in figure 4.3. In all calculations the circular cross-section has been replaced by an elliptical cross-section of the same cross-sectional area $\pi ab = \pi R^2$, where a and b are the semi-major and semi-minor semi-axis, respectively, and R is the tube cross-sectional radius. The semi-major and semi-minor axes are chosen as: $a = 1.1R$ and $b = 0.9R$, respectively. The tube aspect ratio $L/(2R)$ is preserved.

4.1.3 Scheme

An iterative process, alternating flow and structural computations, leads to the solution. The flow results give the input for the structural calculations through the internal pressure $p(z)$. The tube deformation provides the input for the next flow calculation through the new cross-sectional area $A(z)$. The Finite Element Method for the shape of the tube wall uses the numerical solution of the previous step as the initial guess for the next calculation. The area $A(z)$, calculated at each cross-section of the $3D$ mesh, is interpolated to the much finer mesh of the flow computation described below. The load applied on the external area of the shell must be calculated: at each cross-section of the $3D$ mesh, the transmural pressure (internal - external pressure) is converted into a normal force by calculating its area of application. The

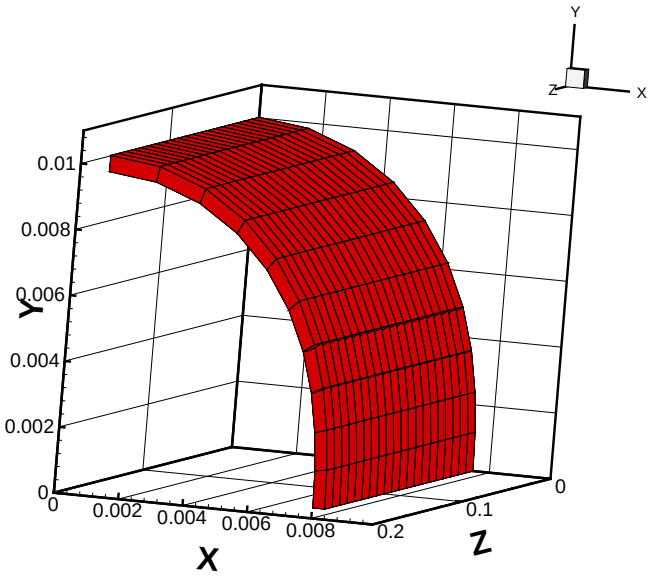

FIGURE 4.3: *Discretized initial state of the tube; the circular cross-section (figure 4.1) has been changed into an elliptical shape to allow the tube to collapse.*

fluid-structure coupling calculation is considered converged when:

$$\frac{(A^*)^k - (A^*)^{k-1}}{(A^*)^k} \leq \epsilon \tag{4.1}$$

where A^* is the throat area, k is the k^{th} iteration and ϵ is taken equal to 10^{-6}.
The scheme is summarized in figure 4.4.

interpolation solid mesh

The cross-sectional areas are calculated from the structure domain: at each cross-section an area $A(z)$ is calculated, that is used to compute the flow field. $A(z)$ is calculated using the trapezoidal rule, employing vertices at (x_i, y_i), (x_i, y_{i+1}), (x_{i+1}, y_i) and (x_{i+1}, y_{i+1}), where i and $i+1$ are two consecutive points:

$$A(z) = \sum_{i=1}^{N_\theta} \left(\frac{1}{2}(y_i + y_{i+1}) \right) (x_{i+1} - xi) \qquad i = 1..N_\theta \tag{4.2}$$

Since the fluid mesh is finer than the solid mesh (in the axial direction) these areas $A(z)$ are found by interpolation (see figure 4.5). Cubic Hermite polynomials are used for the interpolation on an equi-distant grid ([55]). The interpolant, continuous in function value, first and second derivative, does not pass precisely through the specified function values at the grid points. The piecewise cubic interpolant, with $\beta = (z - z_{i-1})/(z_i - z_{i-1}),\ \beta\epsilon[0,1]$, is defined as:

$$F(\beta) = l_i P_1(\beta) + l_{i+1} P_2(\beta) + l'_i Q_1(\beta) + l'_{i+1} Q_2(\beta) \tag{4.3}$$

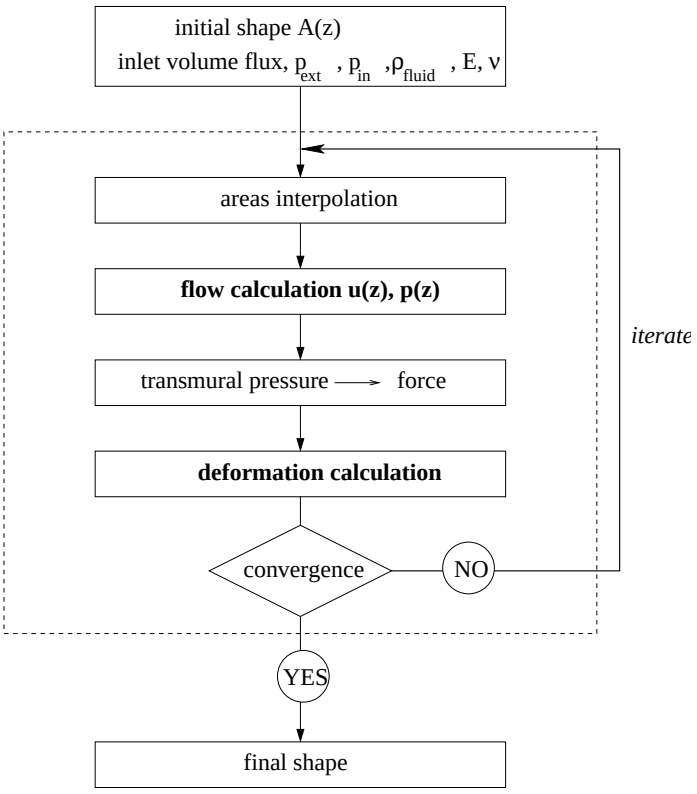

FIGURE 4.4: *Numerical scheme of the fluid-structure coupling.*

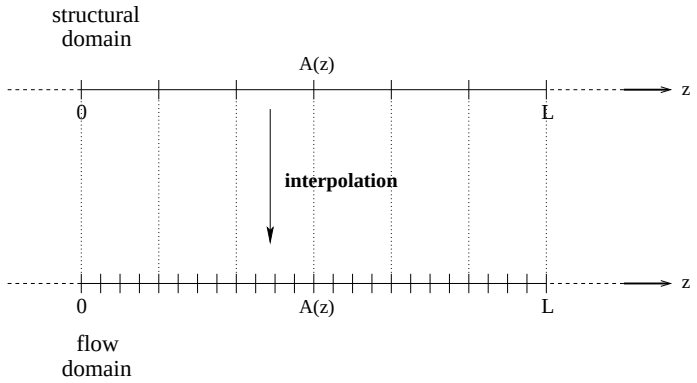

FIGURE 4.5: *Axial cells for the flow and the structural domain.*

with the following cubic Hermite polynomials for the functions $P_1(\beta), P_2(\beta), Q_1(\beta)$ and $Q_2(\beta)$:

$$P_1(\beta) \quad = \quad (1-\beta)^2(1+2\beta) \tag{4.4-a}$$

$$P_2(\beta) = 1 - P_1(\beta) \quad \text{(4.4-b)}$$
$$Q_1(\beta) = \beta(1-\beta)^2 \quad \text{(4.4-c)}$$
$$Q_2(\beta) = -\beta^2(1-\beta) \quad \text{(4.4-d)}$$

Interpolant 4.3 ensures for given $l_i, l'_i, l_{i+1}, l'_{i+1}$ continuity of the function value and first derivative of F across the nodal points. The interpolant is used to generate a discretization scheme. The parameters $l_i, l'_i, l_{i+1}, l'_{i+1}$ are depicted in figure 4.6.

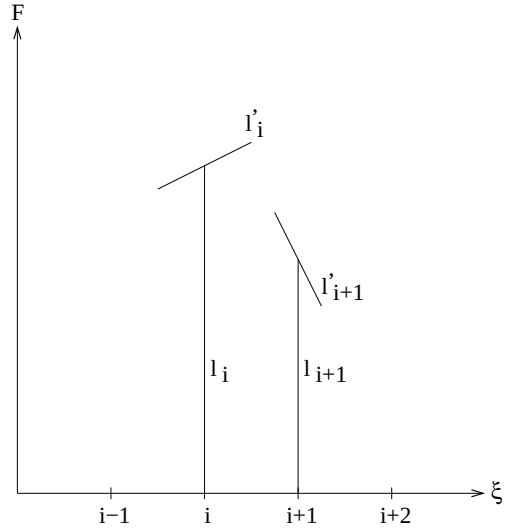

FIGURE 4.6: *Parameters used for the interpolation.*

Requiring continuity up to the second derivative of the function $F(\xi)$ across the nodes, assuming that the grid is uniform and choosing:

$$l'_i = \frac{1}{2} f_{i+1} - \frac{1}{2} f_{i-1} \quad (4.5)$$

results in:

$$l_i = \frac{1}{6} f_{i+1} + \frac{4}{6} f_i + \frac{1}{6} f_{i-1} \quad (4.6)$$

where f_i is the user specified function value at the point i, etcetera. At the edges of the computational domain, this scheme passes into the following form, valid for the left-hand side boundary:

$$l'_i = f_{i+1} - f_i \quad (4.7)$$

A similar relation is used for the right-hand side boundary.
Note that this interpolant has smoothing characteristics in that the function value at a node is replaced by a weighed averaged of the function value at the point considered and the function value at the two nearest neighbors.

4.2 Dimensionless parameters

In considering the flow through collapsible tubes the geometry is characterized by the following geometric characteristics:
- tube diameter $D = 2R$, with R the mean radius
- tube aspect ratio L/D
- tube thickness h/R
The material of the tube wall is elastic, characterized by:
- elasticity modulus E
- Poisson ration ν
The parameter that determines the elastic behavior of the tube wall under loading is:

$$K_p = \frac{E}{12(1-\nu^2)} \left(\frac{h}{R}\right)^3 \tag{4.8}$$

as we have employed already in previous chapters. In the case without flow we found that the tube problem is fully described by the dimensionless transmural pressure $P = (p - p_{ext})/K_p$.
In the case with flow we have in addition to the above listed quantities the inlet conditions:
- total pressure p_{tot}
- density ρ_0
- velocity w_0
so that, in incompressible flow, the inlet static pressure equals $p_0 = p_{tot} - 1/2\rho_0 w_0^2$. This leads to the relevant dimensionless parameter, a similarity parameter, for the case with flow:

$$k_p = \frac{K_p}{1/2\rho_0 w_0^2} \tag{4.9}$$

where the denominator is the dynamic pressure of the flow.
Finally we have the pressure outside the tube p_{ext} as quantity to be considered. It gives the external pressure coefficient as:

$$C_{p,ext} = \frac{p_{ext} - p_0}{1/2\rho_0 w_0^2} \tag{4.10}$$

The solution of the problem of the flow through a collapsible tube is fully described by finding the shape of the tube, e.g. the ratio of the local cross-sectional area as function of z/L, nondimensionalized by the initial cross-sectional area A_0, in terms of three parameters: k_p, $C_{p,ext}$ and L/D. Therefore:

$$\alpha(z/L) = A(z/L)/A_0 = F(z/L; k_p, L/D, C_{p,ext}) \tag{4.11}$$

Note that α, for the finite-length tubes considered here, is a function of z/L.
The structural equations are solved on some mesh resulting in a value of α. Given this value of α, the velocity and the pressure coefficient follow as:

$$\frac{w}{w_0} = \frac{1}{\alpha} \tag{4.12-a}$$

$$C_p = \frac{p - p_0}{1/2\rho_0 w_0^2} = 1 - \frac{1}{\alpha^2} \tag{4.12-b}$$

respectively, where both w and C_p are a function of z/L.
Here we used the continuity equation and the Bernoulli relation for incompressible flow. The dimensionless transmural pressure P is then:

$$P(\alpha) = \frac{p - p_{ext}}{K_p} = \frac{1}{k_p}\left(1 - \frac{1}{\alpha^2} - C_{p,ext}\right) \tag{4.13}$$

where P is a function of z/L through α.

In figure 4.7 the dimensionless transmural pressure given above is plotted for the case $C_{p,ext} = 1$, which corresponds to specifying $p_{ext} = p_{tot}$, as a function of the dimensionless area ratio α. Figure 4.7 shows that for given α the path taken through this plot depends on the way the

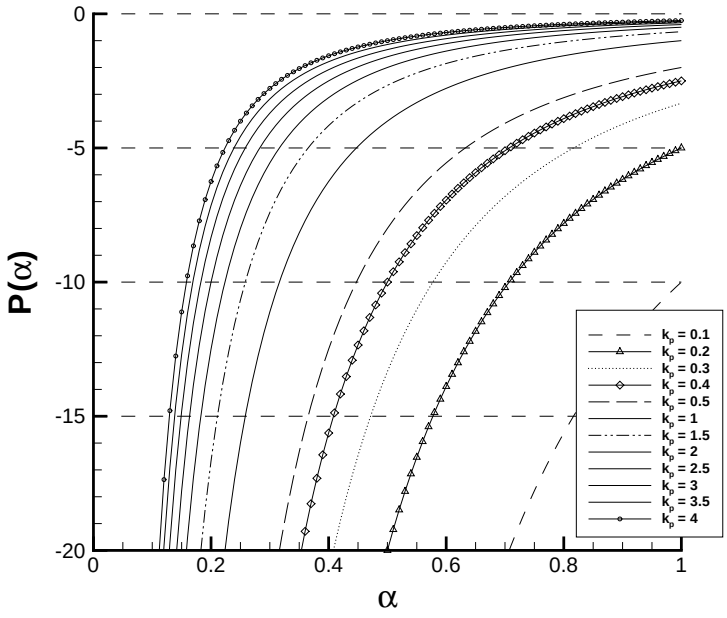

FIGURE 4.7: *Dimensionless transmural pressure as function of the dimensionless tube cross-sectional area for constant k_p. $C_{p,ext} = 1$. The values of k_p are 0.1, 0.2, 0.3, 0.4, 0.5, 1.0, 1.5, 2.0, 2.5, 3.0. 3.5 and 4.0. The curve passing through (1,-10) is the curve for the lowest value of k_p. The curves to the left of this curve are curves for higher values of k_p.*

tube is charged. For the case for which K_p (tube material properties) is kept constant and the calculation is started for a low value of w_0, that subsequently is increased, we start at α near 1 and a high value of k_p, i.e. low absolute value of P. For increasing values of w_0, α will decrease, so that k_p decreases, so that P becomes more and more negative. For the case w_0 is taken constant and the material properties are varied, we start at some value of α and

the corresponding value of $P(\alpha)$. Then increasing the Young's elasticity modulus E (or the Poisson ratio ν), i.e. making the tube stiffer, will result in an increasing k_p, so that a value to the left of the first point will be found.
Note that in the remainder of this thesis we often refer to α as the ratio of the throat cross-sectional area A^* and the initial cross-sectional area A_0.

4.3 The solution for the tube with flow

The flow is considered inviscid, incompressible and quasi-$1D$. The calculations are conducted using the three-dimensional FEM structural method coupled to the (one-dimensional) Bernoulli equation. Since the flow is considered inviscid and the tube is clamped at both ends, the tube remains symmetric with respect to the throat of the tube, which is halfway the tube. We assume that in the cross-section there are two planes of symmetry so that in the finite-element computations, with the appropriate symmetry conditions, we only need to consider one quarter of the tube.
A diagram of the process is shown in figure 4.8. A velocity w_0 is applied at the inlet to

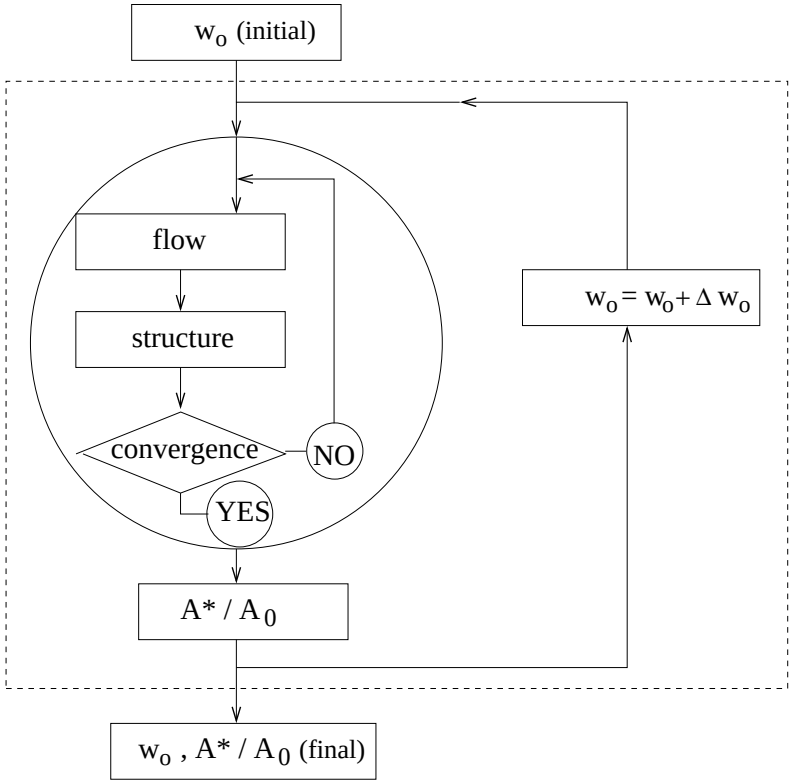

FIGURE 4.8: *Sketch of the flow / structure calculations.*

induce the flow in the undeformed, i.e. straight, tube. Then, the deformation of the tube is

computed using the result of the flow computation, specifically the static pressure inside the tube (the external load applied on the surface of the tube is calculated from the transmural (internal - external) pressure). Since the cross-sectional area along the tube has changed, the flow must be recalculated with the new tube shape. This process is repeated until convergence is reached, i.e. the flow and the tube's shape are in balance and an equilibrium shape is obtained. When the equilibrium shape is reached for a given flow, the inlet velocity is increased in order to induce a stronger deformation of the tube.

The flow conditions p_{tot}, p_{ext}, ρ_0, and w_0, the tube data D, L/D, h/R, E, and ν as well as the number of elements and the number of nodes of the mesh used are given in table 1. Included in the table are the three relevant dimensionless parameters: k_p, L/D and $C_{p,ext}$. The tube chosen has an aspect ratio of $L/D = 5$, which is somewhat longer than the tubes in most lung models, but was used earlier for the case without flow and serves here as a test case.

p_{tot} (Pa)	101000	D=2R (m)	0.002	E (Pa)	$1.0 * 10^4$
p_{ext} (Pa)	101000	L/D (-)	5	ν (-)	0.3
ρ_0 (kg/m^3)	1.0	h/R (-)	0.1		
w_0 (m/s)	varies				
$C_{p,ext}$ (-)	1.0	k_p (-)	varies	K_p (Pa)	0.9158
mesh	10*10*1	number of nodes	803		

Table 1: *Data for the tube with flow: inlet pressure p_{tot}, external pressure p_{ext}, inlet density ρ_0, inlet velocity w_0, diameter $D = 2R$, aspect ratio L/D, thickness h/R, Young modulus E and Poisson ratio ν; number of elements and number of nodes of the mesh used.*

The solution, here studied in the form of $\alpha = A^*/A_0$, with A^* the throat cross-section, is a function of three dimensionless numbers: k_p, L/D and $C_{p,ext}$. In the present study the external pressure is taken equal to the total pressure of the flow, which yields $C_{p,ext} = 1$. So, with L/D fixed, α is a function of k_p only.
The results are obtained by starting for the case with a value of k_p for which the deformation is small and then decreasing k_p stepwise until α decreases so rapidly that the procedure fails to converge. Initially a velocity $w_0 = 1\ m/s$ is imposed at the inlet. This corresponds to a value of k_p of 1.835. When a converged solution is reached the inlet velocity is increased with $0.1\ m/s$ to invoke a more extensive deformation, etc.
Figure 4.9 shows the results of the present method. The dimensionless throat area $\alpha = A^*/A_0$ is plotted versus $k_p = E(h/R)^3/(12 * (1 - \nu^2))/(1/2\rho_0 w_0^2)$. For $w_0 = 1\ m/s$ six iterations were required to find the converged solution. The solution shows that with increasing velocity the tube first does not deform very much, i.e. k_p has to decrease from 1.8 to around 0.6 before α starts to decrease rapidly. This initial behaviour is similar to the behavior we found for the case without flow, i.e. the deformation of the tube is so small that the velocity and therewith the pressure is nearly uniform in the tube. At $w_0 = 1\ m/s$, $P = (p_0 - p_{ext})/K_p = -0.55$, a value that is relevant near the clamped edges. At somewhat higher velocity, here $w_0 = 2\ m/s$, the pressure difference is already larger, giving P a value of -2.2, inducing already larger deformations. As soon as the deformation becomes appreciable the flow velocity in the throat will increase to values considerably exceeding w_0, leading to locally lower pres-

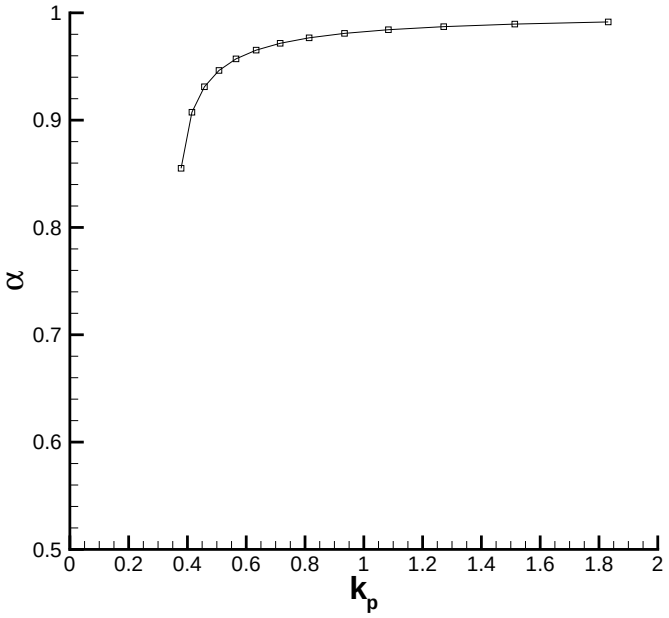

FIGURE 4.9: *The tube with flow: the dimensionless throat area* $\alpha = A^*/A_0$ *is plotted versus* k_p. $C_{p,ext} = 1$, $L/D = 5$*; the mesh contains* $10 * 10 * 1$ *elements.*

sures, therefore higher loads, which leads to more deformation, etc. Therefore α decreases very rapidly once the deformation becomes appreciable. The "critical" value of k_p, the value of k_p for which collapse sets in, is equal to 0.38.

4.4 Mesh refinement

In this section the influence of the refinement of the mesh is investigated. The deformation of a tube is calculated for different meshes. The computations are conducted in a stepwise manner using the converged solution from the previous step as the initial guess for the next calculation. The initial inlet velocity is taken as $w_0 = 1\ m/s$. When an equilibrium of the shape of the deformed tube for the given boundary conditions is found the inlet velocity is increased by $0.1\ m/s$ and the solution for a somewhat lower value of k_p is started.
The inlet flow conditions, the tube geometry and elasticity as well as the mesh data are given in table 2.

p_{tot} (Pa)	101000	D=2R (m)	0.002	E (Pa)	$1.0 * 10^4$
p_{ext} (Pa)	101000	L/D (-)	5	ν (-)	0.3
ρ_0 (kg/m^3)	1.0	h/R (-)	0.1		
w_0 (m/s)	varies				
$C_{p,ext}$ (-)	1.0	k_p (-)	varies	K_p (Pa)	0.9158
mesh	varies	number of nodes	varies		

Table 2: *Data for the case "Mesh refinement": inlet pressure p_{tot}, external pressure p_{ext}, inlet density ρ_0, inlet velocity w_0, diameter $D = 2R$, aspect ratio L/D, thickness h/R, Young modulus E and Poisson ratio ν; number of elements and number of nodes of the mesh used.*

In figure 4.10, the results for different meshes are presented. The non-dimensional throat area is plotted as a function of k_p. Calculations are performed with three different meshes: $10*10*1$, $20*20*1$ and $40*40*1$, 20-node elements, corresponding to 803, 3003 and 11603 nodes, respectively. The value of the deformation A^*/A_0 obtained from a Richardson's extrapolation, corresponding to an "infinite" refinement discussed below, has been added.

Clearly, the mesh refinement has an effect on the tube's deformation. For a given k_p the deformation is larger for a finer mesh. However, for a given k_p the computational error decreases with increasing mesh point density and in the end, for an infinitely fine mesh, the grid-converged solution will be obtained.

The (averaged) mesh size can be defined as:

$$h_{av} = (\Delta X \Delta Y \Delta Z)^{\frac{1}{3}} = \left(\frac{L_x L_y L_z}{N_x N_y N_z} \right)^{\frac{1}{3}} \tag{4.14}$$

with $L_x = h$, $L_y = \pi R/2$ and $L_z = L$ the dimensions in the radial, angular and axial directions and N_x, N_y and N_z the number of elements in the radial, angular and axial direction of the initial tube geometry, respectively. In figure 4.11 α is plotted as function of h_{av} for a number of k_p. It shows that, with decreasing h_{av}, α decreases quadratically, i.e. the deformation becomes larger with increasing mesh density.
The value of the deformation α for $h_{av} = 0$ is calculated from a Richardson type of extrapolation:

$$\alpha(h_{av}) = \alpha(0) + C h_{av}^p \tag{4.15}$$

where C is a constant and p the order of the method. The three unknown parameters are calculated from the results for the three meshes $10 * 10 * 1$, $20 * 20 * 1$ and $40 * 40 * 1$ and are given for different k_p in table 3. It follows from these results that the method appears to be in between first-order and second-order accurate.

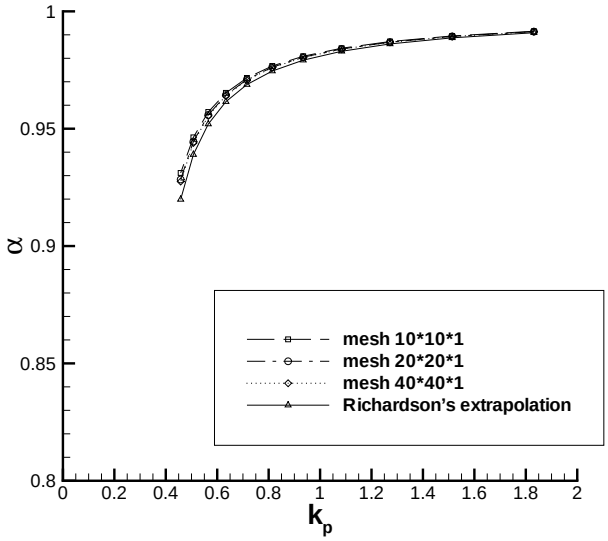

FIGURE 4.10: *The non-dimensional throat area is plotted versus k_p for three different meshes ($10*10*1$, $20*20*1$, $40*40*1$). The "exact" value, i.e. the value of the dimensionless throat area for h_{av} is also plotted. $C_{p,ext} = 1$, $L/D = 5$.*

k_p	$\alpha(0)$ [-]	C [-]	p [-]
1.8315	0.9909	0.0153	1.42298
1.5136	0.9887	0.0194	1.42292
1.2719	0.9861	0.0246	1.42291
1.0837	0.9830	0.0314	1.42292
0.9344	0.9792	0.0402	1.42298
0.8140	0.9746	0.0520	1.42297
0.7154	0.9688	0.0680	1.42300
0.6337	0.9615	0.0906	1.42303
0.5653	0.9520	0.1240	1.42305
0.5073	0.9390	0.1771	1.42314
0.4578	0.9199	0.2731	1.42351

Table 3: *Parameters p, C and $A^*(0)/A_0$ for different values of k_p. $C_{p,ext} = 1$, $L/D = 5$.*

4.5 Influence of the Poisson ratio

The Poisson ratio relates the deformation in axial direction to the deformation in circumferential and tangential directions. In order to investigate the influence of the Poisson ratio ν on the results calculations have been carried out for a number of values of ν for a tube with $L/D = 5$.

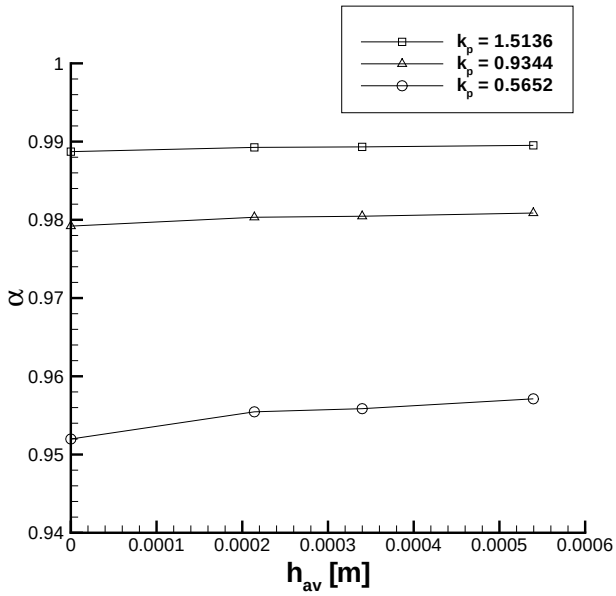

FIGURE 4.11: *α is plotted versus the element size h_{av} for different values of k_p. $C_{p,ext} = 1$, $L/D = 5$.*

The inlet flow conditions, the tube geometry and elasticity as well as the mesh data are given in table 4.

p_{tot} (Pa)	101000	D=2R (m)	0.002	E (Pa)	$1.0 * 10^4$
p_{ext} (Pa)	101000	L/D (-)	5	ν (-)	varies
ρ_0 (kg/m^3)	1	h/R (-)	0.1		
w_0 (m/s)	varies				
$C_{p,ext}$ (-)	1	k_p (-)	varies	K_p (Pa)	varies
mesh	$10 * 10 * 1$	number of nodes	803		

Table 4: *Data for the case "Influence of the Poisson ratio": inlet pressure p_{tot}, external pressure p_{ext}, inlet density ρ_0, inlet velocity w_0, diameter D, aspect ratio L/D, thickness h, Young modulus E, Poisson ratio ν; number of elements and number of nodes of the mesh used.*

The initial inlet velocity is $w_0 = 1.0\ m/s$. As an equilibrium of the shape of the tube is reached the inlet velocity is increased by $\Delta w_0 = 0.1\ m/s$. The calculations are conducted for three values of ν: $\nu = 0.0$, $\nu = 0.3$, and $\nu = 0.4$. The corresponding values of K_p are 0.8333, 0.9158, and 1.1905, respectively.
The dimensionless throat area as a function of k_p is presented in figure 4.12 for the three different Poisson ratios. Similarity of the problem implies that α depends on k_p, L/D and $C_{p,ext}$. Since the latter two parameters are not changed the three $\alpha = \alpha(k_p)$ plots should collapse onto the same curve. Indeed, it is observed that the results fall onto one curve, which

is a verification of the implementation of the method. A value of $\nu = 0.3$ is chosen in this thesis as this is a realistic value for elastic material like lung tissue, but through the similarity parameter k_p, the effect of changing the value of the Poisson ratio is easily assessed.

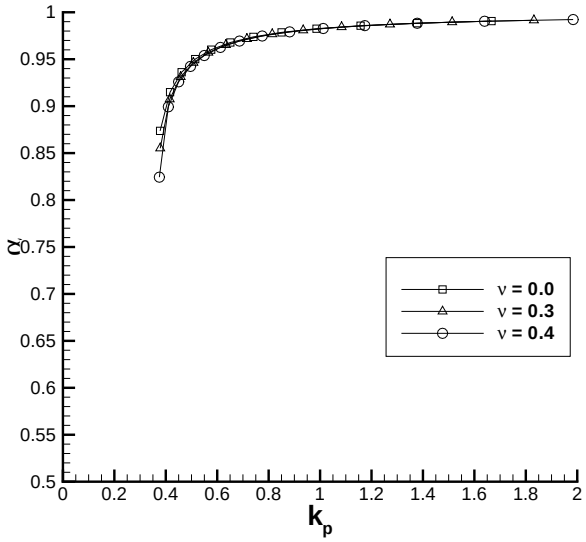

FIGURE 4.12: *Influence of the Poisson ratio:* $\nu = 0.0$, $\nu = 0.3$ *and* $\nu = 0.4$. *The dimensionless throat area* $\alpha = A^*/A_0$ *is plotted versus* k_p. $L/D = 5$, $C_{p,ext} = 1$*; mesh* $10 * 10 * 1$, 20*-node elements.*

4.6 Influence of wall elasticity

Calculations for different Young moduli E are presented here to investigate the influence of the elasticity on the collapse of an elastic hollow tube. The Young modulus is a characteristic of the elasticity of a material and has the dimension of pressure. It is defined as the slope of the stress-strain diagram in the linear elastic region:

$$\sigma = E\epsilon \tag{4.16}$$

with σ is the stress and ϵ is the strain.

For a given value of the flow velocities w_0 a higher value of E will result in a higher value of the similarity parameter k_p and therefore a smaller deformation than for the case of a lower value of E. However, again, because of the similarity of the problem the value of α for a specific value of k_p should be identical, i.e. the results for the three E's considered should collapse onto the same curve. The inlet flow conditions, the tube geometry and elasticity as

well as the mesh data are given in table 5. The values chosen for E are $1 * 10^4$, $5 * 10^4$ and $1 * 10^5$.

The initial inlet velocity is $w_0 = 1.0\ m/s$. Upon convergence of the solution for a given inlet velocity flow, the inlet velocity is increased by: $\Delta w_0 = 0.1\ m/s$.

p_{tot} (Pa)	101000	D=2R (m)	0.002	E (Pa)	varies
p_{ext} (Pa)	101000	L/D (-)	5.0	ν (-)	0.3
ρ_0 (kg/m^3)	1	h/R (-)	0.1		
w_0 (m/s)	varies				
$C_{p,ext}$ (-)	1	k_p (-)	varies	K_p (Pa)	varies
mesh	$10 * 10 * 1$	number of nodes	803		

Table 5: *Data for the case "Influence of wall elasticity": inlet pressure p_{tot}, external pressure p_{ext},inlet density ρ_0, inlet velocity w_0, diameter D, aspect ratio L/D, thickness h/R, Young modulus E, Poisson ratio ν, K_p and k_p; number of elements and number of nodes of the mesh used.*

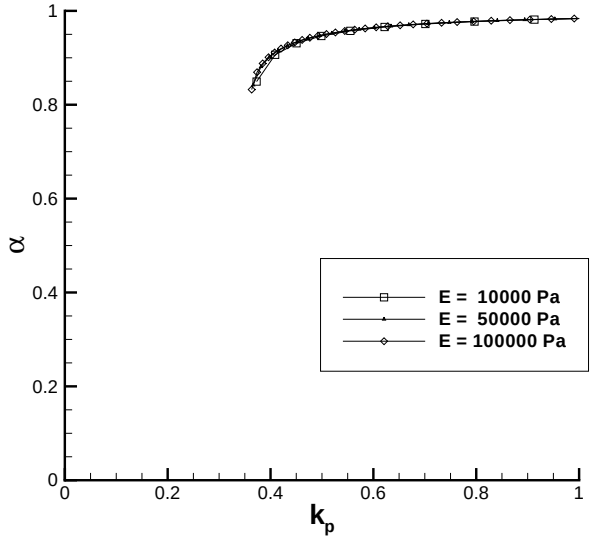

FIGURE 4.13: *Influence of the elasticity: $E = 1 * 10^4, 5 * 10^4, 1 * 10^5\ Pa$. The inlet velocity, that induces the flow, is increased step by step. The dimensionless throat area $\alpha = A^*/A_0$ is plotted versus k_p. $C_{p,ext} = 1$, $L/D = 5$; mesh $10 * 10 * 1$, corresponding to 803 nodes.*

The dimensionless throat area is plotted in figure 4.13 versus the similarity parameter $k_p =$

$K_p/(1/2\rho_0 w_0^2)$. The results confirm that all computed points are on one curve, verifying the implementation of the method.

4.7 Influence of length-diameter ratio

The geometry of a tube is defined by its length and its diameter, as well as by the thickness of the tube wall. For given conditions, i.e. the inlet flow rate, the external pressure and the mechanical properties E and ν of the tube wall, the solution depends on three similarity parameters, i.e. k_p, L/D and $C_{p,ext}$. Here we consider the influence of L/D. Since the tube is held fixed at its two extremities, it is expected that a short tube deforms less than a long tube at the same conditions.
To verify this hypothesis calculations have been conducted for different length-diameter ratios.

The inlet flow conditions, the tube geometry and elasticity as well as the mesh data are given in table 6.

p_{tot} (Pa)	101000	D=2R (m)	0.002	E (Pa)	$1.0 * 10^4$
p_{ext} (Pa)	101000	L/D (-)	varies	ν (-)	0.3
ρ_0 (kg/m^3)	1	h/R (-)	0.1		
w_0 (m/s)	varies				
$C_{p,ext}$ (-)	1	k_p (-)	varies	K_p (Pa)	0.9158
mesh	$10 * 10 * 1$	number of nodes	803		

Table 6: *Data for the case "Length-diameter ratio influence": inlet pressure p_{tot}, external pressure p_{ext}, inlet density ρ_0, inlet velocity w_0, diameter D, aspect ratio L/D, thickness h/R, Young modulus E, Poisson ratio ν; number of elements and number of nodes of the mesh used.*

An initial velocity $w(z = 0) = 1.0\ m/s$ is prescribed at the inlet. When the deformation of the tube is calculated the inlet velocity is augmented with $\Delta w = 0.1\ m/s$ and the new deformation is calculated.

The dimensionless area at the throat A^*/A_0 is plotted in figure 4.14 as a function of k_p for L/D in the range between $L/D = 1$ and $L/D = 10$.

The results show that indeed, for given k_p, the deformation increases with increasing L/D. Furthermore, it is observed that the set-on of collapse occurs earlier for the longer tube. We define the critical value of k_p as the last value for which the computational procedure converged. It is expected that this estimate of the value of k_p for which the tube collapses is reasonably accurate because of the asymptote-like behavior of $\alpha(k_p)$ near collapse. In chapter 1 the combination was considered of the tube law of Flaherty et al. ([12]), for an infinite tube with the quasi-onedimensional inviscid incompressible flow model. This resulted in the

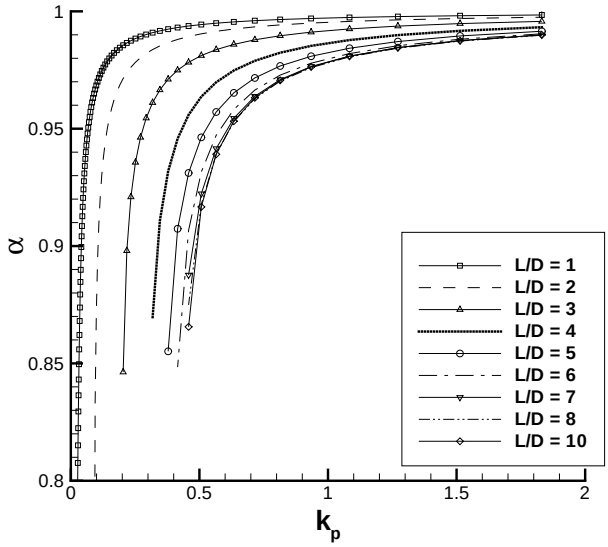

FIGURE 4.14: *The dimensionless area at the throat* $\alpha = A^*/A_0$ *as a function* k_p. $C_{p,ext} = 1$*; mesh* $10 * 10 * 1$*, corresponding to* 803 *nodes.*

solution given in equation 1.15. For the present case of $C_{p,ext} = 1$ this can be written as:

$$k_p = \frac{-1}{\alpha^2 - \alpha^{1/2}} \tag{4.17}$$

The minimum value of k_p that follows from this expression is found for $\alpha = (1/16)^{1/3} \approx 0.4$, for which $k_p = 2.1165$, much higher than the values found here for large L/D. This indicates the classical tube law is not suited for coupling with the flow.

In figure 4.15 the $k_{p,crit}$ is plotted versus L/D. This figure shows that for short tubes the $k_{p,crit}$ is low, i.e. a higher flow velocity is needed to have the tube collapse. For tubes with $L/D \in [1.5, 3.5]$ the critical value of k_p increases nearly linearly, i.e. the flow velocity for which collapse occurs decreases quadratically. It is found that within this range $k_{p,crit} \approx 0.1(L/D - 1)$. For much higher values of L/D, where a kind of two-dimensional situation is reached, the $k_{p,crit}$ reaches a constant level of about 0.45. For $L/D \in [1, 4]$ a more accurate interpolation formula than the linear one is:

$$k_{p,crit} = -0.0065(L/D)^4 + 0.0508(L/D)^3 - 0.1206(L/D)^2 + 0.1819(L/D) - 0.0876 \tag{4.18}$$

It is clear that for tubes with L/D smaller than 6 or 7 the length-diameter ratio has a major influence on the deformation of a collapsible tube. Lung airways have an L/D within this range. It is recalled that the present results are obtained using a structural model that restricts the deformation to one with two planes of symmetry, while also both ends of the tube are clamped. The latter might not be a correct representation of the situation occurring in the

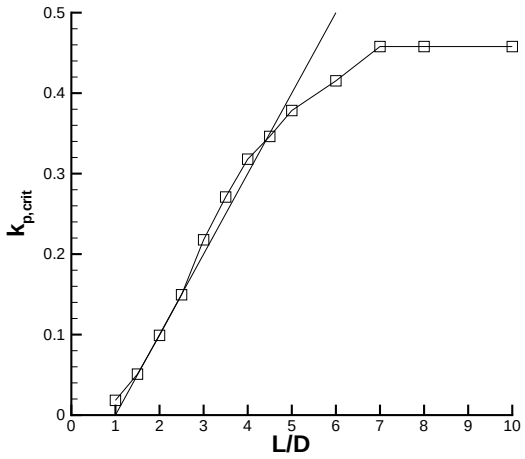

FIGURE 4.15: *$k_{p,crit}$ as a function of the length-diameter ratio's L/D for $C_{p,ext} = 1$; mesh $10 * 10 * 1$, corresponds to 803 nodes.*

human lung. Furthermore, the assumption that the flow is quasi-onedimensional might be adequate for small deformations, say for $\alpha \in [0.8, 1]$, but specifically for short tubes the flow will become three-dimensional.

FORCED EXPIRATION

CHAPTER 5

In this chapter the critical value of the elasticity of an airway, represented by the Young modulus E, is estimated for each generation of the Hansen-Ampaya lung model. To this aim we determine for the airway of each generation the critical value of the similarity parameter $k_p = E(h/R)^3/[12(1-\nu^2)]/(1/2\rho_0 w_0^2)$ and assume that for the conditions of forced expiration, which defines w_0, the airway may collapse. Choosing the airway wall thickness $h/R = 0.1$, ν equal to 0.3 and taking $C_{p,ext} = 1$ then determines the critical value of the elasticity modulus E.

5.1 Elasticity of lung airways

The geometry of a human lung has extensively been described in the literature. Length and diameter of each generation's tube and thus cross-sectional areas as well as surface areas and volumes are tabulated. Well-known models are for instance those of Weibel ([53]) and Hansen and Ampaya ([16]). However, data of the elasticity of lung airways as function of the generation number is an unknown. An exhaustive study of the elasticity characteristics of airways has not been conducted so far.

The following assumptions have to be made:

- The human lung is assumed to be symmetric. Here a scaled Hansen and Ampaya ([16]) lung model is employed.
- The tubes of each generation are identical, in that sense that they have the same geometry (length, diameter and thickness) as well as the same elasticity characteristics.
- The tube's thickness is assumed to remain constant during the deformation. The thickness is chosen as a thickness of $10\ \%$ of the radius of the tube, a reasonable value for lung airways.
- Elasticity of airway walls is supposed to be homogeneous.
- Elasticity of airway walls is supposed to be constant during the deformation.
- The length and undeformed diameter of a tube is supposed to be constant during calculations. In real life, an airway is stretched or expanded since tubes are attached to

each other and interact. Stretching and expanding of each tube happens constantly, as a spring in motion would do. However, we choose clamped-edge conditions.

- It is assumed that the external pressure p_{ext} is equal to the total pressure of the flow, i.e. when the flow velocity equals zero the transmural pressure equals zero. Furthermore, it is assumed that the total pressure in the lung is constant, equal to the atmospheric pressure.

5.1.1 Collapse of generation 2

During a forced expiration, complete collapse of at least one airway is expected to happen. Collapse happens at the maximum flow rate achieved. It is expected that the first generations collapse first. Not all the tubes of the specific generation collapse at the same time but one or more airways. The flow is redirected to the remaining open airways. The collapsed airways are able to reopen as soon as the air flows stops. Subsequently, airway collapse happens in the next generations, one after one, following this closing / reopening process.
For patients with lung disease (patients who suffer from asthma, COPD (Chronic Obstruction Pulmonary Disease) or other lung diseases), collapse of airways happens at a smaller flow rate than for a healthy person. Since lung disease will mostly be initiated deep in the lung thereby damaging airway structures, which influences their elasticity, airway collapse during forced expiration might take place deeper in the lung.

Since the collapse of a tube is expected to happen at the peak expiratory flow rate, only the first part of the forced expiration is considered (that is the part where the expiratory flow rate increases from zero to its maximum). At the maximum flow rate, collapse must happen.
Calculations with a tube of generation 2 are performed. This tube with an L/D of 2.29 is supposed to collapse at the maximum flow rate relevant for a healthy lung. To simulate the increasing flow rate during a forced expiration of a healthy person (see figure 5.1), the inlet velocity ranges from 0 to $46.3\ m/s$, increasing linearly.
The inlet flow conditions, the tube geometry and elasticity as well as the mesh data are given in table 1.

p_{tot} (Pa)	101000	D=2R (m)	0.0083	E (Pa)	$1.27 * 10^6$
p_{ext} (Pa)	101000	L/D (-)	2.29	ν (-)	0.3
ρ_0 (kg/m^3)	1	h/R (-)	0.1		
w_0 (m/s)	varies				
$C_{p,ext}$ (-)	1	k_p (-)	varies	K_p (Pa)	116.3
mesh	$10 * 10 * 1$	number of nodes	803		

Table 1: *Data for the calculation of the deformation of generation 2: inlet pressure p_{tot}, external pressure p_{ext}, inlet density ρ_0, inlet velocity w_0, diameter D, aspect ratio L/D, thickness h/R, Young modulus E, Poisson ratio ν, K_p and k_p; number of elements and number of nodes of the mesh used.*

It is assumed that the forced expiration is a dynamically slow process. This implies that a quasi-steady approach can be followed. The initial inlet velocity is $w_0 = 1\ m/s$. Upon

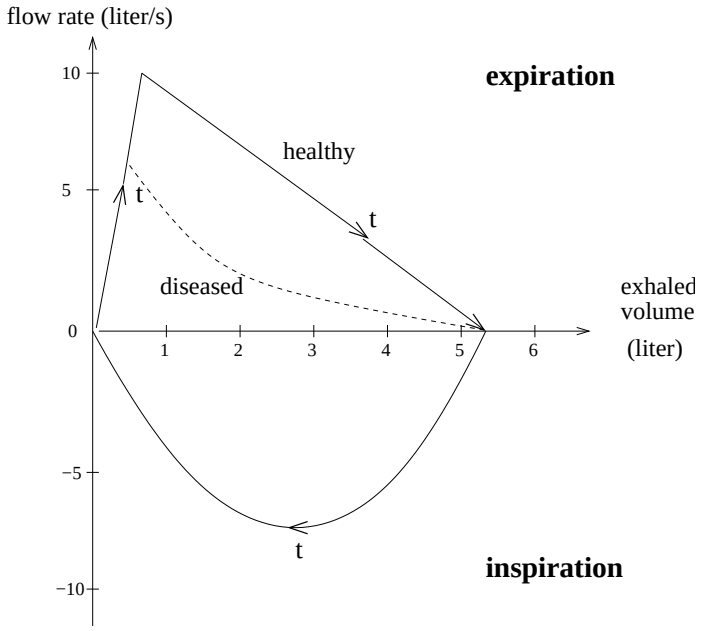

FIGURE 5.1: *Flow-volume curve: adult male (*30 *years,* $1.83\ m$*).*

reaching equilibrium iteratively, the inlet velocity is increased with:$\Delta w_0 = 1\ m/s$. The numerical calculations are stopped as the inlet velocity is $w_{0,max} = 46\ m/s$ or as the solution procedure diverges.

The results of the deformation calculations are presented in figure 5.2. For a number of inlet velocities the dimensionless throat area of the deformed tube is shown as function of the dimensionless similarity parameter $k_p = K_p/(0.5\rho_0 w_0^2)$. It shows that as the inlet velocity becomes high the deformation increases rapidly, decreasing the value of α. The solution procedure failed to converge for k_p smaller than a value of 0.126. This value corresponds to the value that can be found through interpolation from figure 4.15.

The axial distribution of the velocity $w(z)/w_0$ as well as the area $A(z)/A_0$ and the pressure $Cp(z)$ are plotted in figure 5.3 for various values of w_0. Figure 5.3 shows that up to $w_0 \simeq 40$ m/s the velocity, pressure and cross-sectional area remain fairly constant. For higher inlet velocities the cross-sectional area starts to decrease rapidly enforced by the rapidly dropping pressure in the middle of the tube. Note that even at the highest inlet velocity the speed of the flow is much lower than the speed of sound, indicating that compressibility effects will be small or restricted to the final stage of the collapse. Thus, deformation larger than around 20% could not be obtained, indicating that a complete collapse of the tube occurs as soon as the deformation reaches such level of deformation.

5.1.2 Elasticity of lung generations

In chapter 4 the critical value of the similarity parameter k_p has been obtained as function of L/D for $C_{p,ext} = 1$, see figure 4.15. Here we utilize this result to estimate the elasticity

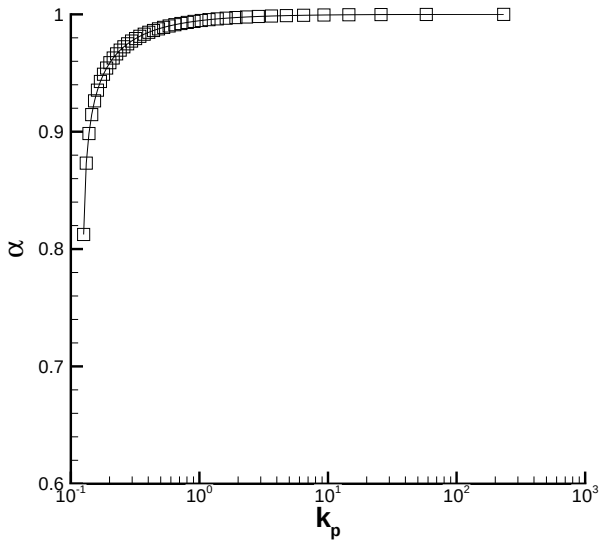

FIGURE 5.2: *The maximum deformation of a tube of generation* 2*, represented by the dimensionless throat area* $\alpha = A^*/A_0$*, for different* $k_p = \frac{E}{12(1-\nu^2)}\left(\frac{h}{R}\right)^3 \frac{1}{0.5\rho_0 w_0^2}$*.* $C_{p,ext} = 1$*,* $L/D = 2.29$*; mesh* $10 * 10 * 1$*,* 803 *nodes. Complete collapse occurs at* $k_p \approx 0.126$*.*

modulus of the airway walls of the lung defined by Hansen-Ampaya.

Hansen-Ampaya's geometrical data of each tube of generations 2 to 12, i.e. the length L and the diameter D are given together with the peak inlet velocity w_0 (the velocity corresponding to the maximum expiratory flow) in table 2. Generations 0 and 1 are not expected to collapse since these airways are too stiff due to cartilage reinforcements. Therefore these generations are not considered. The length-diameter ratio L/D is also specified since it determines the critical value of k_p. The thickness of the tube wall is taken, as before, as $10\ \%$ of the mean radius of the tube, while $\nu = 0.3$ and $\rho_0 = 1\ kg/m^3$.
In order to estimate E, or at least to find a lower limit for E, we assume that at the end of the forced expiration, i.e. an outflow of $10\ liters/s$, the airway is close to collapse. For the estimate we need the geometrical data of the lung. The value of $k_{p,crit}$ is obtained from figure 4.15 by interpolation, which then determines E_{crit}. The results are presented in table 3.

Figure 5.4 shows the distribution of $k_{p,crit}$ in the lung. It indicates a more or less gradual variation of this quantity, with $k_{p,crit}$ increasing with generation number until a maximum is reached near generation number 10. The value for generation number 3 with a low value of L/D is an outlyer. Included in figure 5.4 is the critical value of k_p we found for long tubes. We consider this value as a possible maximum value of $k_{p,crit}$, possibly approached closer in case the condition at the ends of the tubes (now clamped) are represented more accurately.
Figure 5.5 shows the corresponding critical values of the Young elasticity modulus E. It

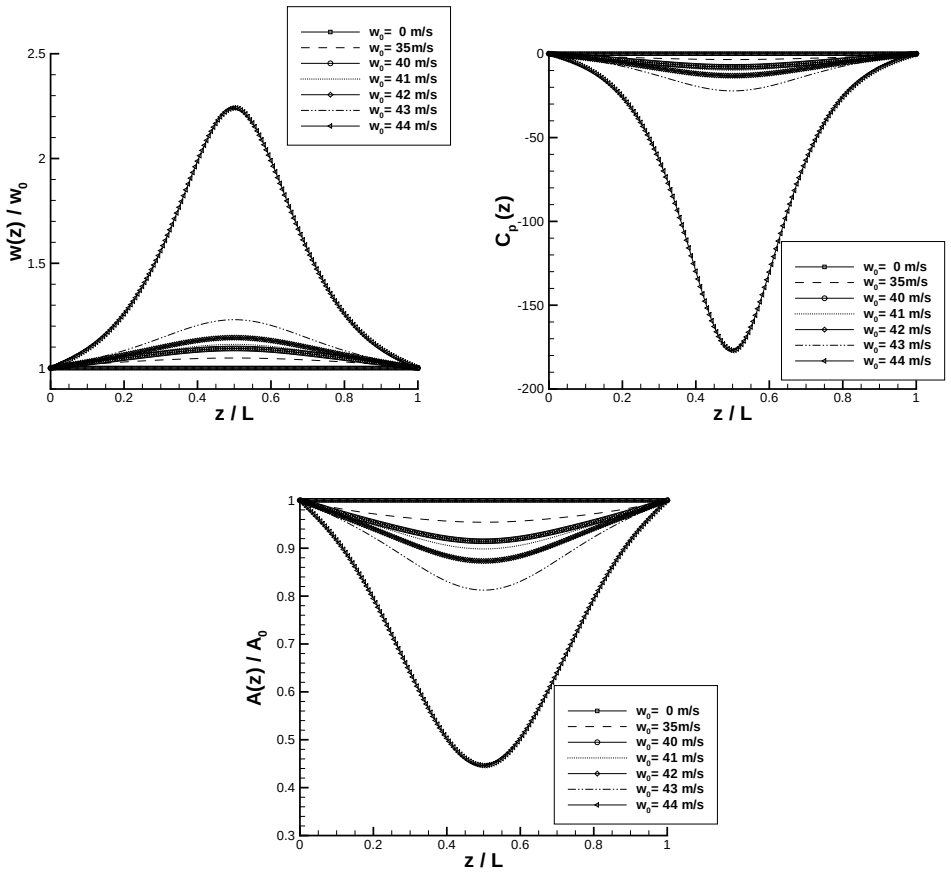

FIGURE 5.3: *Distribution of the velocity in a tube of generation number* 2*: the velocity* $w(z)/w_0$*, of the area* $A(z)/A_0$ *and of the pressure coefficient* $C_p(z)$ *are presented as function of the axial coordinate* z/L *for different inlet velocities up to* $w_0 = 44\ m/s$*.* $C_{p,ext} = 1$*,* $L/D = 2.29$*; mesh* $10 * 10 * 1,803$ *nodes.*

shows that the estimate obtained for the lower bound of the Young elasticity modulus behaves monotically for generation 4 to 12, decreasing from a value around $2.5 * 10^6$ for generation 4 to around $2.5 * 10^4$ for generation 12. Generation 2 and 3 show a different behaviour with values of E between 10^6 and $1.5 * 10^6$. Specifically generation 3 is an outlyer. Since E_{crit} is proportional to $k_{p,crit} w_0^2$, we note that the lower value of $k_{p,crit}$, because of the low value of L/D is not compensated by the higher value of w_0, see table 3. This leads to a low value of the allowable lower limit of E, lower than that for generation 2.
Also included in figure 5.5 is the value of E that follows from the $k_{p,crit}$ for tubes with $L/D \gg 1$, i.e. $k_{p,crit} = 0.45$. In that case, $E_{crit,L/D\gg1} = 0.45\ 1/2\rho_0 w_0^2 12(1 - \nu^2)/(h/R)^3$, which is proportional to w_0^2 only. Now generation 3 has the highest value of the lower limit of E.

g	L [m]	D [m]	L/D [-]	w_0 [m/s]
0	0.1200	0.01800	6.67	39.37
1	0.0476	0.01220	3.90	42.14
2	0.0190	0.00830	2.29	46.27
3	0.0067	0.00496	1.35	64.94
4	0.0112	0.00398	2.81	50.25
5	0.0095	0.00310	3.06	41.49
6	0.0080	0.00248	3.23	32.36
7	0.0067	0.00204	3.28	24.04
8	0.0057	0.00165	3.45	18.35
9	0.0048	0.00136	3.53	13.39
10	0.0041	0.00115	3.57	9.43
11	0.0031	0.00096	3.23	6.67
12	0.0027	0.00084	3.21	4.41

Table 2: *Data for tubes of generations $2-12$ (from Hansen-Ampaya's lung model): length L, diameter D and length-diameter ratio L/D and inlet velocity w_0 for the case of forced expiration ($10\ liters/s$).*

g	$k_{p,crit}$ [-]	E_{crit} [Pa]	$E_{crit}(L/D \gg 1)$ [Pa]
2	0.1278	$1.49 * 10^6$	$5.26 * 10^6$
3	0.0416	$9.57 * 10^5$	$1.04 * 10^7$
4	0.1932	$2.66 * 10^6$	$6.20 * 10^6$
5	0.2254	$2.12 * 10^6$	$4.23 * 10^6$
6	0.2461	$1.41 * 10^6$	$2.57 * 10^6$
7	0.2519	$7.95 * 10^5$	$1.42 * 10^6$
8	0.2697	$4.96 * 10^5$	$8.27 * 10^5$
9	0.2770	$2.71 * 10^5$	$4.41 * 10^5$
10	0.2803	$1.36 * 10^5$	$2.18 * 10^5$
11	0.2461	$5.98 * 10^4$	$1.09 * 10^5$
12	0.2438	$2.59 * 10^4$	$4.78 * 10^4$

Table 3: *The critical value of $k_p = \frac{E}{12(1-\nu^2)} \left(\frac{h}{R}\right)^3 \frac{1}{0.5\rho_0 w_0^2}$, where E is the Young modulus, ν is the Poisson ratio, h and R are the thickness and the radius of the tube, respectively, for generation 2 to 12. Listed id $E_{crit} = k_{p,crit} 12(1-\nu^2) 1/2 \rho_0 w_0^2/(h/R)^3$ for $\nu = 0.3$, $\rho_0 = 1\ kg/m^3$, $h/R = 0.1$ and w_0 given in table 2.*

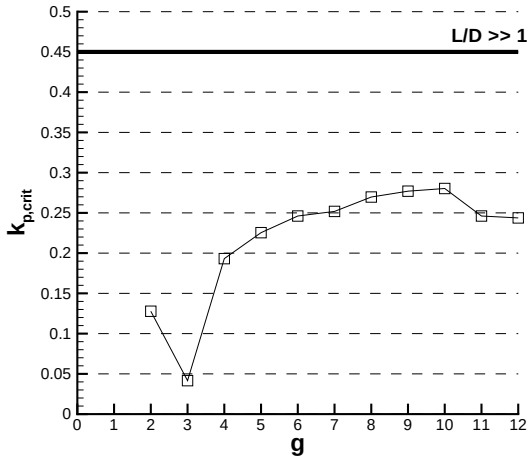

FIGURE 5.4: *Critical value of k_p for generations 2 to 12. $C_{p,ext} = 1$. Included in the figure is the critical value for L/D very large.*

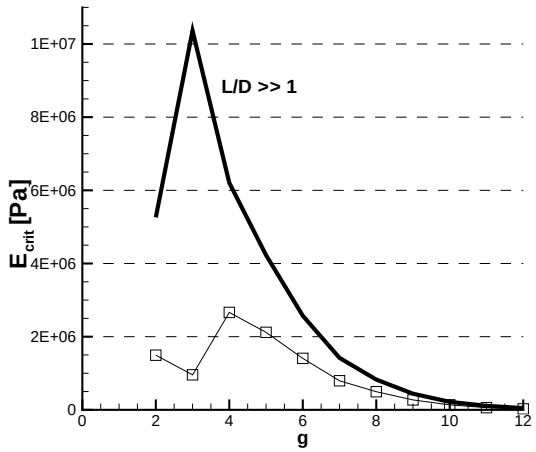

FIGURE 5.5: *Critical value of elasticity modulus E for generations 2 to 12. $C_{p,ext} = 1$. Included in the figure is the critical value for L/D very large.*

CONCLUDING REMARKS

6 CHAPTER

The deformation of a collapsible tube conveying air has been studied. The airflow in a collapsible tube decreases the pressure inside the tube. Since the external pressure is kept constant the transmural pressure (inside pressure minus outside pressure) is negative. Therefore, the transmural pressure acts like an inward, normal force distribution applied on the tube wall, yielding a deformation that reduces the cross-sectional area of the tube. Under certain circumstances, i.e. a large inlet flow rate and/or a low elasticity of the wall, a complete collapse of the tube occurs. This because of the self-enforcing mechanism that the decreasing cross-sectional area causes a further decrease in transmural pressure. This fluid-structure interaction phenomenon arises in a human lung. During a forced expiration some airways collapse completely.
The numerical method developed in this research is capable of simulating the onset of collapse due to the flow of air. The present numerical method shows that for reductions in cross-sectional area larger than around 20 % the decrease in cross-sectional area with transmural pressure is so fast that the computational procedure diverges, indicating the emergence of complete collapse.

The lung is often modeled as a system of branching tubes. The geometry of each tube is defined by its length L and its diameter D. The tubes can be considered as short since in the lung the length-diameter ratio L/D ranges from 1.5 to 4.0. This implies that in the lung tubes the flow cannot be considered fully developed, as has been verified in this research employing the commercial CFD software Star-CD.

A Finite Element Method (FEM) model has been developed to describe the deformation of a tube under a surface load. The structured mesh used for the calculation employs 20-node, hexahedral elements, allowing a quadratic description of the displacements within an element. The mechanical properties of the elastic material, that define its elasticity, are represented by the Young modulus $E\ [Pa]$ and by the Poisson ratio $\nu\ [-]$. Results of calculations for a number of $3D$ cases have been compared with the results found with the commercial software ANSYS. A good agreement has been found.
For the case of a tube subjected to a constant transmural pressure (no flow), results have been obtained for tubes of various L/D. Results of the method have been compared with results of ANSYS for the (2D) case of an infinite tube showing a good correlation as L/D becomes 10 and larger. The results of empirical relations (tube law) for the infinite tube are quite different from the results computed by the present method and the ones obtained from ANSYS, indi-

cating the inadequacy of these empirical relations.

The flow in the (deformed) tube was modeled as an inviscid, quasi-onedimensional flow. By comparing results of an Euler method for non-isentropic flow, a method for isentropic compressible flow and a method for incompressible flow, it has been shown that the incompressible flow method gives adequate results for the flow in deformed lung tubes. This implies that compressibility effects can be neglected.
In the later phases of a collapse the flow will no longer be quasi-onedimensional, nor inviscid. In future research the flow in strongly deformed collapsing tubes should be considered employing a method for three-dimensional viscous flow. In future research also the effects of the tube branching on the flow in the tube should be addressed.

The coupling of the quasi-1D, inviscid flow model and the 3D structural model has been accomplished. The flow and the deformation of the tube are calculated employing an iteration procedure between flow and structure. The solution of the fluid-structure interaction depends on three dimensionless parameters: the tube aspect ratio L/D, the dimensionless transmural pressure $C_{p,ext} = (p_{ext} - p_0)/(1/2\rho_0 w_0^2)$ and the dimensionless elasticity parameter $k_p = E(h/R)^3/[12(1-\nu^2)1/2\rho_0 w_0^2]$. Since $C_{p,ext}$ is fixed to a value of 1 the solution for a tube with a specific L/D is a function of k_p only, which greatly reduces the number of parameters to be investigated.
In this research the value of k_p at which tubes collapse has been determined, as a function of L/D in the range [1,10]. For low values of L/D the "critical" value of k_p, i.e. $k_{p,crit}$, increases approximately linearly, for values of L/D above 6 the "critical" value is constant (0.451), equal to the one for an infinite tube.
In the present research the ends of the tubes are treated as clamped. An improvement is to develop spring-type of end conditions, which will require a structural model of the whole lung system. Furthermore, the tube wall has been considered as a homogeneous material, while in reality it appears to consist out of a number of layers. Apart from the extension of the present method to discretizations with more than one element across the wall thickness, a physiologically more correct multi-layer model of the wall may be considered.

The final part of the research focuses on numerical simulation of forced expiration for the Hansen and Ampaya lung model ([16]). Employing $k_{p,crit}$ as function of L/D an estimate is obtained for a possibly lower limit for the Young modulus E, i.e. the value of E the tube wall should have in order to collapse just at the end of the forced expiration. This characteristic value of the elasticity of the airway wall has been determined for a healthy lung for generation 2 to generation 12. The found values of the generation dependent lower limit of the material of the lung tube wall should be validated using physiological data.

Our ultimate goal is a fluid-structure model for the complete human lung system that could be used in practice, for support of diagnosis, for example. In this research much insight has been obtained in flow-induced collapse of human airways. However, much more research on the fluid dynamics and structural mechanics of the lung is needed to achieve our ultimate goal.

INERTIAL MOMENTS

APPENDIX A

A.1 Moments of inertia of planar area

The moments of inertia have been used for the calculation of the deformation and the normal stress of bodies under external loads (see section 3.4.3). They permit one-dimensional formulation of three-dimensional deformations, by describing the behavior of the surface.
In this section the properties of a plane surface (area, first moment, centroid and moment of inertia) will be presented. Then, the moment of inertia for a rectangle, a circular ring and a quarter of a circular ring will be calculated.
For more details see [15].

A.1.1 Centroids of areas

The location of the centroid of a planar area is an important property of the area. To determine the coordinates of the centroid, let us refer to the area A in figure A.1.
The total area A is defined as:

$$A = \int dA \tag{A.1}$$

The first moments of the area about the x and y axis, respectively, are defined as:

$$Q_x = \int y dA \quad ; \quad Q_y = \int x dA \tag{A.2}$$

in which x and y are the coordinates of the differential element of area dA.
The coordinates $\bar{x}$ and $\bar{y}$ of the centroid C are defined as:

$$\bar{x} = \frac{Q_y}{A} = \frac{\int x\, dA}{\int dA} \quad ; \quad \bar{y} = \frac{Q_x}{A} = \frac{\int y dA}{\int dA} \tag{A.3}$$

If an area is symmetric about an axis, the centroid must be located on this axis, because the first moment about an axis of symmetry equals zero. Furthermore, if the area has two axes of symmetry, the centroid is located at the intersection of these axes.

A.1.2 Moments of inertia of areas

The moment of inertia of a planar area (see figure A.1) with respect to the x and y axes, respectively, are defined as:

$$\begin{array}{l} I_x = \int (y - \overline{y})^2 dA \\ I_y = \int (x - \overline{x})^2 dA \end{array} \tag{A.4}$$

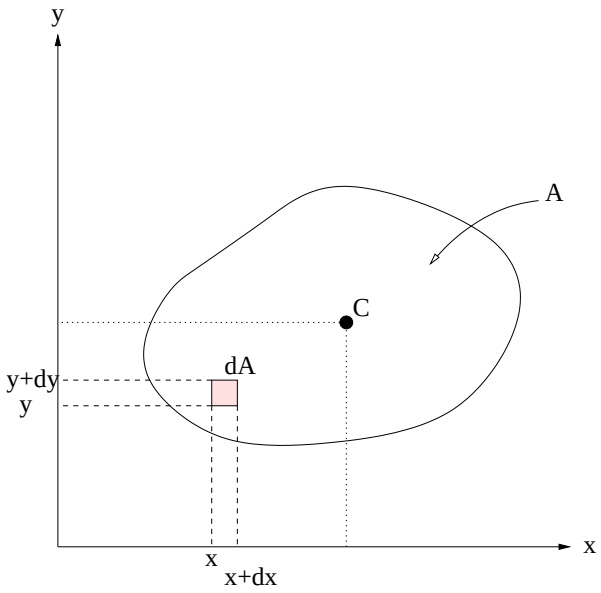

FIGURE A.1: *Planar area A and differential element of area $dA = dxdy$. The origin of the axes are located at the centroid C.*

in which x and y are the coordinates of the differential element of area dA and $\overline{y}$ and $\overline{x}$ are the coordinates of the centroid C.

A.1.3 Moments of inertia of a rectangle

From equations A.1, A.2, A.3 and A.4, the area, first moment, coordinates of the centroid and the moments of inertia for a rectangle, such as pictured on figure A.2, are calculated as:
Area:

$$A = hb \tag{A.5}$$

First moment of area:

$$Q_x = \frac{bh^2}{2} \quad ; \quad Q_y = \frac{hb^2}{2} \tag{A.6}$$

Centroid:

$$\bar{x} = \frac{b}{2} \quad ; \quad \bar{y} = \frac{h}{2} \tag{A.7}$$

Note that the rectangle has two axes of symmetry: $x = \frac{b}{2}$ and $y = \frac{h}{2}$. The centroid is located at the intersection of these two axes.

Moment of inertia:

$$I_x = \frac{bh^3}{12} \quad ; \quad I_y = \frac{hb^3}{12} \tag{A.8}$$

A.1.4 Moments of inertia of a circular ring

A circular ring (see figure A.3) is defined by the surface between two circles of radius a and radius b. The average radius $\overline{r}$ ($\overline{r} = (a + b)/2$) and the thickness t ($t = (b - a)$) can also be

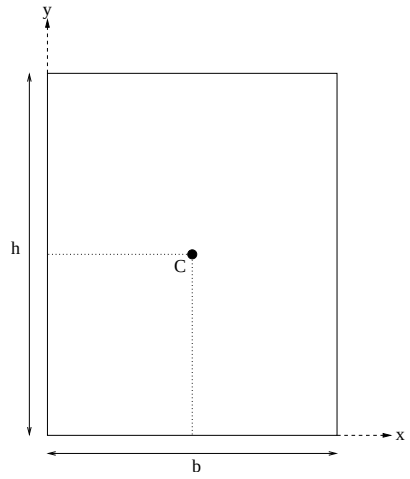

FIGURE A.2: *Rectangle of sides b and h ; the origin of the axes is taken at the centroid C.*

used to define the geometry of the circular ring.
The centroid will be at the intersection of the two axes x and y, i.e. at the center of the ring. Furthermore, due to the symmetry, the two moments of symmetry I_x and I_y are equal. From equation A.4, they are calculated as, for $t \ll \overline{r}$:

$$I_x = I_y = \pi \overline{r}^3 t \tag{A.9}$$

A.1.5 Moments of inertia of a quarter of a circular ring

In this section, the area and moments of inertia of a quarter of a circular ring are investigated (see figure A.4).
The region is defined as the area between two circles of radius a and b, respectively, in the positive quadrant ($x > 0, y > 0$). For the evaluation of the integrals, a differential element of area dA is defined as (see figure A.4):

$$dA = r dr d\theta \quad ; \quad r \epsilon [a, b] \quad ; \quad \theta \epsilon [0, \pi/2] \tag{A.10}$$

Area
The area A is calculated as the area of the outer disk A_b minus the area of the inner disk A_a:

$$A = \int_a^b \int_0^{\pi/2} r dr d\theta \tag{A.11}$$

We find:

$$A = \frac{\pi}{4}(b^2 - a^2) \tag{A.12}$$

Centroid

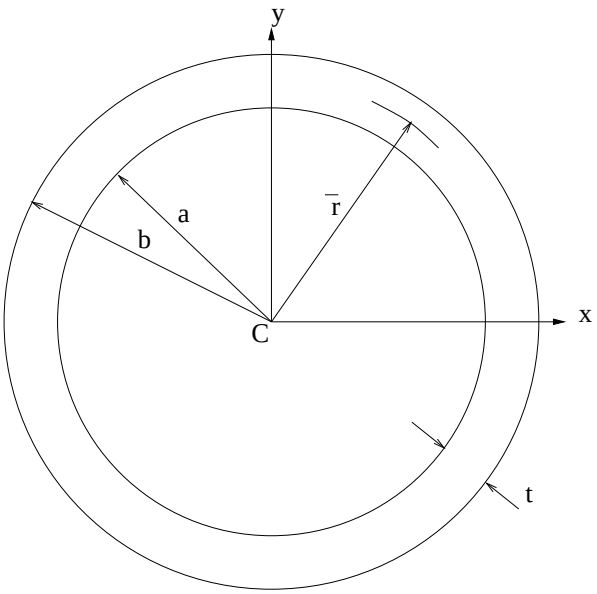

FIGURE A.3: *Circular ring of average radius $\overline{r}$ and thickness t.*

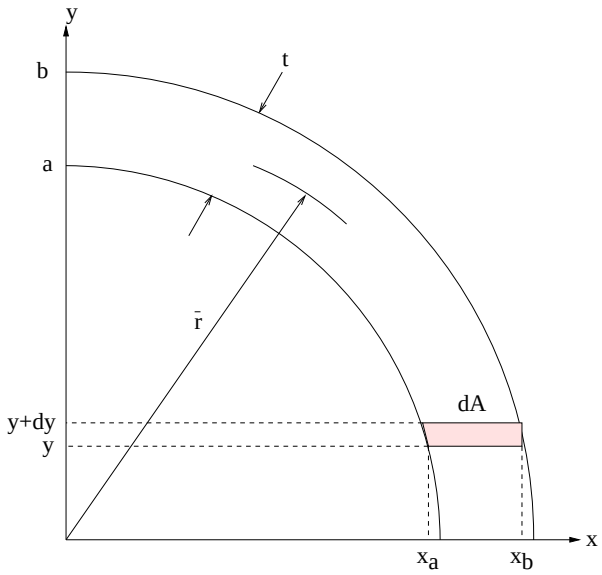

FIGURE A.4: *Quarter of a circular ring of average radius $\overline{r}$ and thickness t.*

The quarter of a circular ring has one axis of symmetry, the line $\theta = \pi/4$. The centroid C is located on this line. The coordinates of the centroid $(\bar{x}, \bar{y})$ are calculated as (see equa-

tion A.3):

$$\bar{x} = \frac{Q_y}{A} = \frac{\int x dA}{\int dA} \quad ; \quad \bar{y} = \frac{Q_x}{A} = \frac{\int y dA}{\int dA} \tag{A.13}$$

In polar coordinates, we find:

$$Q_x = \int y dA = \int_a^b \int_0^{\pi/2} r sin\theta r dr d\theta = \frac{1}{3}(b^3 - a^3) \tag{A.14}$$

By symmetry, $\bar{x} = \bar{y}$. The coordinates of the centroid are:

$$\bar{x} = \bar{y} = \frac{4}{3\pi}\frac{b^3 - a^3}{b^2 - a^2} \tag{A.15}$$

Moment of inertia

From equation A.4 the moment of inertia I_x and I_y are written as:

$$\begin{array}{c} I_x = \int (y - \overline{y})^2 dA \\ I_y = \int (x - \overline{x})^2 dA \end{array} \tag{A.16}$$

which yields:

$$\begin{array}{c} I_x = \frac{\pi}{16}(b^4 - a^4) - \overline{y}^2 \frac{\pi}{4}(b^2 - a^2) \\ I_y = \frac{\pi}{16}(b^4 - a^4) - \overline{x}^2 \frac{\pi}{4}(b^2 - a^2) \end{array} \tag{A.17}$$

The area can still be calculated as:

$$A = \frac{\pi}{4}(b^2 - a^2) \tag{A.18}$$

By choosing the centroid as the origin, one can compute the moment of inertia with respect to the axis BB, defined as $y = \bar{y}$ (by symmetry, the axis BB could also be defined as $x = \bar{x}$) (see figure A.5)

The moment of inertia is defined as (see equation A.4):

$$I_{BB} = \int y^2 dA = I_{xx} \tag{A.19}$$

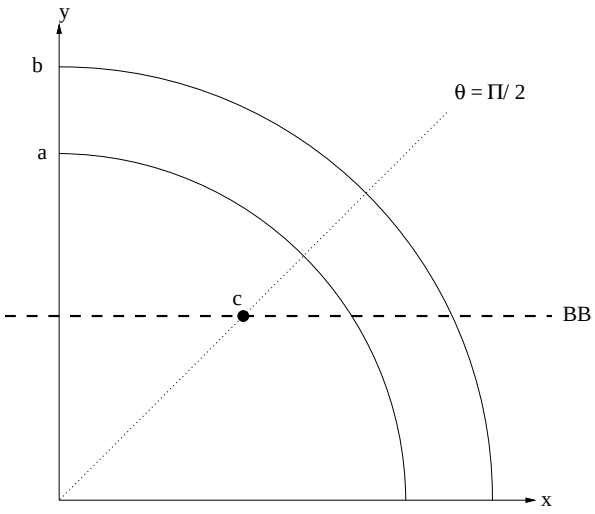

FIGURE A.5: *Quarter of a circular ring: centroid C and axis BB.*

REFERENCES

[1] S. Adam. *Numerische und experimentelle Untersuchung instationarer Dusenstrommingen mit Energiezufuhr durch homogene Koudenstation.* PhD thesis, Universitat Karlsruhe, Karlsruhe, Germany, 1996.

[2] J. D. Jr Anderson. *Computational fluid dynamics, the basics with applications.* McGraw-Hill, Inc., 1995.

[3] C. D. Bertram, C. J. Raymond, and T. J. Pedley. Mapping of instabilities during flow through collapsed tubes of differing length. *J. Fluids Struct.*, 4:125–154, 1990.

[4] C. Cancelli and T. J. Pedley. A separated flow model for collapsible tube oscillations. *J. Fluid Mech.*, 157:375–404, 1985.

[5] T. R. Chandrupatla and A. D. Belegundu. *Introduction to finite elements in engineering.* Prentice-Hall International Editions, 1991.

[6] W. A. Conrad. Pressure-flow relationship in collapsible tubes. *IEEE Trans. Bio-Med. Engng.*, BME-16:284–295, 1969.

[7] S. J. Cowley. Elastic jumps on fluid-filled elastic tubes. *J. Fluid Mech.*, 116:459–473, 1982.

[8] S. J. Cowley. On the wavetrains associated with elastic jumps on fluid-filled elastic tubes. *Q. J. Mech. Appl. Math.*, 36:289–312, 1983.

[9] S. V. Dawson and E. A. Elliot. Wave-speed limitation on expiratory flow - a unifying concept. *J. Appl. Physiol.*, 43:498–515, 1977.

[10] M. J. Fagan. *Finite element analysis, theory and practice.* Longman group UK limited, 1992.

[11] J. H. Ferziger and M. Perić. *Computational methods for fluid dynamics.* Springer, Verlag Berlin Heidelberg, 1996.

[12] J. E. Flaherty, J. B. Keller, and S. I. Rubinow. Post buckling behavior of elastic tubes and rings with opposite sides in contact. *SIAM J. Appl. Math.*, 23:446–455, 1972.

[13] A. T. Fox, R. W. & McDonald. *Introduction to fluid mechanics, Fith Edition.* John Wiley & Sons, Inc., 1998.

[14] Y. C.. Fung. *Biomechanics: Circulation, Second Edition.* Springer, Verlag New York Inc., 1996.

[15] J. M. Gere and S. P. Timoshenko. *Mechanics of material, Third SI Edition.* Chapman & Hall, 1992.

[16] J. E. Hansen and E. P. Ampaya. Human air space shapes, sizes, areas, volumes. *J. Appl. Physiol.*, 38(6):990–995, 1975.

[17] A. L. Hazel and M. Heil. Steady finite-reynolds-number flows in collapsible tubes. *J. Fluid Mech.*, 486:79–103, 2003.

[18] M. Heil. *Large deformations of cylindrical shells conveying viscous flow.* PhD thesis, University of Leeds, Leeds, U. K., 1995.

[19] M. Heil. Stokes flow in collapsible tubes: computation and experiment. *J. Fluid Mech.*, 353:285–312, 1997.

[20] M. Heil. Stokes flow in elastic tube - a large-displacement fluid-structure interaction problem. *Int. J. Numer. Meth. Fluids*, 28:243–265, 1998.

[21] M. Heil and T. J. Pedley. Large post-buckling deformations of cylindrical shells conveying viscous flow. *J. Fluids Struct.*, 10:565–599, 1996.

[22] O. E. Jensen. Instabilities of flow in a collapsed tube. *J. Fluid Mech.*, 220:623–659, 1990.

[23] O. E. Jensen. Chaotic oscillations in a simple collapsible-tube model. *ASME J. Biomech. Engng.*, 144:55–59, 1992.

[24] O. E. Jensen. An asymptotic model of viscous flow limitation in a highly collapsed channel. *ASME J. Biomech. Engng.*, 120:544–547, 1998.

[25] O. E. Jensen and T. J. Pedley. The existence of steady flow in a collapsed tube. *J. Fluid Mech.*, 206:339–374, 1989.

[26] A. I. Katz, Y. Chen, and A. H. Moreno. Flow through a collapsible tube - experimental analysis and mathematical model. *Biophys. J.*, 9:1261–1279, 1969.

[27] I. Kececioglu, M. E. McClurken, R. D. Kamm, and A. H. Shapiro. Steady, supercritical flow in collapsible tubes. part 1. experimental observations. *J. Fluid Mech.*, 109:367–389, 1981.

[28] H. Langhaar. Steady flow in the transition length of a straight tube. *J. Appl. Mech.*, 9:A55–A58, 1942.

[29] S. J. Liang, G. P. Neitzel, and C. K. Aidun. Finite element computations for unsteady fluid and elastic membrane interaction problems. *Int. J. Num. Meth. Fluids.*, 24:1091–1110, 1997.

[30] J. Lighthill. *Mathematical biofluiddynamics.* Philadelphia: SIAM, 1975.

[31] M-S. Liou and C. J. Jr. Steffen. A new flux splitting scheme. *Journal of Computational Physics,* 107:23–39, 1993.

[32] T. W. Lowe and T. J. Pedley. Computation of stokes flow in a channel with a collapsible segment. *J. Fluids and Stuctures*, 9:885–905, 1995.

[33] X. Y. Luo and T. J. Pedley. A numerical simulation of steady flow in a 2-d collapsible channel. *J. Fluids and Stuctures*, 9:149–174, 1995.

[34] X. Y. Luo and T. J. Pedley. A numerical simulation of unsteady flow in a two-dimensional collapsible channel. *J. Fluid Mech.*, 314:191–225, 1996.

[35] X. Y. Luo and T. J. Pedley. The effect of wall inertia on flow in a two-dimensional collapsible channel. *J. Fluid Mech.*, 363:253–280, 1998.

[36] X. Y. Luo and T. J. Pedley. Multiple solutions and flow limitation in collapsible channel flows. *J. Fluid Mech.*, 420:301–324, 2000.

[37] Y. Matsuzaki and K. Fujimura. Reexamination of steady solutioins of a collapsible channel conveying fluid. *ASME J. Biomech. Engng.*, 117:492–494, 1995.

[38] M. E. McClurken, I. Kececioglu, R. D. Kamm, and A. H. Shapiro. Steady, supercritical flow in collapsible tubes. part 2. theoretical studies. *J. Fluid Mech.*, 109:391–415, 1981.

[39] G. C. Oates. Fluid flow in soft-walled tubes: I. steady flow. *Med. Biol. Engng.*, 13:773–778, 1975.

[40] Shih-I Pai and Shijun Luo. *Theoretical and computational dynamics of a compressible flow.* Science press, Beijing., 1991.

[41] T. J. Pedley. Longitidinal tension variation in collapsible channels: a new mechanism for the breakdown of steady flow. *ASME J. Biomech. Engng.*, 114:60–67, 1992.

[42] G. Pedrizetti. Fluid flow in a tube with an elastic membrane insertion. *J. Fluids Mech.*, 375:39–64, 1998.

[43] F. Put. *Numerical simulation of condensation in transonic flows.* PhD thesis, University Of Twente, Enschede, The Netherlands, 2003.

[44] M. P. Rast. Simultaneous solution of the navier-stokes and elastic membrane equations by a finite-element method. *Int. J. Num. Meth. Fluids*, 19:1115–1135, 1994.

[45] P. E. Rauwerda. *Unequal ventilation of different parts of the lung and determination of cardiac output.* PhD thesis, Groningen State University, The Netherlands, 1946.

[46] F. Rohrer. Der stromungswiderstand in den menschlichen aremwegem. *Pflugers Arch. ges. Physiol.*, 162:225–259, 1915.

[47] L. Schiller. Untersuchungen uber laminare und turbulente stromung. *ZAMM*, 2:96–106, 1922.

[48] H. Schlichting. *Boundary-layer theory, Sixth Edition.* McGraw-Hill, Inc., 1998.

[49] A. H. Shapiro. Steady flow in collapsible tubes. *ASME J. Biomech. Engng.*, 99:126–147, 1977.

[50] M. Thiriet and C. Ribreau. Computational flow in a collapsed tube with wall contact. *Mec. Ind.*, 1:349–364, 2000.

[51] M. Tobak and D. J. Peake. Topology of three-diamensional separated flows. *Ann. Rev. Fluid Mech.*, 14:61–85, 1982.

[52] B. Van Leer. Toward the ultimate conservative difference scheme. *Journal of Computational Physics*, 32:101–136, 1979.

[53] E. R. Weibel. *Morphometry of the human lung.* Academic Press, New York, 1963.

[54] G. A. Wempner. *Mechanics of solids.* McGraw-Hill, 1973.

[55] B. A. Wolles. *Computational viscid-inviscid interaction modelling of the flow about aerofoils.* PhD thesis, University Of Twente, Enschede, The Netherlands, 1998.

[56] O. C. Zienkiewicz and R. L. Taylor. *The finite element method, Fourth Edition.* McGraw-Hill, Inc., 1989.

SUMMARY

During a normal lung-function test to determine the health state of a human lung, lung airway collapse will occur and limit the outflow at the mouth of a person. The aim of the study is to obtain qualitative and quantitative insight in the flow in, and the deformation of, the elastic tubes that constitute the lungs.

The lung-function test is a clinical test to determine the health state of a human lung. The patient is asked to expire as hard as possible in a spirometer. The result is presented as the flow-volume curve, in which the expired flow at the mouth is plotted versus the expired volume of air. The characteristics of the flow-volume curve depend on the health state of the lungs, which is thought to affect the compliance (flexibility) of the walls of the lung tubes. The compliance is the decisive parameter in the collapse of lung airways.

The process of the collapse of an airway is induced by a decrease of the pressure inside the airway due to the air flow: as the cross-sectional area of the airway decreases, the velocity of the flow increases, yielding a decrease of the pressure. Since the pressure outside the airway remains constant, the transmural pressure (the internal pressure minus the external pressure) becomes negative. This acts like an inward, normal force applied on the wall of the airway. The airway is compressed. The cross-sectional areas decreases and thus the inside pressure decreases, yielding a larger (negative) transmural pressure and a larger deformation of the tube. Dependent of the mechanical properties of the wall of the airway this process leads to a further deformation of the airway and ultimately to a partial or a complete collapse of the airway. The whole process depends on the inlet flow rate and on the mechanical properties of the lung tube.

The ultimate aim is to develop a numerical simulation method employing realistic mathematical models of the geometrical and mechanical structure of the lungs as well as of the flow of air. This thesis contributes to this aim. The human lung can be modeled as a ”tree” structure: each airway, or ”tube”, splits into two tubes, which in their turn split into two tubes each, iteratively. Each step is called a generation. In the present study we use the geometric lung model of Hansen and Ampaya ([16]), which they derived from Weibel’s model ([53]). It provides the diameter and length of each of the 27 generations of the model, where generation 0 is the trachea and generation 26 the last generation Alveoli are present in generation 16 to 26. The model does not provide the compliance of the lung tube walls.

In this study we consider single tubes and the flow through a tube is coupled to the deformation of the tube wall. We consider models for inviscid flows, one for an incompressible flow, one for isentropic compressible flow and the model based on the Euler equations for non-isentropic flow. It is shown that for the flow in the lungs, even during forced expiration the incompressible flow model suffices. Furthermore, the flow is assumed to behave like a quasi-one dimensional flow. The continuity equation in combination with the Bernoulli relation for incompressible flow is used to compute the flow.

The flow model is coupled to a structural model. A 3D Finite Element Method (FEM)-based computational method has been developed to compute the deformation of the tube wall due to a distributed normal load consisting of the transmural pressure. A 3D, structured, mesh is used to discretize the tube wall. The mesh consists of 20-node, hexahedral elements (the nodes are located at the eight corners of the cell and at 12 mid-side points). The elasticity of the tubes, represented by the mechanical properties of the tube wall, is defined by the Young modulus E [Pa] and by the Poisson ratio ν [-]. The elasticity (compliance) differs for each generation, being stiff at the trachea (generation 0) and soft at the last generations of the lung model. Quantitative data on the compliance of lung tubes is scarce.
The structural model includes a non-linear relation between the strain and the deformation. The results of the structural method have been validated successfully by comparison with the results from beam theory and from the commercial software ANSYS. For tubes results of the present finite-element method are compared with results from ANSYS showing a good agreement. Comparison of both these results and results from the empirical tube law for the deformation of infinitely long tubes subjected to a constant pressure difference show a poor agreement indicating the inadequacy of the tube law.

The method developed has been applied to the flow in the tubes of Hansen and Ampaya's lung model ([16]). The influence of the elasticity modulus E and Poisson ratio ν on the partial collapse have been determined, as well as the influence of the mesh.
From these results we determined the dimensionless similarity parameter $k_p = E(h/R)^3/[12(1-\nu^2)1/2\rho_0 w_0^2]$, as function of L/D, for which the tube collapses, with h the initial thickness, R=D/2 the initial radius of the tube, ρ_0 the density of air, w_0 the inflow velocity and L the length of the tube. With this result we determined for generation 2 to 12 of Hansen and Ampaya's lung model ([16]) the value of the elasticity modulus E (for $\nu = 0.3$ and wall thickness $h/R = 0.1$) for which the tube is on the verge of full collapse. This value of E can be thought of as an estimate of the lower limit of E of the lung tubes in generation 2 to 12.

SAMENVATTING

Bij een longfunctie onderzoek wordt de conditie van de longen onderzocht via onder meer een geforceerde uitademing. Hierbij kunnen de luchtwegen collaberen waardoor de uitstroom aan de mond wordt gelimiteerd. Het doel van de huidige studie is om zowel een kwalitatief als kwantitatief beeld te krijgen van de stroming in, en de vervorming van, de elastisch longbuizen waaruit de menselijke long bestaat.

Een longfunctiemeting is een diagnostische test om de gezondheidstoestand van longen te kunnen meten. De patiënt wordt gevraagd om zo hard mogelijk uit te ademen in een spirometer. Het resultaat wordt weergegeven in een grafiek als een uitstroomsnelheid-volume kromme, waarin de uitstroomsnelheid aan de mond (liter/s) wordt uitgezet als functie van het uitgeademde volume (liter). De kenmerken van de vorm van de uitstroomsnelheid-volume kromme hangen af van de conditie van de longen. Er zijn aanwijzingen dat de conditie van de longen de compliantie (elasticiteit) van de wand van de luchtwegen beïnvloedt. De compliantie van een luchtweg is de bepalende factor voor het optreden van het inklappen van de luchtweg.

Het collaberen van een luchtweg wordt geïnduceerd door een verlaging van de druk in de luchtweg veroorzaakt door de stroming door de luchtweg. Wanneer voor een gegeven debiet het oppervlak van de dwarsdoorsnede van de luchtweg kleiner wordt, zal in de luchtweg de snelheid van de stroming toenemen en de druk dalen. Omdat de druk rondom de luchtweg constant blijft, wordt de transmurale druk (de druk in luchtweg min de druk erbuiten) negatief. Dit werkt als een naar binnen gerichte normaalkracht op de luchtwegwand waardoor de luchtweg wordt ingedrukt. Het oppervlak van de dwarsdoorsnede neemt daardoor af, waardoor de snelheid verder toeneemt en de interne druk verder afneemt zodat een grotere, negatieve, transmurale druk ontstaat. Afhankelijk van de mechanische eigenschappen van de luchtwegwand leidt dit tot een verdere vervorming van de luchtweg. Uiteindelijk wordt een evenwichtsituatie bereikt, al dan niet in de vorm van gedeeltelijke of gehele luchtwegcollaps. Dit proces van collaps hangt af van het debiet door, en van de mechanische eigenschappen van, de luchtweg.

Het uiteindelijke doel van het onderzoek is het ontwikkelen van een numerieke simulatie methode waarin realistische mathematische modellen van het geometrische en mechanische gedrag van de longen zijn vervat als ook van de stroming in de longen. Dit proefschrift is een aanzet daartoe.

De menselijke long kan worden gemodelleerd als een boom, iedere luchtweg of ”buis” splitst in twee buizen die op hun beurt weer in tweeën splitsen, enzovoorts. Iedere stap wordt een generatie genoemd. In deze studie wordt het geometrisch model van Hansen en Ampaya ([16]) gebruikt, dat is afgeleid van het longmodel van Weibel ([53]). Het model geeft de diameter en de lengte van de buizen van ieder van de 27 generaties, waarbij generatie 0 de trachea is en generatie 26 de laatste generatie is. Vanaf generatie 16 zijn er longblaasjes aanwezig. Het model geeft geen informatie over de compliantie van de luchtweg.

In deze studie wordt de stroming door de buis gekoppeld aan de vervorming van de buiswand in één enkelvoudige buis. Er is gebruik gemaakt van modellen voor niet-viskeuze stromingen, namelijk een voor onsamendrukbare stromingen, een voor isentrope samendrukbare stromingen en het model gebaseerd op de Euler vergelijkingen voor niet-isentrope samendrukbare stromingen.
Aangetoond wordt dat voor de stroming in een menselijke long een model voor een onsamendrukbare stroming afdoende is. Verder wordt aangenomen dat de stroming mag worden beschouwd als quasi-ééndimensionaal. De continuïteitsvergelijking leidt dan tot een eenvoudig verband tussen dwarsdoorsnede-gemiddelde snelheid en het oppervlak van de dwarsdoorsnede terwijl de druk volgt uit de wet van Bernoulli voor onsamendrukbare stromingen.

Het stromingsmodel wordt gekoppeld aan een mechanisch model. Een 3D eindige-elementen methode (FEM) is ontwikkeld waarmee de vervorming van de buiswand ten gevolge van een verdeelde normaalkracht, de transmurale druk, wordt berekend. Een 3D, gestructureerd rekennetwerk is gebruikt om de buiswand te discretiseren. Het rekennetwerk bestaat uit 20-punts hexahedrale elementen (de knooppunten zijn de 8 hoekpunten en de 12 middelpunten van iedere zijde van het element). De elasticiteit van de buizen wordt bepaald door de mechanische eigenschappen van de buiswand: de Young modulus E [Pa] en de Poisson ratio ν [-]. Iedere generatie heeft zijn eigen elasticiteit (compliantie). De trachea (generatie 0) is stijf terwijl de laatste generaties van het longmodel meer flexibel zijn. Kwantitatieve data over de compliantie van longbuizen is schaars.
Het mechanisch model bevat een niet-lineaire relatie tussen de spanning en de deformatie. De resultaten van het mechanische model zijn gevalideerd door ze te vergelijken met de analytische resultaten van de ”balk-theorie” en met de resultaten van het commerciële software pakket ANSYS. Voor buizen zijn resultaten van de eindige-elementen methode vergeleken met resultaten van ANSYS en resultaten van de empirische tube-law, allen voor de vervorming van oneindig lange buizen waarop een constant drukverschil werkt. De overeenkomst van resultaten van de huidige methode en die van ANSYS zijn goed. Er zijn aanzienlijke verschillen tussen de resultaten van de tube law aan de ene kant en die van ANSYS en de huidige methode aan de andere kant, hetgeen suggereert dat de tube law tekort schiet.

De ontwikkelde methode is toegepast op de stroming bij geforceerde uitademing in buizen zoals die voorkomen in het Hansen-Ampaya longmodel ([16]). De invloed van de elasticiteitsmodulus E, de Poisson ratio ν en het aantal elementen van het rekennetwerk op het (gedeeltelijk) collaberen van een buis is onderzocht. Uit deze resultaten volgt de waarde van de dimensieloze gelijkvormigheidsparameter $k_p = E(h/R)^3/[12(1-\nu^2)]/(1/2\rho_0 w_0^2)$ waarvoor de buis inklapt als functie van L/D. Hierin is h de initiële dikte van de buiswand, $R = D/2$ de initiële straal van de buis, ρ_0 de dichtheid van lucht, w_0 de snelheid van de

stroming door de onvervormde buis en L de lengte van de buis.

Met dit resultaat is voor het geval van geforceerde uitstroming voor generatie 2 tot 12 van het Hansen Ampaya model ([16]) de waarde van de elasticiteismodulus E (voor $\nu = 0.3$ en een wanddikte $h/R = 0.1$) bepaald waarbij de luchtweg op het punt staat volledig te collaberen. Deze waarde van E kan worden opgevat als een schatting van de ondergrens van de elasticiteitsmodulus van longbuizen in generatie 2 tot en met 12.

ACKNOWLEDGMENT

During the period of working on the topic that is the subject of this thesis a number of persons have been important.

I would like to express my gratitude to my promotor, Prof. Dr. Ir. H.W.M. Hoeijmakers, who gave me the opportunity to conduct this research. His experience in the field of fluid dynamics happened to be a precious help in the guidance of this thesis.

I also would like to thank my assistant promotor Dr. Ir. F.H.C de Jongh, who introduced me into the field of the flow in lungs and guided me through this wide multi-disciplinary field of great societal relevance.

Dr. Ir. H.J.M. Geijselaers played a major role in the success of this thesis with his competences and expertise in solid mechanics, specifically the finite-element method and ANSYS. Furthermore, he has always been very willing to help me. I am greatly thankful for the time and effort he put into my work.

A special thanks goes to the secretaries (Susan, Jennifer, Yvonne and Anjenet) that, even though often discrete, offer an important support.

Finally I would like to thank all the staff, (former) PhD students and students I had the pleasure to meet during these past few years.

ABOUT THE AUTHOR

Olivier Massiot was born on October 10, 1975 at Rennes, France.

From 1993 to 1998 he conducted studies at the University of Rennes I, where he got exposed to a wide range of topics in physics. The course concerning astronomy was especially appreciated.
He completed his masters in energy physics in Grenoble, France, at the INPG (Institut National Polytechnique de Grenoble), de l'Institut National des Sciences et Techniques Nucléaires, de l'université Grenoble 1.

In 1999 he continued his scientific education in the group Engineering Fluid Dynamics of the Department of Engineering Technology of the University of Twente, the Netherlands. There he worked under the guidance of dr.ir. F.H.C. de Jongh and prof.dr.ir. H.W.M. Hoeijmakers within the research theme Biophysical Fluid Dynamics, specifically the flow in lungs.